An investigation of the Matteucci effect on amorphous wires and its application to bend sensing

Sahar Alimohammadi

A thesis submitted to Cardiff University in candidature for the degree of Doctor of Philosophy

Wolfson Centre for Magnetics
Cardiff School of Engineering, Cardiff University
Wales, United Kingdom

Dec 2019

Acknowledgment

I would like to express my deepest thanks to my supervisors Dr Turgut Meydan and Dr Paul Ieuan Williams who placed their trust and confidence to offer me this post to pursue my dreams in my professional career which changed my life forever in a very positive way. I sincerely appreciate them for their invaluable thoughts, continuous support, motivation, guidance and encouragements during my PhD. I am forever thankful to them as without their guidance and support this PhD would not be achievable.

I would like to thank the members of the Wolfson Centre for Magnetics, in particular, Dr Tomasz Kutrowski and Dr Christopher Harrison for their kind assistance, friendship and encouragement during my PhD. They deserve a special appreciation for their warm friendship and support. Also, I am thankful to my colleague and friend Robert Gibbs whose advice was hugely beneficial in helping me to solve many research problems during my studies.

This research was fully funded by Cardiff School of Engineering Scholarship. I gratefully acknowledge the generous funding which made my PhD work possible.

I owe a debt of gratitude to all my colleagues and friends, Vishu, Hamed, Lefan, Sinem, Hafeez, Kyriaki, Frank, Gregory, Seda, Sam, Paul, Alexander, James, Jerome and Lee for their kind friendship. Also, I would like to thank other staff members of the Wolfson Centre for their friendships and support during my research especially, Dr Yevgen Melikhov.

I would like to very especially thank my Mum and Dad whose love and support has been always so inspiring to me. I would say a heartfelt thank you to them for believing in me and encouraging me to follow my dreams. I owe them a great debt of gratitude as without their constant love, encouragement and strong support none of my achievements in my life would be possible.

Last but not least, many thanks goes to my husband Hamid who deserves considerable recognition for his continuing love, support, criticism and advice. Without his bright thoughts and advice this PhD was not achievable. Also I am thankful to my brother Yashar for his emotional support and encouragement.

Abstract

The study of wearable sensors for human biometrics has recently developed into an important research area due to its potential for personalised health monitoring. To measure bending parameters in humans such as joint movement or posture, several techniques have been proposed however, the majority of these suffer from poor accuracy, sensitivity and linearity. To overcome these limitations, this research aims to develop a novel flexible sensor for the measurement of bending by utilising the Matteucci effect on amorphous wires. The Matteucci effect occurs in all ferromagnetic wires but the advantages of amorphous wires are their superior soft magnetic and magnetoelastic properties and a Matteucci effect that is very sensitive to applied stresses like tensile and torsion. For these reasons a sensor based on Matteucci effect was investigated for use as a wearable bending sensor.

Previous studies of the Matteucci effect have been interpreted in terms of simple phenomenological models using conveniently sized lengths of amorphous wire. In this work, the Matteucci effect has been characterised in short, sensor-compatible, wires. In addition, a thorough examination of the stress dependency of the Matteucci effect was also investigated as this is an area that has been neglected in the past.

The main aim of this work was to study the effect of tensile and torsion stresses on the Matteucci effect in both highly positive magnetostrictive and nearly zero magnetostrictive amorphous wires. A measurement rig was specifically built to characterise the Matteucci effect for a range of magnetic field amplitudes, frequencies, torsions and axial stresses. The second major aim was to use this characterisation data to ascertain the optimum working parameters to design and construct a novel flexible bending sensor.

In this work, the Matteucci effect in amorphous wires was found to be very sensitive to both axial and torsional applied stresses and dependent upon the sign of the magnetostriction. Insights gained here were used to develop the bend sensor in three steps. The initial prototype was a non-flexible strain sensor for measuring tensile stress and exhibited a very high gauge factor equal to 601 ± 30. The second step resulted in a strain sensor prototype utilising a flexible planar coil to magnetise the amorphous wire. The final step produced a bend sensor this time consisting of a flexible solenoid with greater magnetising capability. It resulted in a bend sensor

with a high output voltage sensitivity of 5.62 ± 0.02 mV/cm which is the slope of the voltage due to curvature and excellent linearity (R^2 = 0.98). In this case the sensor's operating range was 1.11 rad to 2.49 rad with $\pm$ 0.003 rad uncertainty. This range is scalable and dependent on the sensor configuration. This work has demonstrated the feasibility of utilising the Matteucci effect as a bend sensor with a performance exceeding that found in many commercial sensors.

Publications

Journal article:

- S.Alimohammadi, T. Meydan, P.Williams, “Strain Sensing by Exploiting the Matteucci Effect in Amorphous Wire”, International Journal of Applied Electromagnetics and Mechanics (IOS), vol. 59, no. 1, pp. 115-121, 2019 DOI: 10.3233/JAE-171225

Conferences:

- S.Alimohammadi, T. Meydan, P.Williams, “A Flex Sensor Utilizing the Matteucci Effect in Magnetostrictive Amorphous Wire on the “12th European magnetic sensors and actuators conference, Athens- Greece 01/06/2018.
- S.Alimohammadi, T. Meydan, P.Williams, “Exploiting the Matteucci Effect in Amorphous Wire for sensor applications on the “23rd soft magnetic materials (SMM) conference, Sevilla- Spain 10/09/2017.

Nomenclature

Acronyms

AC	Alternating current
B	Boron
C	Carbon
Cr	Chromium
CMOS	Complementary metal- oxide Semi-conductor
CNT	Carbon nanotubes
Co	Cobalt
DC	Direct current
EGF	Equivalent Gauge factor
Fe	Iron
FEM	Finite element method
FTP	Fingertip blood tip vessel pulsation
GF	Gauge factor
GMI	Giant magnetoimpedance effect
Inc.	Incorporation
IWE	Inverse Wiedemann Effect
LBD	Large Barkhausen Discontinuous
ME	Matteucci effect
MI	Magneto-Impedance
MOIF	Magneto- optical indicator film
MOKE	Magneto- optical Kerr effect
Mn	Manganese
Ni	Nickel
PCB	Printed circuit board
P	Phosphorus
SA1	First flexible bending sensor with annealed amorphous wire
SA2	Second flexible bending sensor with annealed amorphous wire
SD	Standard deviation
SI	Stress impedance

Si	Silicon
S1	Flexible bending sensor number one
S2	Flexible bending sensor number two
S3	Flexible bending sensor number three
S4	Flexible bending sensor number four
TSA	Flexible bending sensor with twisted annealed amorphous wire
2 D	2 Dimensional
3 D	3 Dimensional

Greek letters

Symbol	Description	Units
α	Angle	rad
β	Eddy current damping coefficient	-
γ_w	Domain wall energy density	J
δ	Skin penetration depth	m
δ_b	Bending angle	rad
Δ	Change	-
ε	Strain	-
ξ	Shear modulus	-
η	Viscosity	Dyne s/cm^2
θ	Incident angle	rad
λ	Magnetostriction	-
Λ_0	Spontaneous magnetisation	-
λ_s	Saturation magnetostriction	-
λ_w	Wavelength	m
μ	Permeability	H/m
μ_0	Permeability of free space	H/m
μ_r	Relative permeability	-
ρ	Resistivity	Ω.m

σ	Stress	Pa
σ_r	Residual stress	Pa
Φ	Magnetic flux	Wb
χ	Magnetic susceptibility	-

Roman letters

Symbol	Description	Units
A	Area	m^2
B	Magnetic flux density (Magnetic induction)	T
d_c	Inner core diameter	m
E	Energy	J
E	Young's modulus	Pa
e	Spontaneous strain	
f	Frequency	Hz
F	Force	N
H	Magnetic field	A/m
H^*	Critical field of domain nucleation	A/m
HV	Vicker's hardness	N/mm^2
I	Electric current	A
J_f	Current density	A/m^2
K	Anisotropy constant	
K_u	Uniaxial anisotropy	J/m^3
l	Length	m
M	Magnetisation	A/m
m	Magnetic moment	$A.m^2$
m	Mass	kg
N	Number of turns	A/m^2
r	Distance	m
R	Resistance	Ω
R_p	Yield strength	
t	time	s
T_c	Curie temperature	°C

V	Voltage	V
V_l	Volume	M^3
v	Velocity	m/s
W	Weight	N
Z	Impedance	Ω

Table of contents

List of figures

List of tables

1 Introduction

1.1 Motivation

The Matteucci effect in ferromagnetic wires is known to be sensitive to torsional and axial stresses however, the exploitation of this effect in sensing applications has to date been very limited. The Matteucci effect is the generation of voltage pulses at the ends of a ferromagnetic wire when magnetised axially with an alternating field in the presence of torsional stress. This thesis describes a unique approach to utilise the Matteucci effect as a wearable sensor for monitoring changes in curvature. In recent years demand for wearable sensors has increased significantly in many application areas such as medical, entertainment, security and military. It might be that smart wearable sensors technology will revolutionise our life, activities and social interaction like computers have done a few decades back [1]. In medical applications, they can be attached to clothes or even attached directly to the skin for monitoring knee or finger movements, blood pressure, heart rate or body temperature [2, 3]. Flex sensors are prevalent in modern wearable devices, particularly in the area of instrumented gloves used for measuring hand and finger posture. The hand's motor function can be impaired by disease, it is reported that 40 percent of people will at some point be affected by arthritis in at least one hand. Diseases such as Dupuytren's contracture and carpal tunnel syndrome also affect fine motor control and restrict movement. Twenty percent over the age of 65 in the UK suffer from Dupuytren's contracture [4]. Inherited disorders such as epidermolysis bullosa cause a gradual loss of motor function due to generalised skin contracture. The assessment of hand motor function is therefore essential to develop suitable hand treatments. The technologies currently used in hand monitoring devices tend to be expensive fiber optic solutions, complex accelerometer systems or the less reliable resistance or capacitance-based sensors. There is a clear need for a new generation of lightweight wearable devices with improved accuracy, whilst remaining unobtrusive to the user [5].

The aim of this research was to develop a high sensitivity flexible bending sensor, utilising the Matteucci effect, capable of monitoring body posture or bending and that addresses the issues discussed above. To achieve this aim, the following broad objectives were identified: (1) Quantify the dependence of the Matteucci effect for both axial and torsional applied stresses, particularly in shorter wires, not previously reported in literature. (2) Interpret the findings in (1) and propose novel sensor designs and (3) Fabricate sensors and characterise their performance.

In recent years, ferromagnetic amorphous wires have attracted significant interest in sensor applications including Giant Magneto-Impedance (GMI) [6], strain, magnetic field and current sensing [7] due to their remarkable magnetic properties [8]. The unique characteristics of amorphous wire include good flexibility, high fatigue strength, a large Barkhausen jump and a significant Matteucci effect [9]. The Matteucci effect occurs in all ferromagnetic materials but is particularly strong in amorphous wires [10]. This research focussed on using the relative change in the Matteucci voltage as a function of strain as the basis for high sensitivity strain and bend sensors. The Matteucci effect is highly sensitive to different parameters like the magnetic field amplitude and frequency, stress and torsion, and wire dimensions. Therefore, there is the potential to optimise the bending and tensile stress sensitivity by fine-tuning one or more of these parameters [11].

The gauge factor which defines the performance of the strain sensor, is the ratio of relative change in electrical resistance R to the mechanical strain ε. in the case of conventional resistive metal foil strain sensors this number is around two [12]. Wireless strain sensors fabricated from amorphous carbon, designed for high strain applications, have gauge factors of only 0.534 [13]. Amorphous magnetostrictive materials have the potential to form very sensitive micro strain gauges with very high gauge factors. For example, annealed $Fe_{76}(SiB)_{24}$ amorphous ribbon shows a change in differential susceptibility from 750 to 3500 over a stress range from -1.5 to 5 MPa. This equates to an equivalent gauge factor of 4.3×10^4 defined as the fractional change in permeability divided by the strain [14]. In this work, equivalent gauge factors were calculated to enable a comparison with commercial sensors.

To achieve the research objectives, the influence of tensile stress on the Matteucci effect in two types of amorphous wires ($Fe_{77.5}Si_{7.5}B_{15}$ and $Co_{68.15}Fe_{4.35}Si_{12.5}B_{15}$) was studied. Results show how the axial stress significantly affects the Matteucci voltage and that, this behaviour is dependent upon the sign of the magnetostriction constant. Measuring the Matteucci voltage as a function of stress in

magnetostrictive wire, equivalent gauge factors were determined and compared to those of resistive strain gauges.

Based on the findings above, two types of sensor using positive magnetostrictive amorphous wire were developed. The first one used a planar coil printed on to a flexible polyester film for magnetising the amorphous wire. FEM modelling was done to select the best geometry. This sensor was designed to act principally as a strain sensor. A second sensor, consisting of a flexible solenoid for magnetising the amorphous wire, was designed specifically for measuring curvature. The output Matteucci voltage was measured over curvatures ranging from 1.11 to 2.49 rad to assess sensor performance in terms of its sensitivity and linearity.

1.2 Outline

Chapter 2: This chapter presents the basic principles of magnetism relevant to the study of ferromagnetic amorphous wires. Fundamental magnetic equations, magnetostriction theory, the intrinsic properties of ferromagnetic materials and the Matteucci effect are all described including an introduction to amorphous materials, their manufacture, and properties.

Chapter 3: This chapter reviews the academic work on the Matteucci effect. Topics include magnetic characterisation of amorphous wires, magnetic domain imaging, circular magnetisation on negative magnetostrictive amorphous wires, the effects of annealing amorphous wires as well as potential applications for strain and bend sensing.

Chapter 4: In this chapter, a new approach is described for characterising amorphous wires under different conditions of torsion, tensile stress and magnetic field conditions to identify the best candidate for sensing. Results are explained and discussed. Domain imaging has also been done on amorphous wires as they provide useful insights into the magnetic anisotropy of the material.

Chapter 5: This chapter presents two kinds of sensor, strain and bending, based on the Matteucci effect. The strain sensor utilises a planar coil configuration and the bend sensor employs a flexible solenoid to excite the amorphous wire. The chapter describes the sensor fabrication and testing followed by a discussion on the sensor's performance including output linearity and repeatability.

Chapter 6: This chapter is the conclusion of this thesis followed by a discussion on potential avenues for future research.

2 Basic principles of magnetism including the Matteucci effect in amorphous wires

This chapter presents the basic principles of magnetism and fundamental magnetic equations, magnetostriction, Matteucci effect and intrinsic property of ferromagnetic materials as well as an introduction to amorphous materials, their manufacture and properties.

2.1 Fundamental magnetism

A magnetic field is produced whenever there is an electrical charge in motion. This can be due to the electrical current flowing in a conductor or a permanent magnet in which the magnetic field is produced by the orbital motions of electrons.

The Biot-Savart law can be used to determine the magnetic field H at the centre of a circular coil of one turn with radius a meter carrying the current of i Ampers. By dividing the coil into elements of arc length δl each of which contributes δH to the field in the centre of the coil, r is the radial distance. Since by Biot-Savart [15]:

$$H = \sum \frac{1}{4\pi r^2} i\delta l sin\theta \qquad (2\text{-}1)$$

The simplest way to produce a uniform magnetic field in a long thin solenoid, if the solenoid has N turns on a former of l length and carries a current i amperes inside it, the magnetic field inside it will be:

$$H = \frac{Ni}{l} \qquad (2\text{-}2)$$

Ampere's law is equivalent to one of Maxwell's equations of electromagnetism, $\nabla \times H = J_f$ where J_f is the current density of conventional electrical currents.

The magnetic field lines through and around a solenoid are shown in Figure 2-1 [16].

When a magnetic field is applied to a magnetic medium, a magnetic induction (B, in Teslas) is generated. The ratio of magnetic induction to magnetic field strength is called the permeability of the medium (in Hm^{-1}) and defined as Eq.(2-3).

$$\mu = \vec{B}/\vec{H} \tag{2-3}$$

Permeability is the product of relative permeability μ_r and the permeability of free space which has a constant value of $\mu_0 = 4\pi \times 10^{-7} Hm^{-1}$.

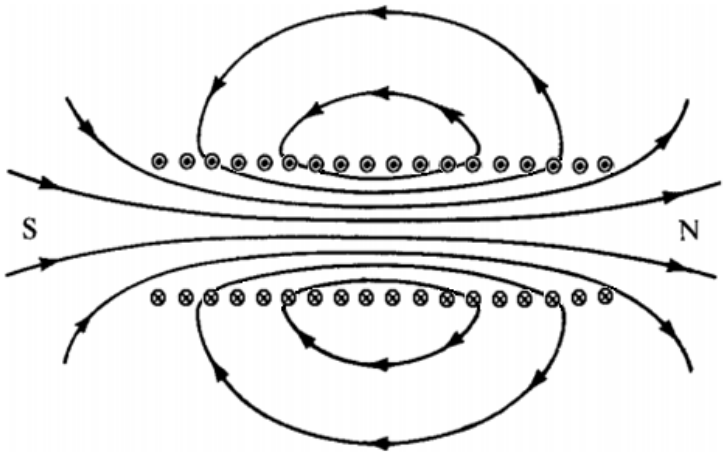

Figure 2-1: Magnetic field of a solenoid (adopted from [1])

$$\mu = \mu_r \mu_0 \tag{2-4}$$

Magnetic regions in a ferromagnetic material are formed by the long-range ordering of permanent magnet dipole moments, even with no external magnetic field applied. Each atomic dipole in the ferromagnetic material has a permanent magnet moment and the magnetisation ($\vec{M}$) is defined as the dipole moment per unit volume. The magnetic induction can simply be rewritten as the sum of magnetisation and magnetic field multiplied by the permeability of free space [15].

$$\vec{B} = \mu_0(\vec{H} + \vec{M}) \tag{2-5}$$

Ferromagnetic materials are broadly divided into two groups, soft and hard magnetic materials based on their coercivity. Broadly hard magnetic materials are those with coercivities above 10 kA/m where soft magnetic materials are those with coercivities of below 1 kA/m. Therefore, where amorphous wires are soft magnetic materials. One of the very important parameters for a soft magnetic material is permeability as it shows how much magnetic induction is generated by the material in the given field and generally speaking depending on applications, the higher the permeability the better the material [17].

Moreover, susceptibility which is a measure of how much a material will become magnetised in an applied magnetic field is defined as:

$$\chi = |\vec{M}|/\overrightarrow{|H|} \quad (2\text{-}6)$$

According to Eq.2-8, where $\mu_0 = 4\pi \times 10^{-7} Hm^{-1}$. The relative permeability of free space is 1. The relative permeability is closely related to the susceptibility and the following equation is always true [15].

$$\mu_r = \chi + 1 \quad (2\text{-}7)$$

According to susceptibility, magnetic materials are divided in three different groups: Diamagnetic, paramagnet and ferromagnetic. Diamagnetic materials are materials which susceptibility is small and negative $\chi \approx -10^{-5}$. Their magnetic respond opposes the applied magnetic field. Paramagnetic materials are the materials which χ is small and positive and typically $\chi \approx 10^{-3} - 10^{-5}$. The magnetisation of paramagnetic is weak but aligns parallel with the direction of magnetic field. The last one is ferromagnetic materials which the susceptibility is positive and much greater than one and typically have values from $\chi \approx 50 - 10000$ [15].

2.2 Maxwell equations

The fundamental electromagnetic equations are Maxwell equations which describe the properties of electric and magnetic fields. These equations provide relations between magnetic field H, the electric field E which is a vector field surrounding an electric charge that applies force on other charges, attracting or repelling them, the magnetic flux density B and the electric flux density D which is a measure of the strength of an electric field generated by a free electric charge, corresponding to the number of electric lines of force passing through a given area.

$$\nabla . D = \rho \quad (2\text{-}8)$$

$$\nabla . B = 0 \quad (2\text{-}9)$$

$$\nabla . E = \frac{\rho}{\varepsilon_0} \quad \text{(Gauss Law)} \quad (2\text{-}10)$$

$$\nabla \times E = \frac{\partial B}{\partial t} \quad \text{(Faraday's Law)} \quad (2\text{-}11)$$

$$\nabla \times B = \mu_0 j + \mu_0 \varepsilon_0 \frac{\partial E}{\partial t} \quad \text{(Ampere's Law with Maxwell corrections)} \quad (2\text{-}12)$$

Eq. (2-8) and (2-9) determines the static electric and magnetic fields. Eq.(2-10) introduces the Gauss law and Eq.(2-11) indicates that a time-varying magnetic field B induces a voltage in a conductor, with E being the electric field. This equation is

based on Faraday's law. In Eq.(2-12) j is the area current density in Ampere per square metre that generates the field and ρ is the charge density in coulombs per cubic metre that generates the electric flux. This equation is based on Ampere's law [18].

2.3 Hysteresis loop

A B-H curve represents the magnetic history characteristic of the magnetic material. It shows the relation between magnetic flux density (B) and magnetic field strength (H) for a particular material. As shown in Figure 2-2 the remanent magnetisation, B_{rem} is marked on the graph and is the magnetisation remaining after the external magnetic field is removed. The magnetic coercivity, H_c, is a measure of the ability of a ferromagnetic material to withstand an external magnetic field without becoming demagnetised.

The saturation induction, B_s, is the state that the material reaches when increases in the applied field has no further effect on the induction level in the material. Mathematically, this happens when $\frac{\Delta M}{\Delta H} = 0$ or the permeability of the ferromagnetic material becomes equal to free space [15].

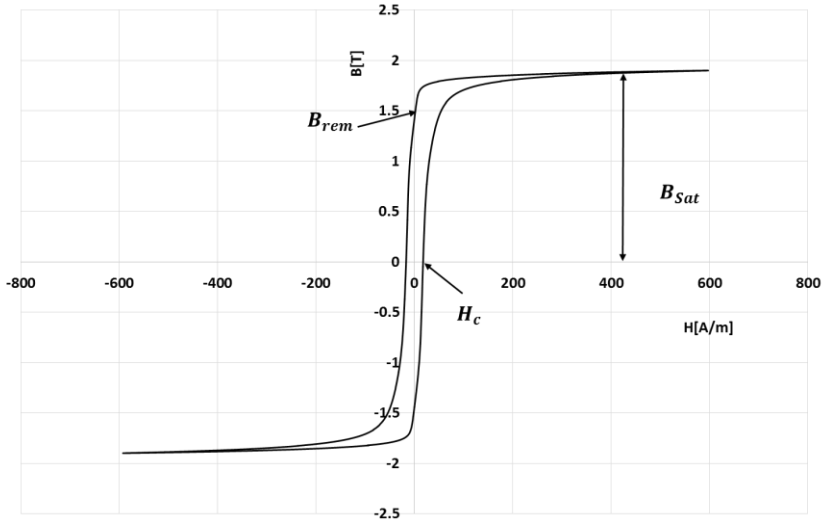

Figure 2-2: A sample B-H curve showing coercivity field, saturation magnetisation and remanent magnetisation for a soft magnetic material

2.4 Magnetic domains

The magnetic properties of amorphous materials are mainly dependent on the domain structure under the influence of external stresses and applied field and tempreture [19]. To investigate these changes it is important to understand their basic nature.

Bozorth [20] discovered that spontaneous magnetisation occurs within ferromagnetic materials and attempted to explain this in terms of large interatomic forces acting between neighboring atomic dipoles in the crystal lattice. Below the Curie temperature, which is the temperature above which materials lose their permanent magnetic properties, these forces can overcome thermal effects leading to an ordered magnetic state. These interaction forces are known as exchange forces. He also proposed the existence of magnetic domains in ferromagnets in 1907. Magnetic moments of atoms are aligned in the same direction in tiny bounded regions called domains. The domains are magnetically saturated and act as regions with uniform magnetisation. However, the direction of alignment can be randomly different from domain to domain [15]. In an unmagnetised specimen, the domains are randomly oriented so that the net magnetisation of the sample is zero. The transition region between domains is called the domain wall which was first suggested by Bloch [21]. In the wall, the orientation of the magnetic dipoles change from the direction of one domain to the direction of the other as shown in Figure 2-3.

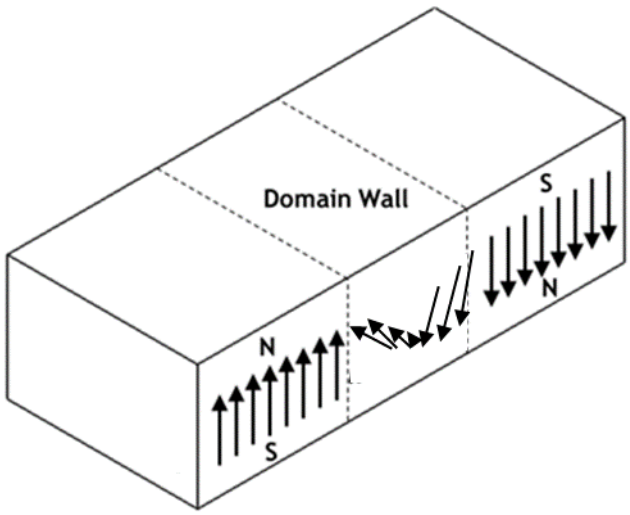

Figure 2-3: Magnetic moment alignment within a 180° Bloch wall [15]

In crystalline materials, the alignment of magnetic moments is energetically more favourable along certain crystallographic directions. This is known as magnetocrystalline anisotropy and results in easy and hard directions of magnetisation [20]. The final domain structure is a combination of the effects of the exchange energy, anisotropy and field energy of the ferromagnetic body [22]. The thickness of the domain wall is influenced by the forces due to the exchange and magnetocrystalline anisotropy energies. The magnetocrystalline anisotropy tend to make the domain wall thinner since the anisotropy energy is the lowest with all moments aligned along crystallographically equivalent axis. In contrast, the exchange energy tends to make the domain wall thicker as the exchange energy is minimized in a ferromagnet when the neighboring moments are aligned parallel [15]. Consequently, as shown in Figure 2-4, there is an equilibrium wall thickness where the domain wall energy is a minimum [15]. The total angular displacement across the domain wall is often 90° or 180 °. The domain boundaries between the neighboring longitudinal domains are 180 ° walls while those between closure domains are 90 ° domain walls as shown in Figure 2-5 [15].

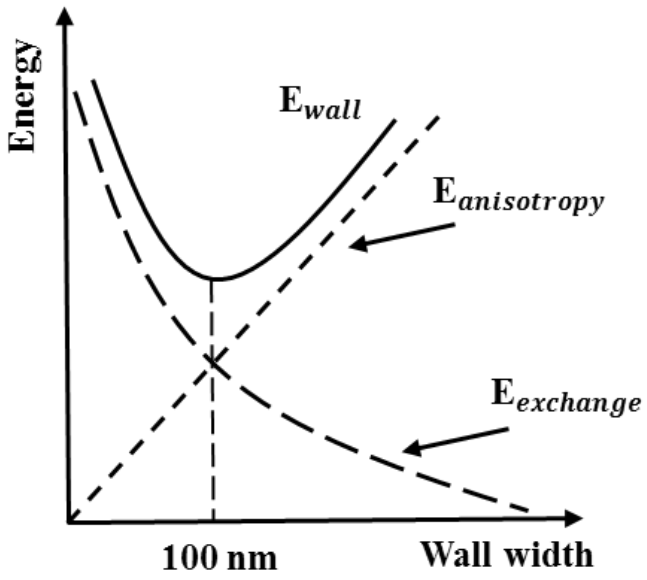

Figure 2-4: Dependence of the wall energy in wall width [15]

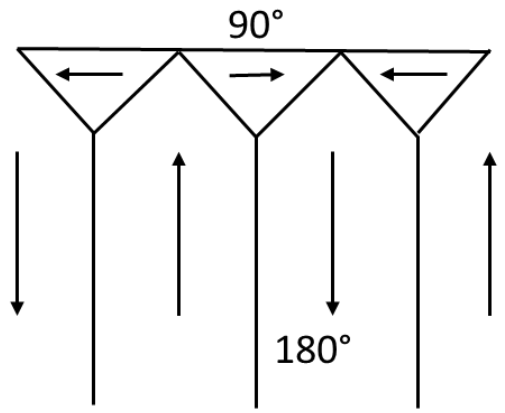

Figure 2-5: 180 ° and 90 ° domain walls [15].

Subsequent to Weiss's work, two main experimental observations confirmed the existence of domains. The first observation was the indirect detection of domains by Heinrich Barkhausen [15]. The Barkhausen effect is the small discontinuous changes in flux density B as the magnetic field H is changing continuously. It was discovered in 1919, when a secondary coil was wounded on a piece of iron and connected to an amplifier and loud speaker. A series of clicks were heard from the speaker which were because of the small voltage pulses induced in the secondary coil. In the magnetised B-H curve, discontinuous changes are shown in Figure 2-6 [15]. The Barkhausen noise is a consequence of small discontinuous changes in domain wall motion [23].

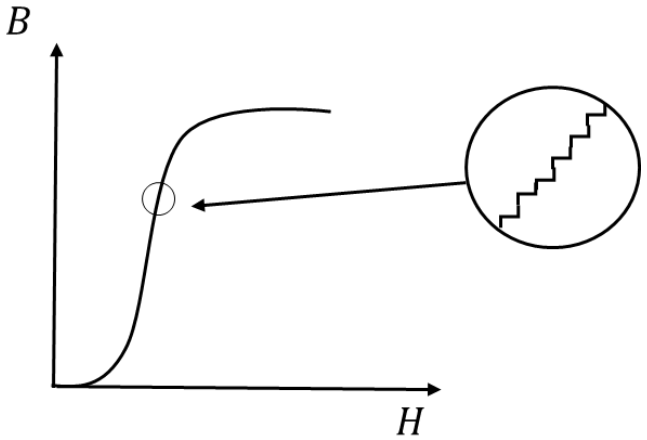

Figure 2-6: Barkhausen discontinuous along the initial magnetisation curve observing by amplifying the magnetisation

The second confirmation was the direct observation of domains by Francis Bitter using Bitter technique [15]. In this method, a very fine magnetic powder was spread over a specimen and patterns of domains were observed under the microscope.

Particles accumulated in the places where the magnetic field gradient is greatest, usually where the domain walls intersect the surface. These particles in modern ferrofluids are usually Fe_3O_4 with diameters of around 10 nm.

2.5 Magnetostriction

Magnetisation is the vector field that expresses the density of permanent or induced magnetic dipole moments in a magnetic material. The magnetisation $\vec{M}$ is defined as the magnetic moment (m) per volume of a solid V_l.

$$\vec{M} = \frac{m}{V_l} \tag{2-13}$$

The magnetisation in some ferromagnetic materials is sensitive to applied stress. In such cases, the material will be subject to a change in the length when magnetised, this is called magnetostriction and was first discovered by Joule in 1842 [24, 25]. He showed that an iron rod increased in length when subjected to a magnetic field. The fractional change in length is defined as the magnetostriction coefficient λ, as shown in Eq.(2-14), where l is the length of material and dl is the change in the length when applying a magnetic field. The value of dl can be positive, negative or zero [26]. If it is positive the material expands, and if it is negative it will contract in length.

$$\lambda = \frac{dl}{l} \tag{2-14}$$

The strain due to the magnetostriction changes with the increase of the magnetic field and reaches a saturation value as by increasing the magnetic field, magnetostrction does not change anymore and domains have been aligned in one direction which is shown in Figure 2-7.

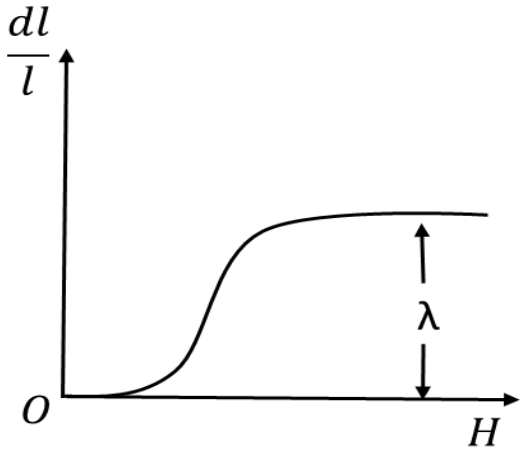

Figure 2-7: Magnetostriction as a function of field intensity [25]

The crystal lattice inside each domain is spontaneously deformed in the direction of domain magnetisation and its strain axis rotates with the rotation of the domain magnetisation thus resulting in the sample's deformation as a whole as shown in Figure 2-8 [18]. Conversely, the influence of stress on the magnetisation is known as the inverse magnetostrictive effect [15]. The dependence of magnetisation on stress may be described in terms of the energy E_σ associated with the stress and direction of spontaneous saturation magnetisation M_s in a domain.

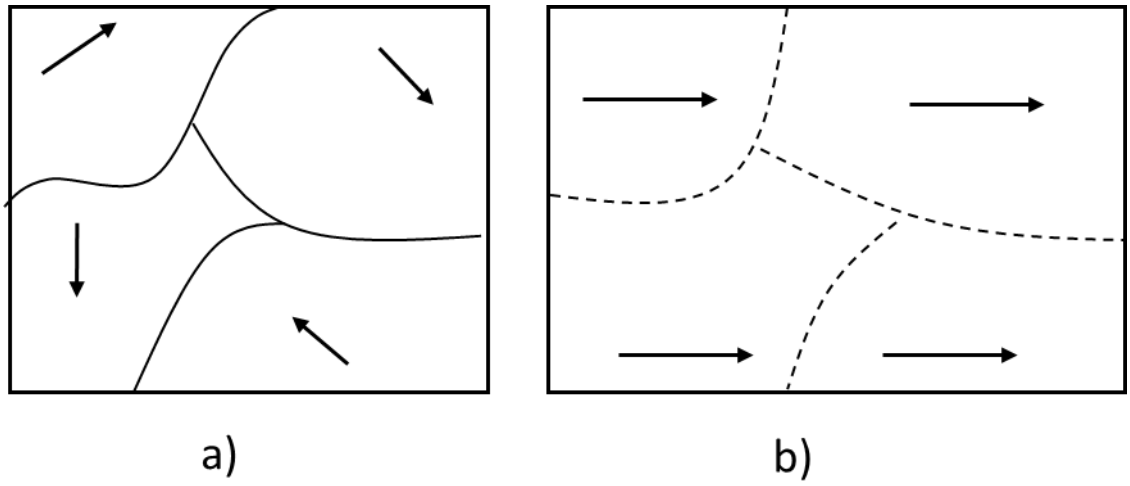

Figure 2-8: Rotation of domain magnetisation and accompanying rotation of the axis of spontaneous strain [18]

$$E_\sigma = \frac{3}{2}\lambda_s \sigma \sin^2 \theta_s \qquad (2\text{-}15)$$

Where λ_s is the saturation magnetostriction, and θ_s is the angle between saturation magnetisation $\overrightarrow{M_s}$ and the stress σ. According to the Eq.(2-15) when $\overrightarrow{M_s}$ and σ are in

the same direction, the magnetic strain energy (magneto elastic energy) is zero, as $\sin^2\theta_s$ is zero it rises up to its maximum value, which is $\frac{3}{2}\lambda_s\sigma$ [15] when they are at right angles. When magnetostriction in amorphous alloys are comparable to those in crystalline alloys typically of the order of parts per million [27].

Easy axis is an energetically favorable direction of spontaneous magnetisation. The magnetisation of domains which are at an angle to the easy axis, will require higher energy to reach saturation magnetisation. This fact is due to the directional dependence of the magnetic material's properties and is known as anisotropy. The energy referred to it is called anisotropy energy. When an isotopic material with disordered magnetic moments above the Curie temperature (T_c) is cooled below T_c, as seen in Figure 2-9 (a), it becomes ferromagnetic with a spontaneous magnetisation. The newly formed magnetic domains have an associated spontaneous strain (e) or magnetistriction λ_0 along particular directions as seen in Figure 2-9 (b). For this isotropic example, the amplitude of spontaneous magnetostriction is independent of the crystallographic direction. Within each of these domains the strain varies with angle θ_s from the direction of the spontaneous magnetisation according to the following relation:

$$e(\theta_s) = e\cos^2\theta_s \tag{2-16}$$

The average deformation throughout this isotopic sample due to spontaneous magnetostriction can be obtained through integration, assuming that all domains are oriented randomly, therefore, all directions are equally likely.

$$\lambda_0 = \int_{-\pi/2}^{\pi/2} e\cos^2\theta_s \sin\theta_s \, d\theta_s = {}^{e}/_{3} \tag{2-17}$$

This is the spontaneous magnetostriction caused by the ordering of the magnetic moments due to the onset of ferromagnetism. We should note that we have assumed an isotropic material where the domains are arranged with equal probability in all directions so although the sample's dimensions have changed its shape remains the same [15].

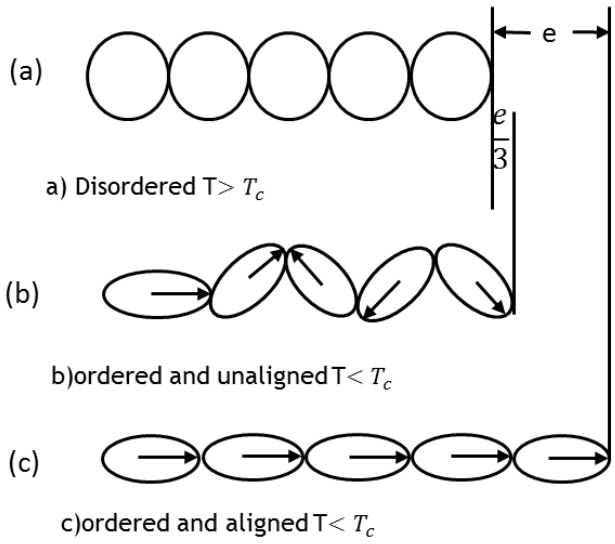

Figure 2-9: schematic diagram illustrating magnetostriction in a) paramagnetic state b) ferromagnetic state demagnetised c) ferromagnetic state, magnetised to saturation [15]

2.6 Amorphous materials

Amorphous metals are solid metallic materials with a disordered structure on the atomic scale. The majority of metals are crystalline in their solid-state which means the structure of atoms is highly ordered. The difference between crystalline and amorphous structure is shown schematically in Figure 2-10.

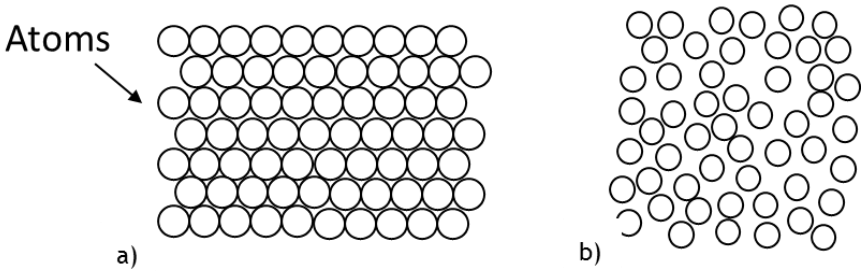

Figure 2-10: Schematic diagram of a) Crystalline solid structure b) Amorphous solid structure in which each circle presents atoms

Duwez [11, 28] had discovered in 1960 that amorphous metals can be prepared by rapid quenching of melts. His experimental technique of splat quenching has been used first to discover and study a wide variety of liquid quenched amorphous metals and their properties. The unique characteristics of amorphous wires have attracted worldwide interest. Amorphous alloys are produced in different shapes like ribbon or wire. Amorphous wires made by the water quenched spinning method have

special advantageous such as mechanical, electrical, magnetic and chemical properties, compared with crystalline alloys as shown in Table 2-1. For example, they have high anti-corrosiveness (zero and negative magnetostriction) enabling the creation of micro magnetic sensors without the need for additional protective coatings. Moreover, they have high electric resistivity which is beneficial to make micro sensor heads operating with high input impedance and low eddy current losses [9].

Compositional dependent properties such as saturation magnetisation, magnetostriction and Curie point usually exhibit similar values in both amorphous ribbons and wires with the same composition. However, it should be pointed out that amorphous wires can exhibit re-entrant magnetic flux reversal with a resultant large Barkhausen effect [29].

Flux reversal in a soft magnetic material is influenced by domain wall motion which is achieved only when the drive field is larger than the coercivity force [30].

Table 2-1: Advantages of amorphous wires [9].

<table>
<tr><th>Mechanical</th><th>Magnetic</th><th>Electrical</th><th>Chemical</th></tr>
<tr><td>High tensile strength (400 kg/mm^2)</td><td>Effective behaviour by current annealing</td><td>High resistivity (130 μΩ-cm)</td><td rowspan="4">High anti-corrosiveness (Co-rich)</td></tr>
<tr><td>High residual stresses</td><td>High domain wall energy density</td><td>Low eddy current losses</td></tr>
<tr><td rowspan="2">High Elasticity (95%)</td><td>High stress relief by annealing</td><td rowspan="2">High impedance</td></tr>
<tr><td>High permeability</td></tr>
</table>

Almost all amorphous materials have atomic composition of T_xM_{100-x} where T represents one or more of the transition metals Iron (Fe), Cobalt (Co), Nickel (Ni), Manganese (Mn), or Chromium (Cr) and M represents one or more of the metalloid or glass former elements, Phosphorous (P), Boron (B), Carbon (C) or silicon (Si). The transition metal content, X, can vary from 75 to 80 percent [16].

In amorphous metallic alloys, the absence of a long-range ordered atomic structure leads to a wide range of characteristics and features which makes these alloys favourable in a variety of applications [31].

2.7 Properties of amorphous materials

Amorphous materials have some special properties compared to crystalline materials which make them unique in many applications. Some of these properties will be discussed below.

2.7.1 Mechanical and electrical properties of amorphous materials

In sensors, mechanical properties like hardness, yield strength, and Young's modulus are important. Typical values are listed for amorphous and crystalline alloys in Table 2-2. The Vicker's Hardness (HV) is a standard measure of the hardness of the material. The Young's modulus (E), which is a mechanical property that measures the stiffness of a solid material, defines the relationship between stress (force per unit area) and strain (proportional deformation) in a material in the linear elasticity regime of a uniaxial deformation. The Yield strength (Rp) is the material property defined as the stress at which a material begins to deform plastically [32].

The differences between the elastic range of amorphous material compared to crystalline one are shown in Figure 2-11. Amorphous alloys have an almost straight characteristic and withstand higher stress. The crystalline alloys have a smaller elastic region before exhibiting plastic flow which is a deformation of a material that remains rigid under stresses of less than a certain intensity but that behaves under severer stresses approximately as a Newtonian fluid. The tensile strength and yield strength are almost identical in amorphous alloys resulting in no plastic flow, however fracture occurs at smaller strains compared to crystalline alloys. For amorphous alloys, elastic strains up to 1 % are feasible however for crystalline metals 0.1 % is the best [31].

Amorphous wires have a disordered, non-periodic structure which leads to an irregular arrangement of atoms, therefore the electrical resistivity is high leading to low eddy current losses [33]. The electrical resistivity of $Fe_{72.5}Si_{12.5}B_{15}$ and $(Co_{0.94}Fe_{0.06})_{72.5}Si_{12.5}B_{15}$ amorphous wires are normally close to 1 Ω/cm.

Table 2-2: Mechanical properties of magnetic materials [31]

Material group	Vickers Hardness (HV)	Yield strength (R_p) (N/ mm^2)	Young's modulus (E) (kN/mm^2)
Metals crystalline	80 - 200	150 - 5000	100 - 230
Metals Amorphous	800 - 1000	1500 - 2000	*Ca.150
Soft ferrites	800	75 - 100	150 Ca.50

*Ca stands for calculated

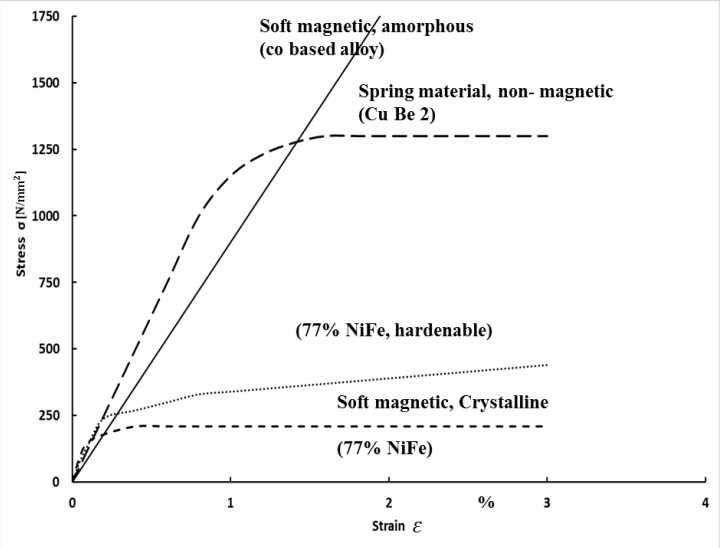

Figure 2-11: Stress-strain curves of several materials (adapted from [31])

2.7.2 Magnetic behaviour of amorphous materials

In-rotating-water quenched ferromagnetic amorphous wires, either in the as-cast state or after treatments, can exhibit very fast magnetisation flux reversal in an external AC-field excitation. This effect can be observed using a pick-up coil to detect the Barkhausen noise or from the induced voltage due to the Matteucci effect [34]. In typical amorphous materials $(Co_xFe_{1-x})_{75}Si_{15}B_{10}$, the magnetostriction coefficient λ_s changes with x from -5×10^{-6} at x=1 to $\lambda_s \approx 35 \times 10^{-6}$ at $x \approx 0.2$ achieving nearly zero values at Co/Fe about x=0.93. The best soft magnetic properties are achieved for nearly zero magnetostrictive Co-rich compositions. On the other hand, Fe-based amorphous wire has different magnetic properties exhibiting a rectangular hysteresis with a large and single Barkhausen

jump[35]. In contrast to Fe-rich wires, Co-rich amorphous wires exhibit non-hysteric behaviour with low coercivity field and large susceptibility. The magnetic properties of amorphous wires are therefore dependent on the composition. Furthermore, internal stresses of the material can be another reason for different magnetic properties. Table 2-3 represents the magnetic properties of amorphous wires by Unitika [9], [36], [37], [25]. M_s(T) is the saturation magnetisation, M_r/M_s is the ratio of remanent magnetisation to saturation magnetisation, K_u(J/m^3) is uniaxial anisotropy $K_u = 3/2\lambda\sigma_r$, σ_r is the residual stress.

Table 2-3: Magnetic properties of as-cast amorphous wires

Composition	Ref	M_s (T)	M_r/M_s	K_u (J/m^3)	λ (x 10^{-6})	σ_r (MPa)	D* (μm)
$Fe_{72.5}Si_{12.5}B_{15}$	[9]	1.3	0.5	2200	25	60	130
$(Co_{0.94}Fe_{0.06})_{72.5}Si_{12.5}B_{15}$	[9]	0.8	0.65	40	-0.1	332	124
	[36], [37]	0.8	-	39	-0.08	-	121
$Co_{72.5}Si_{12.5}B_{15}$	[9]	0.64	0.31	240	-3	54	130
	[36]	0.72	-	256	-5.6	-	123
	[37]	0.64	-	-	-5.6	-	-
$Fe_{77.5}Si_{7.5}B_{15}$	[36]	1.6	-	3187	34.5± 1	-	125
	[36], [37, 38]	1.6	-	-	35	-	-

*D stands for diameter

Amorphous wires have a low coercivity field typically equal to 8 A/m on 60 Hz or less because of the absence of crystalline anisotropy, grain boundaries and structural defects such as vacancies or dislocations. The main factor which increases the coercivity field is the stress due to the magnetostriction effect. Annealing normally causes the coercivity field to be reduced because of the relaxation of internal stresses and zero magnetostriction alloys have the lowest coercivity field due to their reduced stress sensitivity [17]. These results, together with domain observations, were the basis for concluding that, even in the zero magnetostrictive alloys, there still exists an anisotropy that can be influenced by magnetic or stress annealing. Finally, the permeability of As-cast amorphous alloys is low but annealing and magnetostriction can change it [17].

2.7.3 Domain structure of amorphous wires

As it is shown in Figure 2-12, zero and negative magnetostrictive amorphous wires consist of three distinct magnetic regions: the inner core, an intermediate layer, and an outer shell. In the inner core, anisotropy induces the magnetisation vector along the wire axis where one or more domain walls can propagate. A stable single domain state in the inner core is dependent upon the ratio l/d_c given by Eq.(2-18) [9].

$$\frac{l^2}{d_c} = \frac{\pi d_c M_s^2}{8\mu_0 \gamma_w} \tag{2-18}$$

$$K_u = \frac{3}{2}\sigma\lambda \tag{2-19}$$

$$\gamma_w = 4(AK_u)^{\frac{1}{2}} \tag{2-20}$$

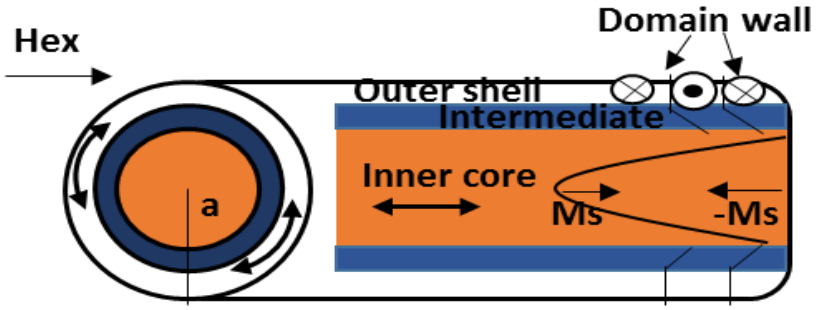

Figure 2-12: Domain structure of slightly negative magnetostrictive amorphous wire (adopted from [39])

where l is wire length, d_c the inner core diameter, M_s the saturation magnetisation and γ_w is the domain wall energy density which is a function of stress and magnetostriction. In addition to the single-core domain, the radial domain structure existing in the outer shell are highly stress sensitive and dependent on frozen-in manufacturing stresses [40, 41]. The outer shell domains typically form radial or circumferential orientations in positive and negative magnetostrictive alloys respectively [41], [42] As a consequence, externally applied stresses strongly affect the magnetic properties of amorphous wires including the Matteucci effect [43, 44].

The complex domain structure and stress sensitivity of amorphous wire results in unique magnetic behaviour and various potential application areas [45].

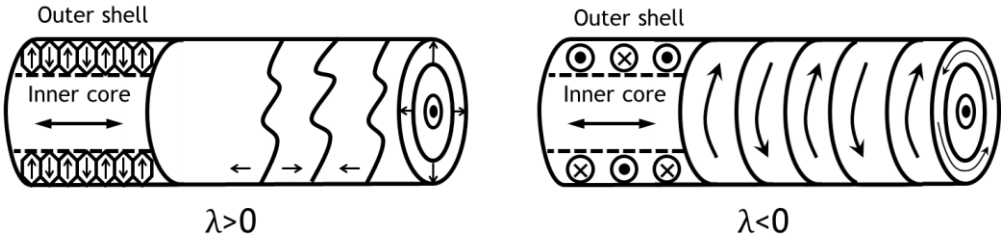

Figure 2-13: Domain model for as-cast amorphous wire with a) positive magnetostriction $\lambda > 0$ b) Negative-magnetostriction $\lambda < 0$ (adopted from [46])

2.8 Matteucci effect

In a ferromagnetic wire, the preferred magnetisation direction can be aligned with a helical path as a function of twisting. If the magnetic strain energy density, related to stress, is bigger than the magnetic anisotropy all the spins are oriented along the helical direction [47]. This amount of stress is called saturation torsion. If the wire was initially demagnetised, it will remain so since both the helix senses are equally populated. An external, longitudinal or circular, magnetic field splits the helix senses and produces a magnetisation transition in the easy sense. Then a macroscopical magnetisation with longitudinal and circular components will appear. In twisted wires, the susceptibility tensor possesses two non-diagonal terms $X_{z\emptyset}$ and $X_{\emptyset z}$:

$$\begin{pmatrix} M_z \\ M_\emptyset \end{pmatrix} = \begin{pmatrix} X_{zz} & X_{z\emptyset} \\ X_{\emptyset z} & X_{\emptyset\emptyset} \end{pmatrix} \begin{pmatrix} H_z \\ H_\emptyset \end{pmatrix} \quad (2\text{-}21)$$

The $X_{\emptyset z}$ term relates to circular magnetisation in a longitudinal magnetic field. When the amplitude of the longitudinal field changes, a variation of circular magnetisation appears, and consequently a longitudinal electric field is induced. This effect is called the Matteucci effect. The $X_{z\emptyset}$ relates to longitudinal magnetisation in a circular magnetic field which is known as the inverse Wiedemann effect [47]. However, the Matteucci effect does not appear just in twisted wires, as Hernado (1973) has clarified that the Matteucci effect will appear in any wire which presents a circular magnetisation to a longitude field in the susceptibility tensor. In fact, the Matteucci voltage appears in non-twisted wires as well because of the random twisting stresses introduced in the wire during solidification [48]. The Wiedemann effect is the inverse of the Matteucci effect. Discovered in 1858, a ferromagnetic wire undergoes spontaneous twisting when subjected to an

alternating axial magnetic field whilst passing a DC current. Figure 2-14 shows the combination of ac current J_1 passing through the solenoid coil and current J_2 passing through the wire. The interaction of the wire's magnetostriction with the combination of linear and circular magnetic fields gives rise to torsional oscillations. Memory configuration designs exhibited in the "twistor" matrix is an example of an application of the Wiedemann effect.

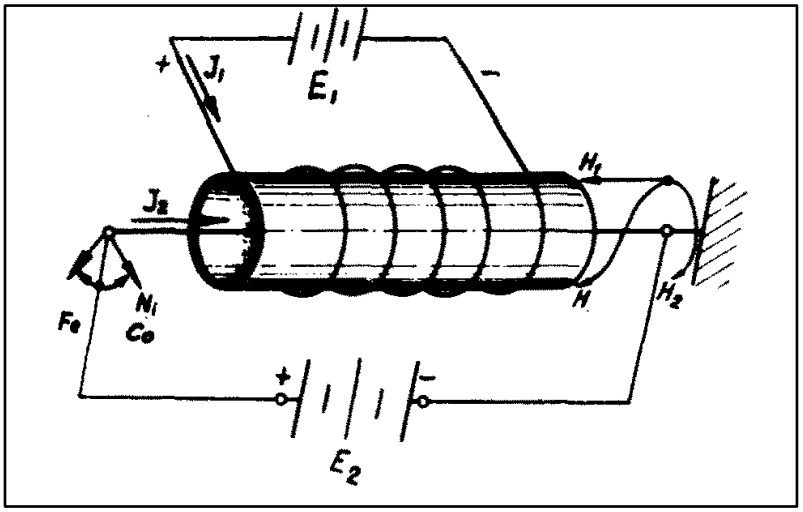

Figure 2-14: Wiedemann effect [49]

The Matteucci effect in amorphous wires was thought to be related to magnetostriction and domain wall propagation due to large Barkhausen effect [50] but it also occurs in nearly zero magnetostrictive amorphous wires which does not exhibit large Barkhausen effect. Therefore, the Matteucci effect is a phenomenon which may occur regardless of the presence of magnetostriction, and the voltage across the wire ends (the Matteucci voltage) is described very simply in terms of the time rate of change $\frac{\partial \Phi_\theta}{\partial t}$ of the circumferential flux Φ_θ in the wire, according to Maxwell equation $\nabla \times \mathrm{E} = -\frac{\partial B}{\partial t}$. The circumferential flux is expected to be closely related to the domain structure in the outer shell of the amorphous wire [50].

Mohri et al. [48] investigated the mechanism of the Matteucci effect and Large Barkhausen effect in amorphous wires by domain observation. The Matteucci voltage e_p' is generated at the ends of the amorphous wire by applying an AC field of more than 7.9 A/m at frequencies from 0.01 Hz to 10 kHz. The magnitude of e_p' is obtained by using the relation of $\nabla \times \mathrm{E} = -\frac{\partial B}{\partial t}$ and Stokes' Theorem. The Matteucci voltage is calculated from the following equation:

$$e_p' = 2DlN_w M_s B_s \overline{\sin\theta}\,(H^* - H_0)/\beta \qquad (2\text{-}22)$$

Where l is the wire length, D is inner core diameter, B_s is the saturation flux density, N_w is the number of domain walls propagating through the pick-up coil, H^* is the critical field of domain nucleation for the flux reversal, H_0 is the critical field of domain propagation, M_s is the saturation magnetisation, β is the eddy current damping coefficient, $B_s \overline{\sin\theta}$ is the resultant component of flux density perpendicular to a plane including the wire radius due to the random twisting stresses. Eddy currents are loops of electrical current induced within conductors by a changing magnetic field in the conductor according to Faraday's law of induction. Eddy currents flow in closed loops within conductors, in planes perpendicular to the magnetic field.

Mohri et al. [51] also developed an equation for the Matteucci effect in amorphous ribbon. To explain the Matteucci effect, Figure 2-15 shows the corresponding domain model. The easy magnetisation axis in a twisted ribbon is ∏/4 rad at a half thickness and -∏/4 rad at another half-thickness, leading to two ∏ rad walls (solid line and dotted line) simultaneously propagating along the ribbon axis in each half thickness of the ribbon with the speed $v = \frac{dx}{dt}$. From the relation of $E = -\frac{\partial B}{\partial t}$ or $\oint E_x\, ds = -\iint_s B_y ds$, the induced voltage at the ends of the ribbon with length l and width W is obtained by integration of magnetic field along the paths C1 and C2 as shown in Figure 2-15:

$$e = \sqrt{2}\, B_s h N_w l v \qquad (2\text{-}23)$$

Where B_s is the flux density and N_w is the number of the domain walls per unit length and h is the height of domain inner core.

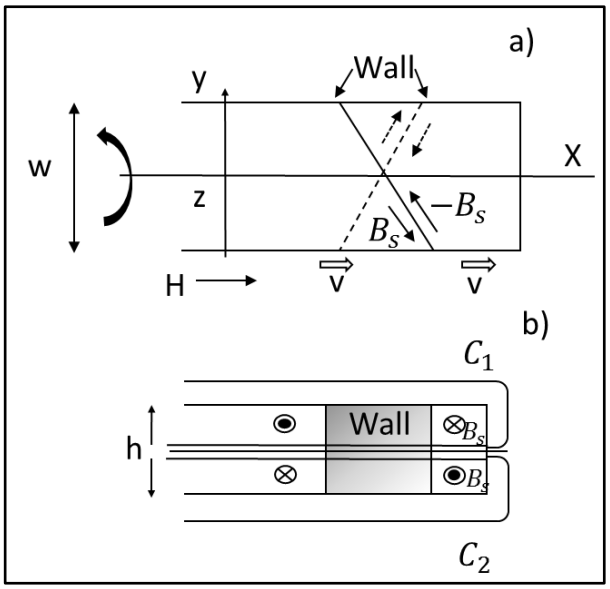

Figure 2-15: Domain model [51]

The Matteucci effect with sufficient signal to noise ratio, for sensor applications, is realized only by using amorphous magnetostrcitive alloys because of its outstanding elasticity, high flux density, high resistivity, and material uniformity [51].

The Matteucci effect was discovered in 1847 and explained in terms of magnetostriction, however a full explanation was not forthcoming. Skorski [49] performed measurements to study the Matteucci effect on 3 mm thick, 300 mm long iron wire. Results showed that the Matteucci voltage is induced by torsion leading to a shift of magnetisation along a helical path. It was shown that increasing the frequency of magnetisation increases the amplitude of the output Matteucci voltage and concluded that the Matteucci voltage depends directly on the rate of change of the magnetisation. It was asserted that the Matteucci effect appears in both ferromagnetic and nonconductive ferrite materials and can be observed in large plates as well as wires.

It was previously reported by Takamure et al. that CoSiB amorphous wire with negative magnetostriction exhibits a large Barkhausen effect as well as a Matteucci voltage but ten times greater than that of Fe-based wire [52]. According to Takamure et al. [52] the Matteucci effect appears in long, thin, magnetic samples which are magnetised with an alternating field. If the magnetisation vector is at an angle relative to the length direction, a voltage will be induced across the ends of the sample. It was proposed that a component of the magnetisation vector in the inner core of amorphous wire that gives rise to large Barkhausen jumps occurs at an angle relative to the length direction thus contributing to the Matteucci voltage.

The Matteucci voltage component due to the inner core magnetisation [53] is illustrated in Figure 2-16. Domain walls in amorphous wires were described as cone-shaped walls. From Figure 2-16, using cylindrical coordinates in which the z-direction is along the wire axis a cone-shaped domain wall model was developed with a cone length l, radius R propagating with velocity v. The generated Matteucci voltage is obtained by Eq.(2-24):

$$e_{pm} = B_\theta v R l \tag{2-24}$$

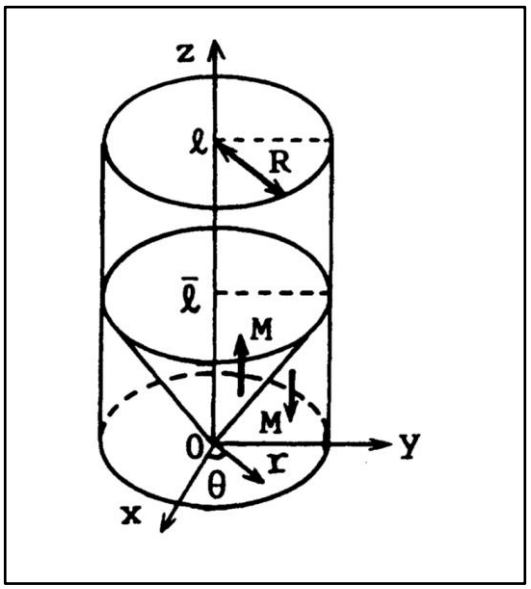

Figure 2-16: Model of domain wall in an amorphous wire [52]

By referring to Eq.(2-24) Takamure et al. proved that the Matteucci voltage is proportional to the domain wall velocity v, the inner core radius R and the wall length l [52]. It was shown that Matteucci voltage has the important feature of being proportional to the length of the domain wall, in contrast to the voltage pulses due to Barkhausen jumps [52]. The torsion annealing was done on 200 mm long Co-based amorphous wire and it caused M_r/M_s to increase therefore indicating that the inner core diameter had increased. It was also shown that as a result of annealing under torsional stress of Co-base wire, an anisotropy is induced at ∏/2 rad to the direction of torsion. Consequently, the circumferential component of the flux density is increased and the inner core radius is made larger.

The mechanism of the Matteucci effect in negative-magnetostrictive amorphous wires were discussed in [50] by considering the magnetic domain model and B-H

curve measurements for the case of circular magnetisation. Three kinds of amorphous wires FeSiB, CoSiB and FeCoSiB with diameters of 50 and 120 μm were investigated [50]. It was shown that in an amorphous wire with negative magnetostriction, the Matteucci effect occurs due to changes in circumferential flux as a result of domain changes in the outer shell.

Fevieres et al. [54] showed that the magnetic domain structure observed by the Bitter technique reveals that the anisotropy changes direction rotating gradually from its original longitudinal direction into a ∏/4 rad helix. As a result of this helical anisotropy, whenever the sample is subjected to a longitudinal magnetic field, the Matteucci effect (ME) appears at both ends of the sample. This ME is produced by the magnetic flux induction variation in the circular direction which is proportional to the magnetisation's circular component derivative. Similarly, Favieres et al. showed when the sample is subjected to a circular magnetic field, a variation of longitudinal component of magnetisation is detected which is called the Inverse Wiedemann Effect (IWE) [54]. Figure 2-17 shows a schematic representation of both effects IWE when a helical magnetic anisotropy is presented in a cylindrical sample.

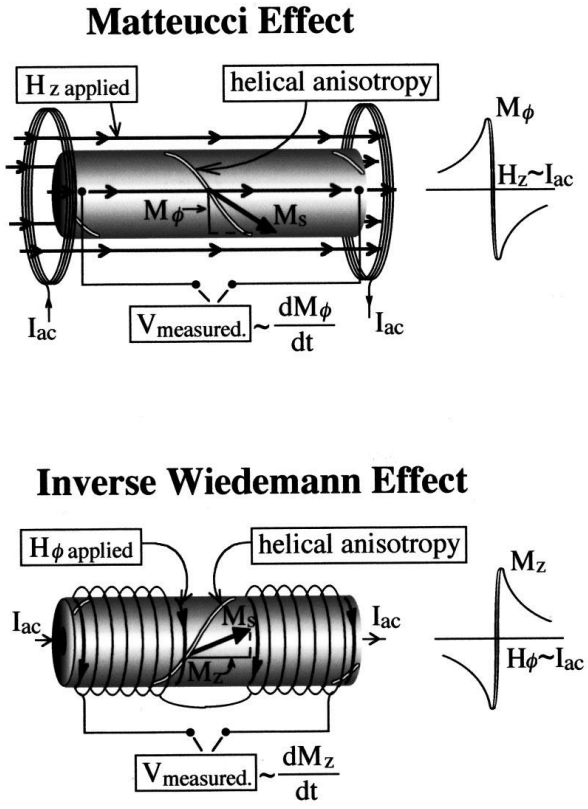

Figure 2-17: Schematic representation of both ME and IWE when a helical magnetic anisotropy is present in a cylindrical sample [54]

Therefore according to Eq.(2-21),

$$M_{\emptyset} = X_{\emptyset z} H_z \tag{2-25}$$

for the Matteucci effect since $H_{\emptyset} = 0$ and

$$M_z = X_{z\emptyset} H_{\emptyset} \tag{2-26}$$

for the inverse Wiedemann effect since $H_z = 0$.

The Matteucci effect can be observed in amorphous wires without torsion because of random twisting stresses induced in the wire during the solidification process [38]. A normal arrangement for detecting the Matteucci effect is with the applied field produced with an external coil along the wire axis, but another arrangement requiring no coil, uses AC current along the wire to produce a circumferential field at the wire surface which is shown in Figure 2-18. If it is sufficiently large, it can induce core switching, resulting in a Matteucci voltage (e_M). However, it can be detected only in Co-based wires with a circumferential magnetised region in the surface layer [38].

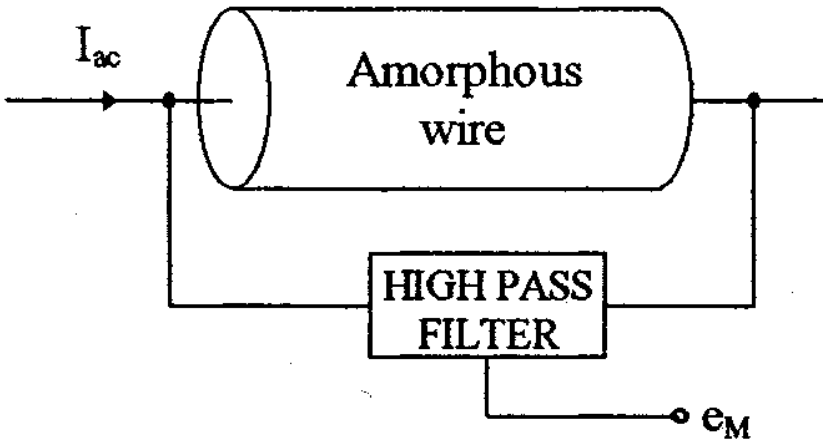

Figure 2-18: Matteucci effect in amorphous wire [38].

To conclude, a brief overview has been provided on amorphous wires and the basic theory of magnetism in this chapter. Amorphous materials, their mechanical, electrical and magnetic properties have been described. The magnetic field, permeability and hysteresis in amorphous materials as well as magnetostriction and the Matteucci effect were defined. This will provide the basic understanding required for some of the concepts described in later chapters.

3 A review on the Matteucci effect in amorphous wires and its use in sensor applications

3.1 Introduction

This chapter reviews previous work on the Matteucci effect and its application to sensors. Details include the magnetic characterisation of amorphous wires, magnetic domain imaging, B-H curve measurements and the effect of annealing on amorphous wires as well as potential applications for strain and bending sensing.

3.2 Applications utilising the Matteucci effect

Amorphous alloy sensors are divided into two main groups, magnetometers using zero-magnetostrictive alloys and stress sensors using highly magnetostrictive alloys. The latter is further divided into three sub-groups, sensors utilising ultrasonic propagation effect, the stress magnetic effect, and the large Barkhausen and Matteucci effects. Amorphous wires have become more attractive in the last few years for the development of the sensing devices able to measure quantities such as displacement [55], acceleration [56], stress [57], and torsion [58].

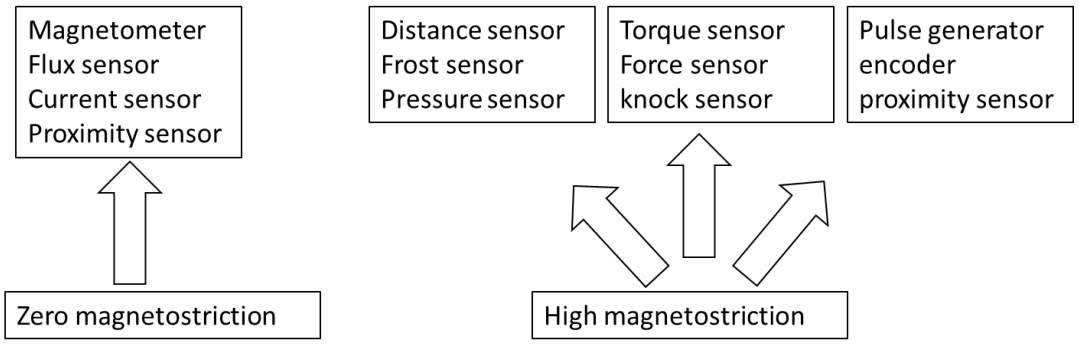

Figure 3-1: Amorphous alloy sensor applications [59]

Mohri et al. [10] introduced a pulse generator sensor using $Fe_{77.5}Si_{7.5}B_{15}$ and $Fe_{77.5}Si_{7.5}B_{15}C_1$ compositions with 100-200 μm diameter wire made by Unitika. Sharp pulses with extremely small jitter were induced at the pickup coil due to the

large Barkhausen jumps, and between both ends of the wire due to the Matteucci effect, for external AC fields ≥ 0.78 A/m at 0.01 Hz - 10 kHz frequency. These pulse generators can be used to construct high-resolution rotary encoders in combination with multiple ring magnets. He reported that those amorphous wires induced sharp and stable voltage pulses at the pickup windings due to the large Barkhausen jump and 6 V/cm^3.Oe at the end of the wire due to the Matteucci effect. These wires induced higher voltage pulses than those seen in twisted amorphous ribbons [51] or Wiegand wires which are a low carbon Vicalloy, a ferromagnetic alloy of cobalt, iron, and vanadium. Initially, the wire is fully annealed [60]. Figure 3-2 represents the voltage pulse shapes of the pulse generator using amorphous wire, amorphous ribbon of $Fe_{79}Cr_2B_{17}Si_2$ and Wiegand wire. It can be clearly seen that sharpness and stability of pulses in amorphous wire are the best.

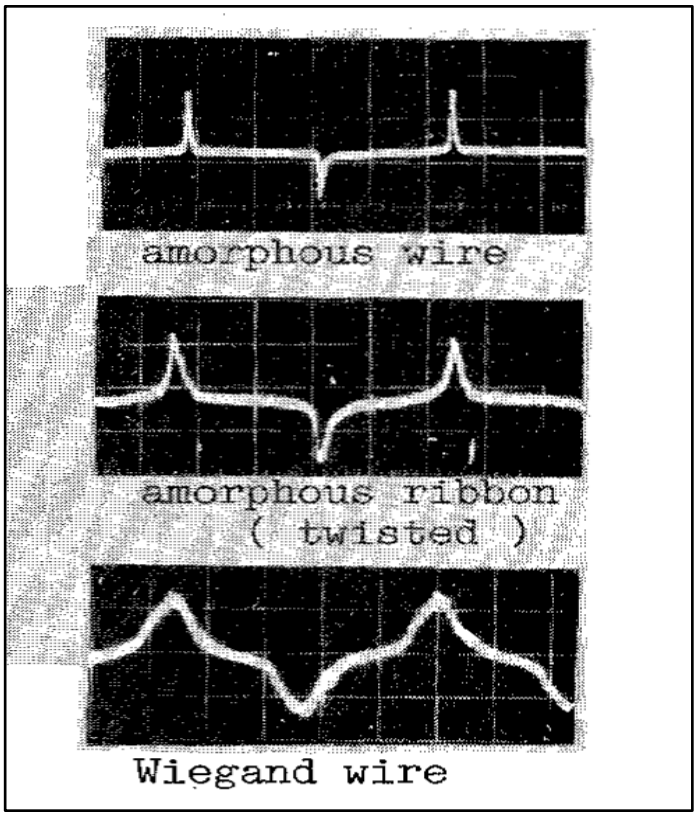

Figure 3-2: Pulse wave shapes for three different materials magnetised with 20 mm long coils with 500 turns [10]

Lassow et al. [56] developed an angular accelerometer transducer utilising the Matteucci effect in the amorphous wire. The proposed sensor had low impedance output and low frequency response as compared to piezoelectric accelerometers without any requirement for extra electronic circuitry. He confirmed that the

Matteucci effect is advantageous due to the transduction of magnetic to electrical signals without the requirement of pick up coils. As Figure 3-3 shows when the accelerometer rotates, the twist of the wire influences the magnetic properties of the wire. For the frequencies below the resonant frequency, the angular acceleration of the mass rotating about the axis of the wire will be the same as the acceleration of the accelerometer's base and the Matteucci voltage across will show the vibratory input angular acceleration. The $Fe_{77.5}Si_{7.5}B_{15}$ amorphous wire with 125 μm diameter and 30 cm long was used in these experiments. The wire was magnetised with a 200 turn, 52 mm long solenoid coil and the output Matteucci voltage was detected directly across contacts without further amplification. The proposed accelerometer displays superior low acceleration results and a frequency response less than approximately 33 $\frac{\text{rad}}{s^2}$ and 3 Hz respectively compared with commercially available piezoelectric accelerometers. Moreover, he declared that the proposed accelerometer is robust, easy to construct and has high signal to noise ratio with low impedance output and does not require supporting equipment for signal conditioning and impedance conversion.

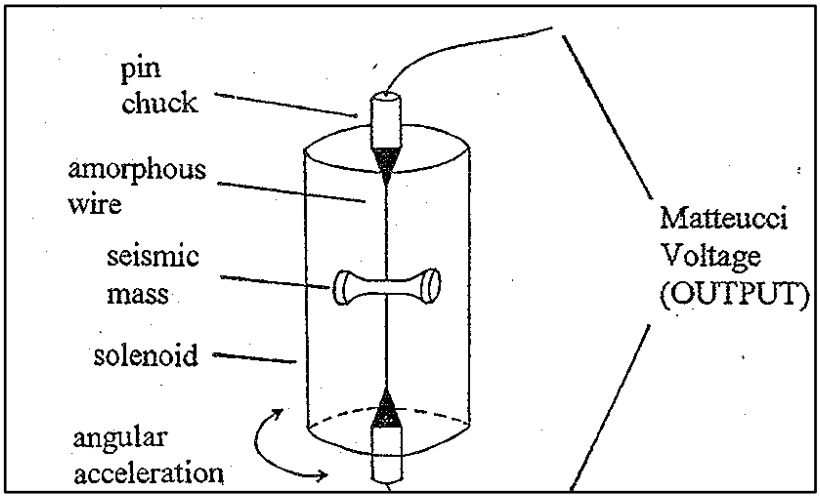

Figure 3-3: Schematic representation of an angular accelerometer, the magnetising winding is omitted for clarity [56].

Fosalau [38] developed a circular displacement sensor based on the Matteucci effect with $Fe_{77.5}Si_{7.5}B_{15}$ amorphous wires to measure angle and force. The schematic diagram of the sensor is shown in Figure 3-4 in which a 55 mm long amorphous wire was connected between two metallic pieces, one fixed and one mobile, the latter connected to a moveable shaft with both axial and circular motion. When the shaft rotated, the wire was subjected to torsional strain and

generated a Matteucci voltage between the two metallic pieces. A winding precision potentiometer was employed to measure the torsion angle. The output voltage of the potentiometer had a linear relationship with the angle of the cursor. It was shown that when the intensity of the magnetic field H exceeds critical field H^*, the output voltage value depends on the diameter of the wire and temperature. The sensor was characterised for sinusoidal and square waves and the result showed that the sensitivity of the sensor for square waves was 25% greater than for the sine wave. Moreover, at low frequencies the amplitude of the output pulses was small, stable and linear. At higher frequencies, the linearity of the sensor deteriorated as the permeability of the amorphous wire is frequency-dependent. This dependency is also affected by the wire diameter. It was also shown that the frequency limit for the wire increases as the wire thickness reduces. The sensor sensitivity depends on frequency variation except at higher frequencies when the sensitivity becomes approximately constant. This sensor had good sensitivity (approximately 5 mV/deg) and acceptable linearity for the range of operation of 2∏ rad.

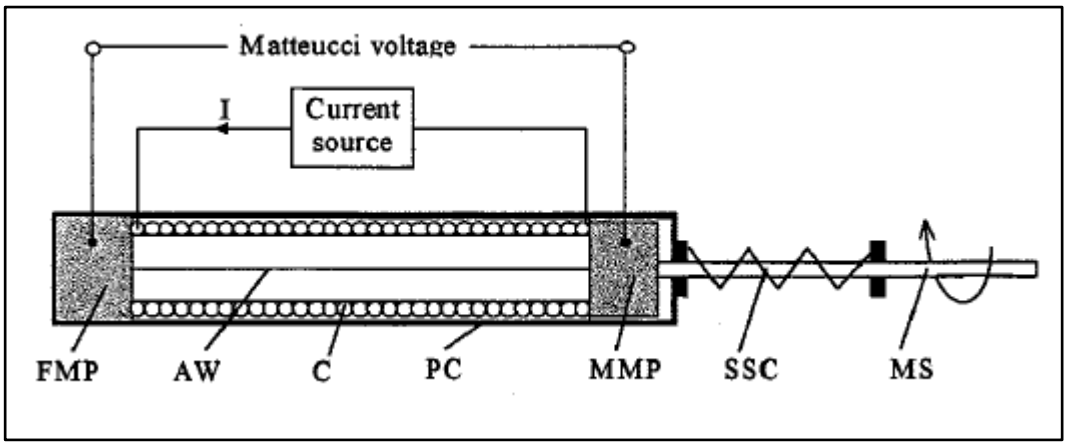

Figure 3-4: Schematic representation of the circular displacement sensor, FMP is fixed metallic piece, MMP is mobile metallic piece, AW is amorphous wire, C is coil, PC is plastic case, SSC is spring for stress control, and MS is mobile shaft [38].

Dimitropoulos et al. presents a micro-fluxgate sensor utilising conventional and glass-covered $Fe_{77.5}Si_{7.5}B_{15}$ amorphous wires in combination with a planar coil [61]. The amorphous wires were mounted on to the planar coil by soldering the ends to create a 30×60 mm sensor. The wire was current annealed prior to mounting in order to optimise the inductive response of the wire. Figure 3-5 shows the pair-coil design which was chosen to minimise the sensor head dimension and to obtain the generation of a symmetric magnetic field parallel to the coil plane. Each winding was 0.3 mm wide and 20 μm thick and were separated by a 0.2 mm air gap.

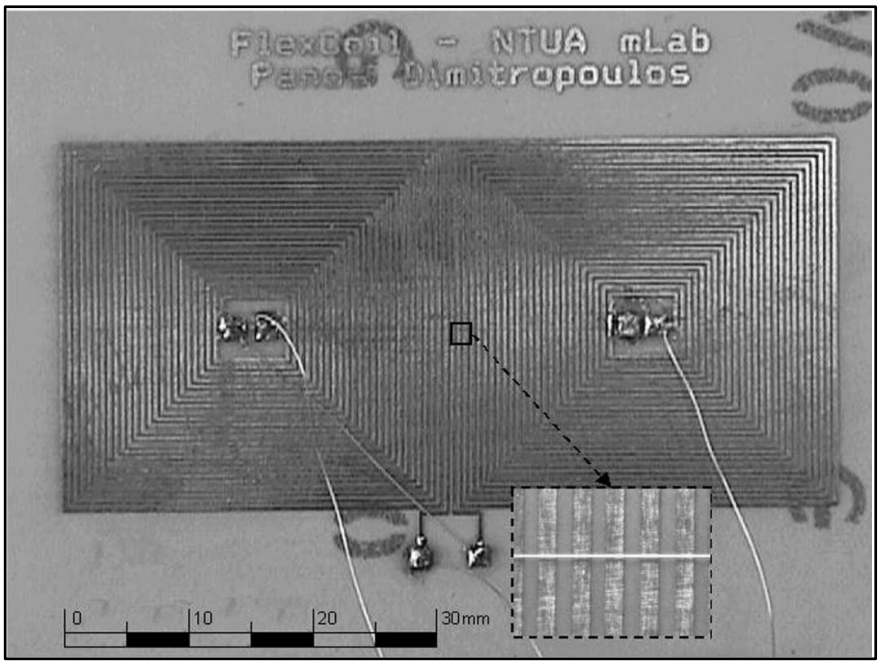

Figure 3-5: The fluxgate sensor head. The glass-covered amorphous fibre core is visible in the centre of the head [61] . 60×30 mm head dimension

Results show that the proposed sensor had 74 kV/T sensitivity before amplification. The glass-covered wires were preferable because they exhibited a Matteucci voltage even in smaller sizes down to 5 mm. The Matteucci voltage was higher in conventional wire than glass-covered one and this may be because of the larger wire diameter. However, the raw Matteucci voltage was amplified through amplification and a buffering stage [61].

Fosalau et al. [62] developed a novel current sensor to measure the Matteucci pulse amplitude across the ends of a twisted magnetic amorphous wire carrying an AC current. To obtain this effect a 125 μm thick, 300 mm long wire was wound around a 300 mm long cylindrical conductor, thus creating the axial orientation with respect to the field and, at the same time, having the possibility of modifying its length based on the study requirements (see Figure 3-6). The following sets of measurements were performed which are listed in Table 3-1 [62]: Two different conductor diameters (10 mm and 6 mm),

Three different wire lengths (5 cm, 30 cm and 45 cm),

Three different wire torsions (5π, 15π, and 25π rad/m).

A sinusoidal current with a total harmonic distortion (THD) of 0.2 %, and a square wave current.

Table 3-1: List of measurements

Conductor diameter (mm)	Length (cm)	torsion (rad/m)
10	5	5π
6	30	15π
	45	25π

The sensor frequency range was between 50 Hz to 1 kHz. The experiments were made at two ambient temperature values: 20 ºC and 70 ºC. The latter was conducted within an electric oven whose temperature control accuracy was better than ± 2%. The wires were tested in an as-cast form.

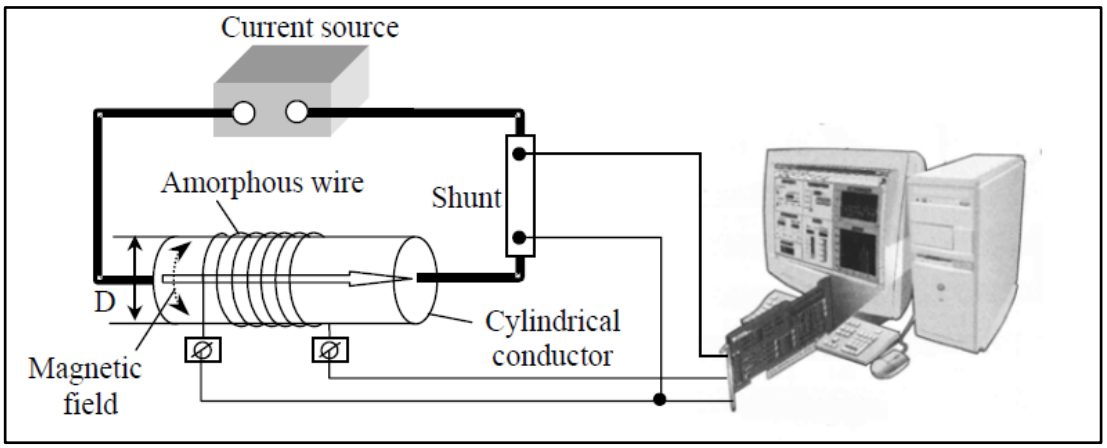

Figure 3-6: Experimental set up for the study of sensor characteristics [62].

It was demonstrated that sensor's sensitivity increases with increasing the frequency due to faster flux variance in this region, leading to sharp pulses with higher amplitude. When the current goes to a squared shape, the magnetic field reverses faster than the sinusoidal case (this is due to bandwidth of the square signal which theoretically is infinite) and the sensitivity also goes higher. Moreover, the sensitivity stays constant up to 600 Hz and above that dramatically decreases, probably caused by two aspects: i) the loss of magneto elastic energy with frequency inside the wire and ii) the low-pass filter effect of the coil. Thirdly, the wire length becomes important when it is smaller than a critical value which usually depends on wire diameter. For instance, for a wire diameter of 125 μm, the critical length is approximately 7 cm. For wires whose length drops under 7 cm, a strong

reduction of the sensitivity and some output instability are expected. The experiments showed sensitivity decay over three times in the 5 cm case compared to a 30 cm long wire. Finally, as the torsion increased, the pulse amplitude increased as well. To conclude, the experimental sensor had the advantage of low price, simple construction, robustness, good linearity, accuracy and low dependence on temperature [62]. Furthermore, effect of waveform on the Matteucci effect was discussed in this paper.

3.3 Giant magneto-impedance (GMI) effect

As Velázquez et al. calculated in [63], the maximum relative change in impedance originating from the magneto-inductive voltage is given by:

$$\frac{Z_{max}}{Z_{min}} = \left\{1 + \left[\pi\mu_0 R^2 \chi_{\phi max} v/(2\rho)\right]^2\right\}^{1/2} \quad (3\text{-}1)$$

The variation in impedance increases with circular susceptibility χ_ϕ, radius of the wire R, frequency v of the current through the wire and increases with increasing resistivity ρ.[63] Some technological applications based on this effect are reported in [64] and [65]. This relative change in impedance is restricted to the low frequency range because of the skin effect at higher frequencies. An AC current flowing along the wire creates an inhomogeneous AC magnetic field. In the case of very high frequencies, the penetration of such a field is confined to a surface shell due to the skin effect giving rise to changes in ohmic and inductive components of the impedance [66, 67]. The skin penetration depth δ can be expressed as:

$$\delta = \left(\frac{\rho}{\mathrm{X}\phi v}\right)^{1/2} \quad (3\text{-}2)$$

The total impedance Z is related to the penetration depth through the expression:

$$Z = 1/2R_{dc}(kR)\left(\frac{J_0(kR)}{J_1(kR)}\right) \quad (3\text{-}3)$$

Where R_{dc} is resistance when v=0 and J_i are the Bessel functions with k= (1+i)$(\frac{R}{\delta})$. According to Eq.(3-3), changes in impedance can be produced by the modification of the resistivity and permeability [68]. The circular permeability is strongly reduced by the presence of an external biasing magnetic field. Therefore, the

penetration depth increases with the external field and the total impedance decreases simultaneously.

Nabias et al. investigated the influence of bending parameters on the GMI effect in 100 μm Co-rich wires [6]. Changes in the values of key parameters associated with the GMI effect have been investigated under bending stress. These parameters included the GMI ratio, the intrinsic sensitivity, and the offset at a given bias field. The experimental results have shown that bending the wire resulted in a reduction of GMI ratio and sensitivity. It has also been shown that the effect of bending seemed to be reversible and repetitive. However, Knobel et al. declare that more work is necessary to achieve a better understanding of the physical phenomena related to bending and compression [6].

3.4 Characterising amorphous wires

Meydan has studied the influence of tensile, compressive and torsional stresses on the magnetic properties of as-cast highly positive and nearly zero magnetostrictive amorphous wires [69]. Experiments were conducted on 30 cm lengths of the following types of amorphous wires:

1- $Fe_{77.5}Si_{7.5}B_{15}$ positive magnetostrictive 125 μm thick amorphous wires,
2- $(Co_{94}Fe_6)_{72.5}Si_{7.5}B_{15}$ nearly zero magnetostrictive, 130 μm thick amorphous wires.
3- $(Co_{94}Fe_6)_{72.5}Si_{7.5}B_{15}$, 100 μm thick amorphous wire which was annealed at 510 ºC for 1 hour.

It was shown that by applying tensile and compression stress on the wires the Matteucci voltage decreases as a result of cancelling the helical magnetisation. Furthermore, Fe-based amorphous wires were found to be more sensitive to the change in Matteucci voltage due to tensile, torsion and compression compare to Co-based amorphous wires. This behaviour can be attributed to the increase in the helical anisotropy component due to the alignment of magnetisation vectors in a spiral magnetisation path [69].

Lassow studied the effect of tensile, compressive and torsional stresses on the magnetic properties of annealed and as-cast highly magnetostrictive and nearly zero magnetostrictive amorphous wires for different frequencies and magnetisation levels to design an angular acceleration transducer [32]. The author claimed that a

simple, rugged, potentially inexpensive novel linear and angular accelerometer by using amorphous materials exhibit good overall characteristic with low impedance output and superior low frequency as compared to commercial piezoelectric accelerometer without the requirement of costly impedance conversion vibration preamplifiers.

Kane et al. studied the influence of torsion during current annealing on the Matteucci voltage in amorphous wires [70]. Positive magnetostrictive $Fe_{77.5}Si_{7.5}B_{15}$ amorphous wires with 125 μm diameter were used in these experiments. The wires were annealed using two methods, method 1 passed a 500 mA AC current for 1 minutes and method 2 passed a 300 mA current for 10 minutes, both with 3.71 rad/m (rad per meter) twist. Amorphous wires were magnetised by a 120 mm long, 300 turn solenoid. Tensile stress was applied by loading the sample and the Matteucci voltage was obtained by connecting oscilloscope probes across the ends of the wire. An experiment done under tensile stress showed that the Matteucci voltage increases as a result of current annealing under torsion. The influence of an axial DC magnetic field on the Matteucci voltage has been measured with a twist of 51 rad/m and an exciting ac magnetic field of 260 A/m at 30 kHz. Measurements showed that applying a dc magnetic field, inhibits the Matteucci voltage. Furthermore, current annealing under torsion leads to an increase in Matteucci voltage. The author [70] declared that the Matteucci effect needs the existence of a circular component of magnetisation which is achieved by applying torsional stress, so giving rise to an easy axis with the non-vanishing helical component. The magnetoelastic anisotropy induced by torque is described:

$$E_\tau = \frac{3}{2}\mu\xi r\lambda_s \qquad (3\text{-}4)$$

Where λ_s, μ and ξ are the magnetostriction constant, shear modulus and angular displacement per unit length, respectively while r is the distance from the wire axis. The strength of the helical easy axis increases with r coordinate [71] [72]. Annealing will induce circular anisotropy when the heating is below the Curie temperature. It was shown that the largest Matteucci voltage was achieved when the wire was annealed under torsion. Kane et al. [70] suggested that the linear variation of the Matteucci voltage with applied axial stress can be useful for field and stress sensors.

Fe-rich alloys exhibit very low coercive field, magnetic losses and high remanence and susceptibility [73]. The magnetostriction depends not only on the composition of the amorphous wire but also the quality of the metalloid elements [74]. The measured magnetostriction has been shown to depend on the structural relaxation [75], applied stress [76] and fabrication parameters [77]. In these studies, the observed magnetostriction changes were of the order of 10^{-7} i.e. a low magnetostrictive material and small changes in these fabrication parameters can result in changes to the sign of the magnetostriction.

Vázquez et al. [78] analysed changes in the magnetic properties of a Fe-rich amorphous wire $Fe_{77.5}Si_{7.5}B_{15}$ when it is submitted to bending stresses. By decreasing the radius of curvature Rc, the main changes in the magnetic properties are summarised as below: bistable behaviour disappear inside the range 110 mm - 25 mm. This effect is also obtained for short wires less than 7 cm which do not show spontaneous bistability. The appearance of magnetic bistability in Fe-rich bent wires for short enough radius of curvature, allows the design of reduced size pulse generator elements. In such devices, magnetisation reversal within the wire which is caused by existing circular field, is generated by an electrical current passing through the conductor perpendicularly placed across the plane formed by the bent sample. In this way, when a critical current flows through the conductor wire, a sharp voltage pulse is detected in a pickup coil wound around a certain point of the bent sample. Therefore, sharp pulse generator devices and magnetic switches of reduced size can be built by using this configuration.

3.5 Domain imaging on amorphous wires

Co-based amorphous wires have bamboo-like straight domains in the surface while Fe-base amorphous wires have maze type domain patterns [40]. In positive magnetostrictive wire, residual stress will induce anisotropy in which the magnetisation easy axis lies in the radial direction and in negative magnetostrictive wire in the circumferential direction [79]. Therefore, the magnetic properties of amorphous wires depend on the composition and the internal stresses of the material [35].

According to Humphrey et al. [80] two main regions of magnetisation exist in amorphous wires, an axially magnetised inner core and an external shell where

magnetisation is either radial or circular depending on the sign of the magnetostriction which is described in more detail in section 2.6.3. In the intermediate region between the core and the shell as well as the surface of the wire, some closure domain structure exist to reduce the magneto static energy [72]. The origin of such a domain structure must be related to the magneto-elastic anisotropy distribution inside the wire. When the reverse axial magnetic field reaches a critical value, magnetisation inside the core is reversed giving rise to the observed Barkhausen jump. This magnetisation reversal process has been ascribed as a nucleation mechanism [48, 81].

The existence of domains, the arrangement of domain walls, and their reaction to magnetic fields are the consequence of the minimisation of the free energy of the magnetic body and the stray field energy has the maximum contribution [82]. The relative size of stray field and anisotropy energy is very important in domain characterisation and it is defined by the dimension less ratio $Q = \frac{K}{K_d}$ where K is the anisotropy constant which represents crystal anisotropy and $K_d = \frac{J_s^2}{2\mu_0}$ is the stray field energy coefficient which is a measure of the maximum stray field density. In soft magnetic materials this ratio is less than one [82]. However amorphous wires do not have crystal anisotropy.

3.5.1 Kerr microscopy

In the magneto-optical Kerr microscopy method, the polarisation vector of linearly polarised light rotates after reflection from the magnetised surface. The reflected light when passed through a polarising filter can be used to develop a magnetic contrast image [83]. The magneto-optical Kerr effect (MOKE) can be further categorised as the polar, transverse or longitudinal Kerr effects according to the geometrical arrangement of the magnetisation and the plane of an incidence of the scattered light. The Kerr effect results in a rotation of the plane of polarisation of the incident light, or in the case of the transverse effect a change in the intensity of the light reflected from the surface of a magnetised material. Experiments have shown that the rotation of the polarisation or the change of light intensity (depending on the magneto-optical configuration) is approximately proportional to the change in magnetisation [84]. As Figure 3-7 shows, in the polar Kerr effect the magnetisation vector is perpendicular to reflection surface and parallel to the plane of incident, in the longitudinal mode the magnetisation vector is parallel to both

the surface plane and plane of incidence and in the case of the transverse effect the magnetisation vector is perpendicular to plane of incidence and parallel to the reflection surface.

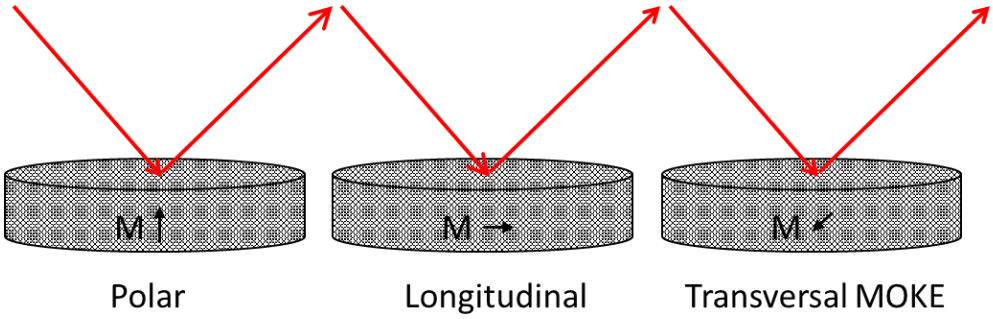

Figure 3-7: Different geometries in Kerr microscopy

Yamasaki et al. have reported on domain imaging of Fe-based and Co-based amorphous wires using Kerr microscopy [79]. As shown in Figure 3-8-a, in Fe-based wire maze-like domains were observed over the entire surface whereas in Co-based wire which is shown in Figure 3-8-b a bamboo-like domain pattern is observed with alternating light and dark areas. These domain patterns do not vary with magnetisation reversal, inferring that both wire types have core domains that contribute to the main magnetisation reversal. Figure 3-9 shows the domain pattern on a polished surface of Fe and Co-based wires. When Fe-based wires are polished deeply a point occurs when the inner core domains become visible and as the polishing proceeds further, the core domains eventually disappear [79]. For Fe-based wire an in-plane magnetisation appears over one-half of the polished surface. Here the effect of polishing is small and the observed domain structure in Figure 3-9-a believed to reflect fairly the internal domain structure.

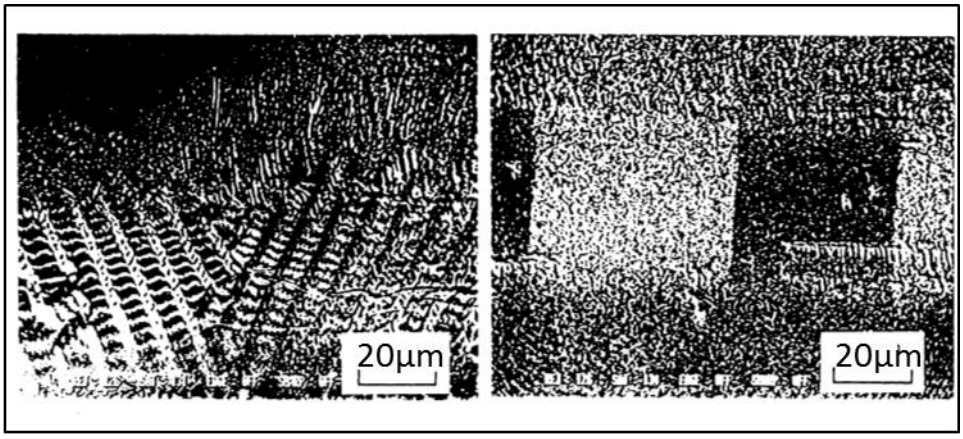

Figure 3-8: a) Domain patterns of Fe-Si-B , b) Co-Si-B amorphous wires observed by Kerr microscopy [79]

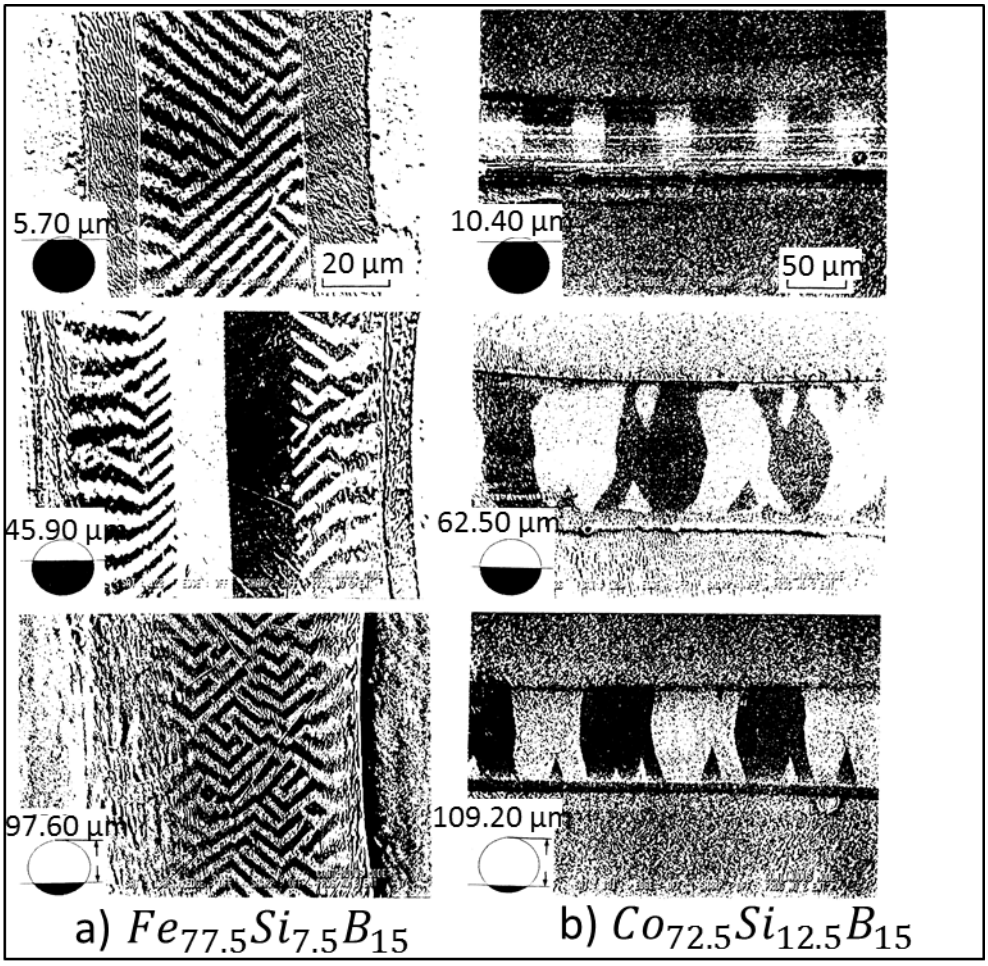

Figure 3-9: Domain patterns of a) zigzag structure Fe-Si-B and b) Co-Si-B triangular structure observed in mechanically polished surfaces by Kerr microscopy [79]

The triangular structure that appeared in Figure 3-9-b in one-half of the polished surface is caused by magnetic poles appearing at the surface as a result of polishing. In Co-based wire no domains corresponding to core domain are observed, Since the magnetisation in Co-based wires are in a circular direction, a perpendicular magnetisation component always appears in a polished surface [79].

Yamasaki et al. demonstrated that Fe-based amorphous wires have separate domain structures consisting of an outer shell and an inner core [85]. The re-entrant reversal takes place in the core domain by domain wall propagation along the wire axis. When domain wall coercivity is smaller than the wall nucleation field re-entrant flux reversal occurs. The wall coercivity of FeSiB amorphous wire is 0.79 A/m and the threshold field (the filed which flux reversal appears) is about 71.79 A/m which is much larger than the wall coercivity. Kerr microscopy performed on 125 μm thick $Fe_{77.5}Si_{7.5}B_{15}$ amorphous wire with 40 mm length is shown in Figure 3-10. The 40 mm long wire is too short to support re-entrant reversal.

The linear increase in magnetisation proceeds by the smooth motion of the wall in the core with the transition region domains remaining unchanged as shown in Figure 3-10-b,c. The cause of the wavy wall in the core domain is not clear. The shell domain seems to catch the white domain in the core when the wall gets closer to the shell domain on the left side, resulting in the small magnetisation jump as shown in Figure 3-10-c,d. The domain pattern of the shell transition region changes on the left side while remaining unchanged on the right.

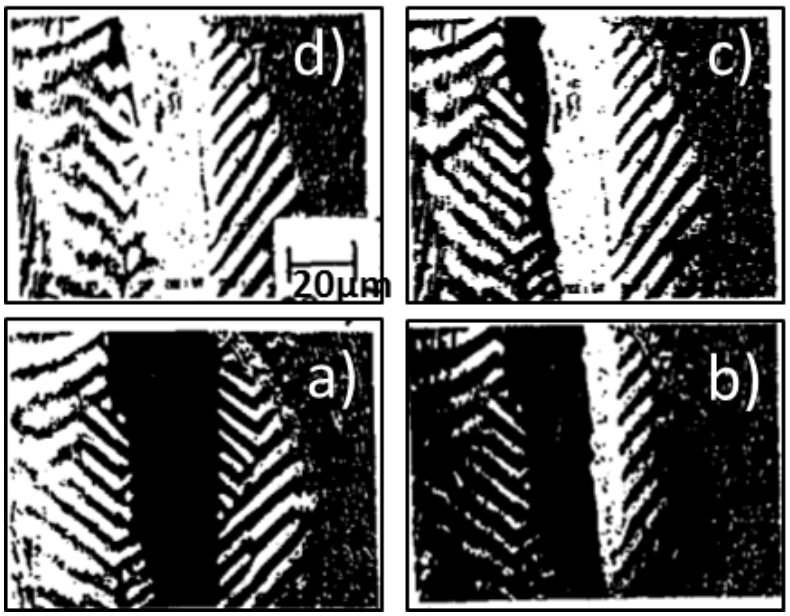

Figure 3-10: Domain patterns in a polished section of 40 mm long wire at different drive conditions [85]

Chizhik et al. investigated surface magnetic domain structures in 120 μm thick, 70 mm long Co-rich $(Co_{94}Fe_6)_{72.5}Si_{12.5}B_{15}$ amorphous wires using Kerr microscopy [86]. The formation and motion of multi-domain structures with curved domain walls have been observed in these wires. Figure 3-11 represents the evolution of the domain pattern during reversal of magnetisation when an axial field was applied to the wire which is perpendicular to the direction of circular surface anisotropy. The change of magneto–optical contrast is shown through Figure 3-11-b to f at the point when full reversal is complete. An equivalent schematic diagram of the surface domain structure is also shown in Figure 3-12 where four distinct domain regions exist prior to complete reversal which is marked from 1 to 4. Domain walls between types 1 and 3 and types 2 and 4 were clearly observed, but the positions of them between the domains of 1-2 and 3-4 were not evident [86].

To conclude, by applying an axial magnetic field, magnetisation reversal appears as a fluent rotation of magnetisation, followed by the formation of a domain structure containing domains of four distinct regions including a curved domain wall boundary. This structure which can move along the wire surface could be considered as a magnetic vortex. The formation of a vortex-type structure in the surface of the wire could be related to some twisting process appearing in the inner core of the wire and to cylindrical-shape anisotropy [86].

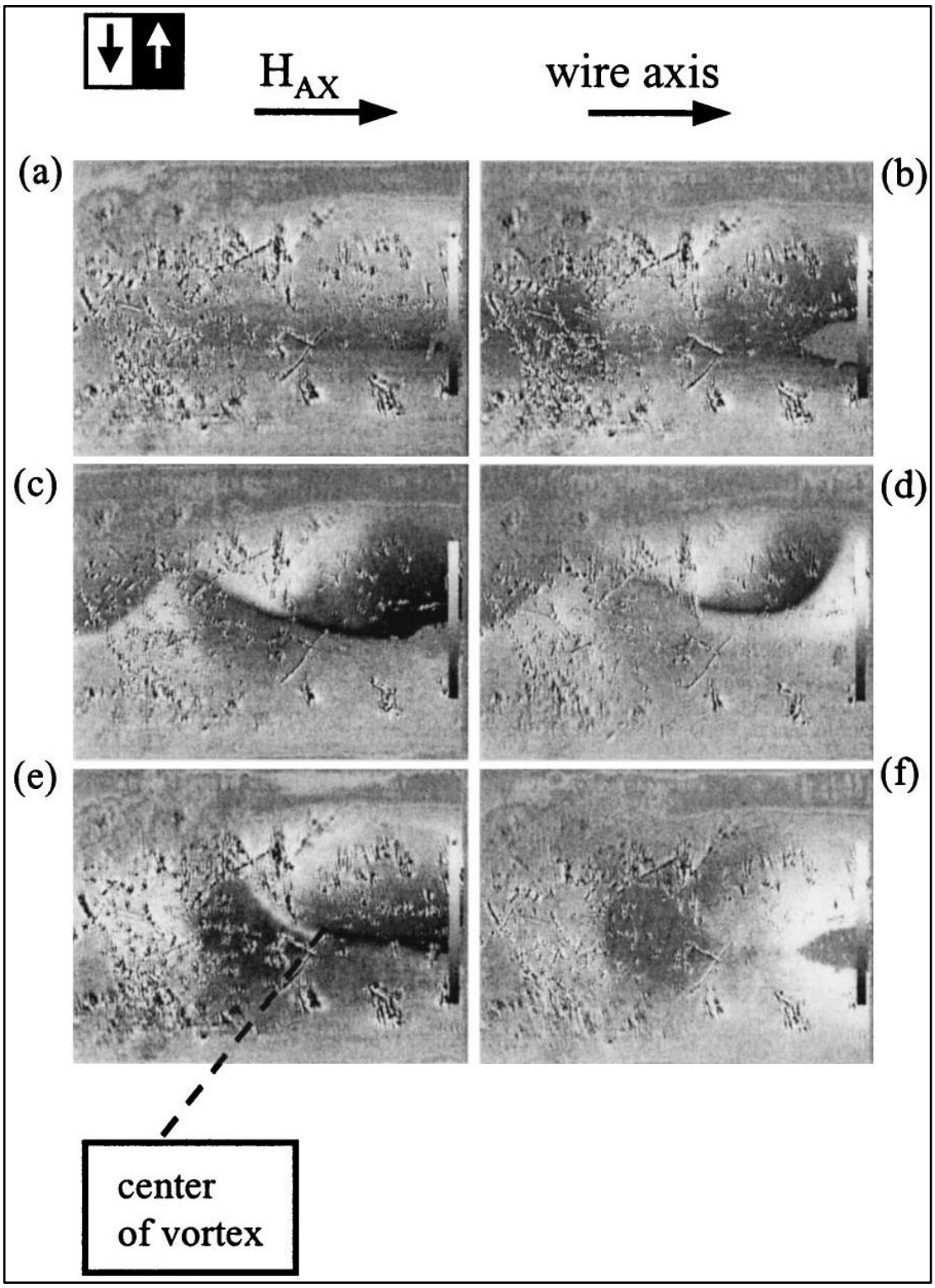

Figure 3-11: Surface domain images of Co-based wires [86].

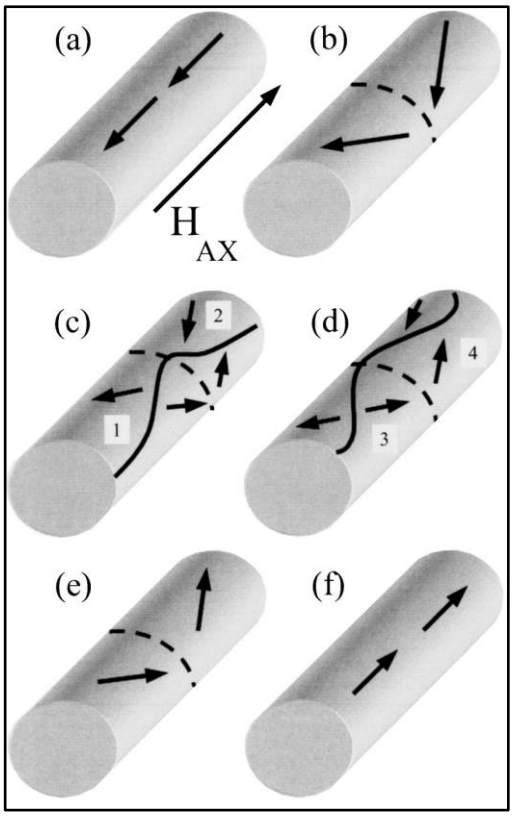

Figure 3-12: Schematic diagram of the evaluation of surface domain structure in the axial magnetic field. Arrows show the direction of magnetisation in surface domain structure [86].

Kabanov et al. [87] investigated a 100 mm long 120 μm thick $Fe_{77.5}Si_{7.5}B_{15}$ amorphous wire with positive magnetostriction and $Co_{72.5}Si_{12.5}B_{15}$ with negative magnetostriction. Figure 3-13-a, shows the distribution of magnetisation in the wire for the so-called stripe with the "open" domain structure. The band domains in Figure 3-13-b were strongly twisted and their shape was similar to Labyrinth-like domain structure in thin films with a bubble domain structure. Figure 3-13-c shows the magneto-optical indicator film (MOIF) image of the same area as Figure 3-13-b [87]. The dark contrast of the transition region between the stripe domains relates to domain walls between them. Figure 3-14-a shows the distribution of the stray field around the edge of an artificial shallow scratch made on the Co-rich wire surface along its axis. Figure 3-14-c is a schematic diagram assuming that the magnetisation at the surface has circular orientation and is formed by 90 ° domains. Such an alignment of the magnetisation in the domains creates a stray magnetic field in the edges of the scratch as shown in Figure 3-14-b.

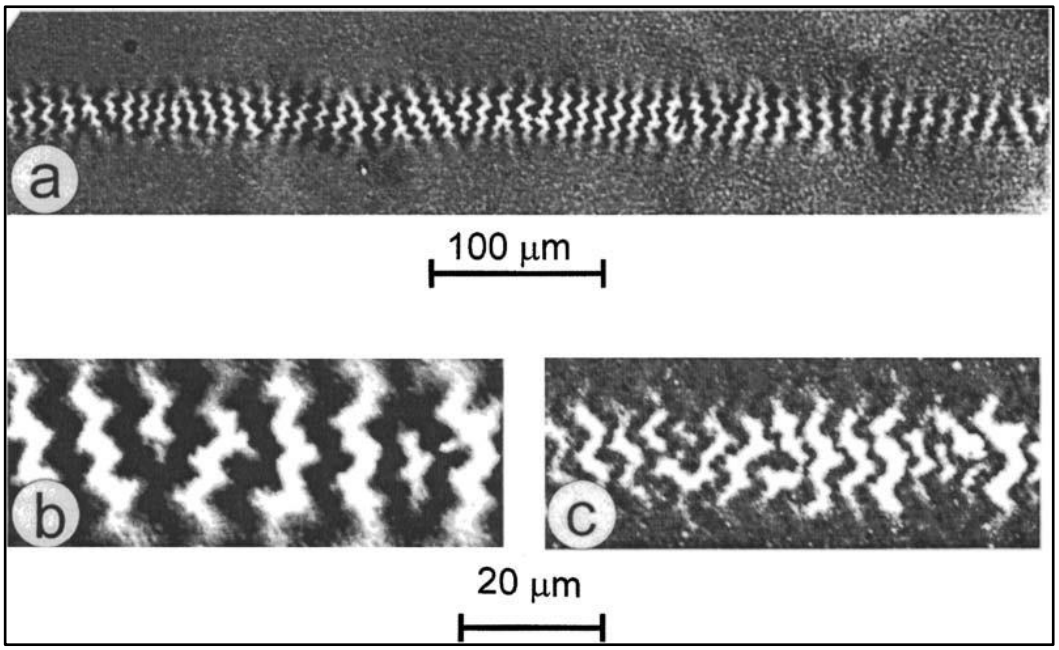

Figure 3-13: Magneto-optical contrast of magnetisation distribution on the surface of Fe- rich wire (a,b) and c) MOIF image of the domain walls in the region as indicated in (b) [87].

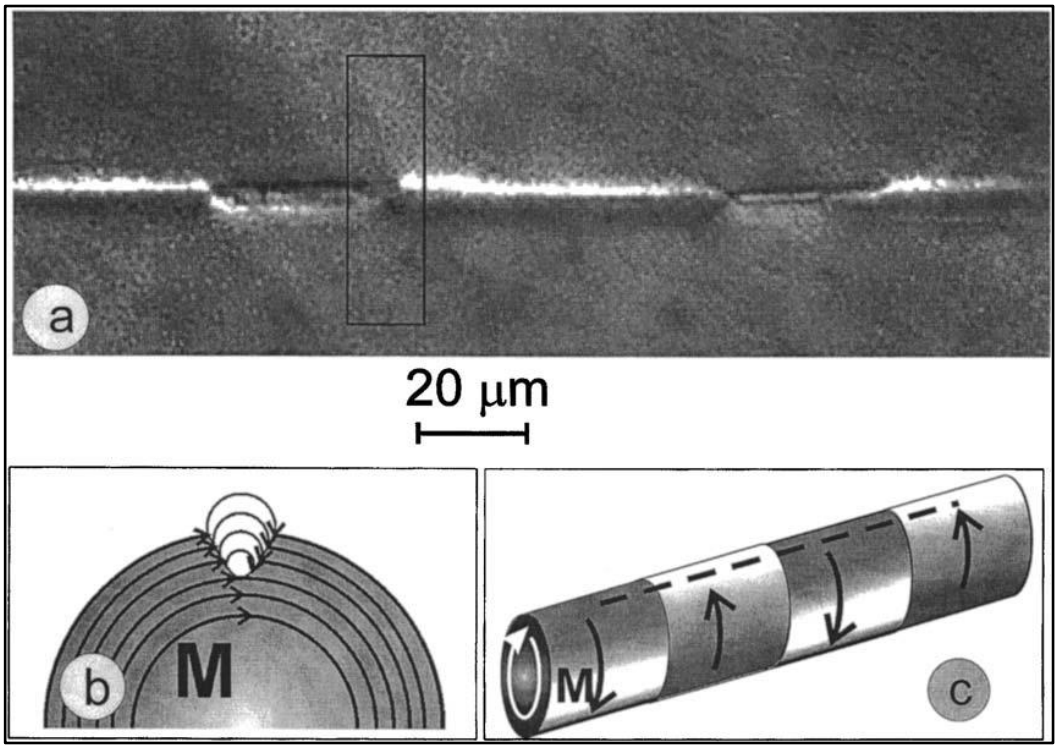

Figure 3-14: a) The MOIF image of magnetisation distribution near artificial shallow scratch made along axis of the C0 – rich wire [87].

3.5.2 Bitter technique

The Bitter pattern technique involves placing a small quantity of ferrofluid on to the surface of a ferromagnetic material. The ferrofluid spreads along magnetic domain walls where magnetic field gradients are highest.

Mohri et al. [48], used the Bitter technique to observe domain images as shown in Figure 3-15 for 125 μm diameter, 80 mm long $Fe_{77.5}Si_{7.5}B_{15}$ amorphous wire. In Figure 3-15-a, Zig-Zag walls indicate the existence of ∏/2 rad walls with the induced anisotropy perpendicular to the wire surface. Moreover, the parallel pattern of these walls with $\pm\ 0.70 - 1.22\ rad$ with respect to the wire axis shows the existence of a random twisting stress direction. The stress direction in "a" is inverse to that in "b". These stresses at the wire surface occur during the solidification of the wire. Figure 3-15-b shows the domain pattern after annealing by passing a 0.4 A current for 2 sec to induce circular magnetic anisotropy. Figure 3-15-c shows the domain pattern after annealing at 370 ºC for 30 minutes. In this case, all domain walls are aligned parallel to the circumference of the wire due to the elimination of random twisting stresses. From these domain images it was concluded that the Large Barkhausen jump and the Matteucci effect of as-prepared wire are dominated by random twisting stresses in the inner core [48].

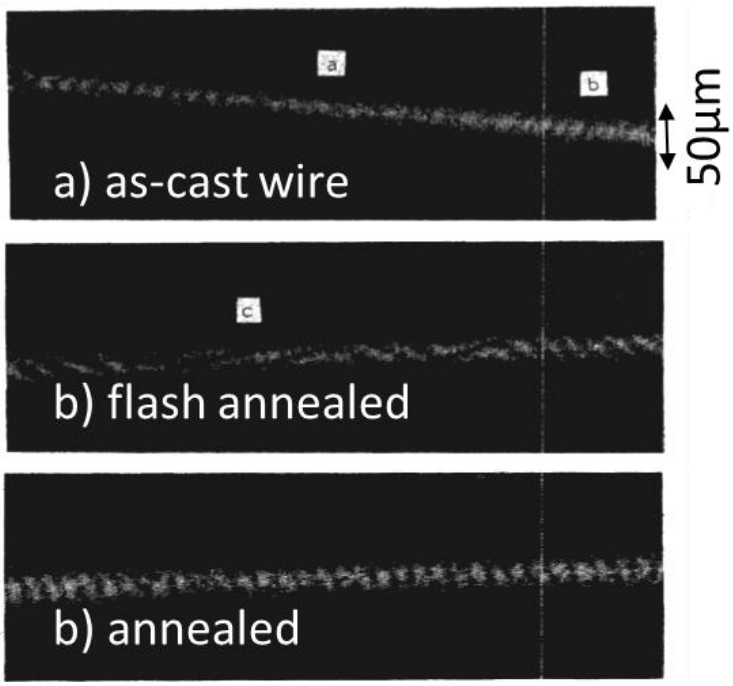

Figure 3-15: Domain observation of $Fe_{77.5}Si_{7.5}B_{15}$ amorphous wire by Bitter technique [48]

Bitter patterns of $Co_{72.5}Si_{12.5}B_{15}$ and $Fe_{77.5}Si_{7.5}B_{15}$ which were observed by Yamasaki [88] are shown in Figure 3-16. As can be seen, Co-based wire has bamboo-like straight walls at the surface while Fe-based wire shows maze-like domain patterns. The domain width is about 20 μm for Co-based wire and 4 μm for Fe-based wire.

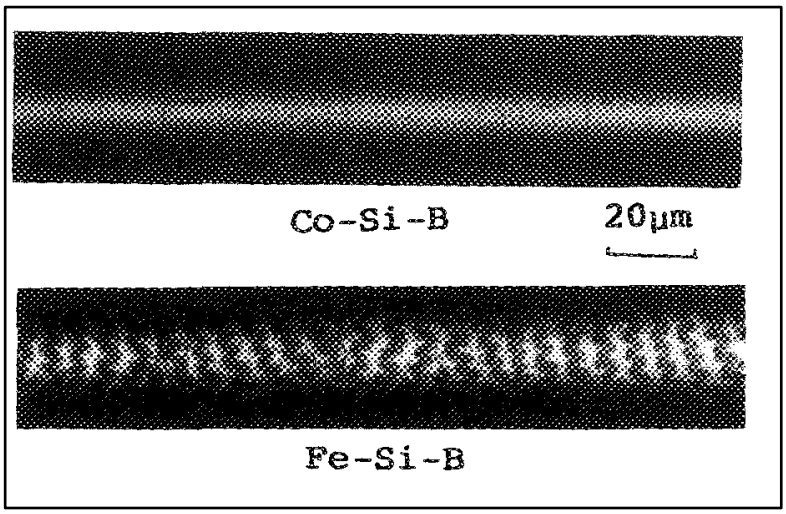

Figure 3-16: Bitter pattern of Co-Si-B and Fe-Si-B amorphous wires by applying 0.8 kA/m magnetic field perpendicular to the surface [88].

Also, Hernando et al. used the Bitter technique [89] to characterise $Fe_{73.5}Si_{13.5}B_9Nb_3Cu_1$ amorphous wire under torsion. A metallographic microscope was used to see the magnetic domains under a constant magnetic field (24 kAm^{-1}) perpendicular to the wire axis to enhance the contrast. The ends of the wire were fixed by clamping and one of the clamps could be rotated to apply pure torsion. An external field up to 6.4 kA/m was provided by a Helmholtz coil. The domain patterns showed a maze configuration and zigzag walls over the whole surface as shown in Figure 3-17. The domain structure changed from a maze configuration with zigzag walls to a helical one by applying torsion. Domain width, as well as tilt angle with respect to the wire axis, changed with torsion. The tilt angle saturated at $\pi/4$ rad/m (radian per meter) for both clockwise and anticlockwise torsions for twisting angles above 2π rad/m.

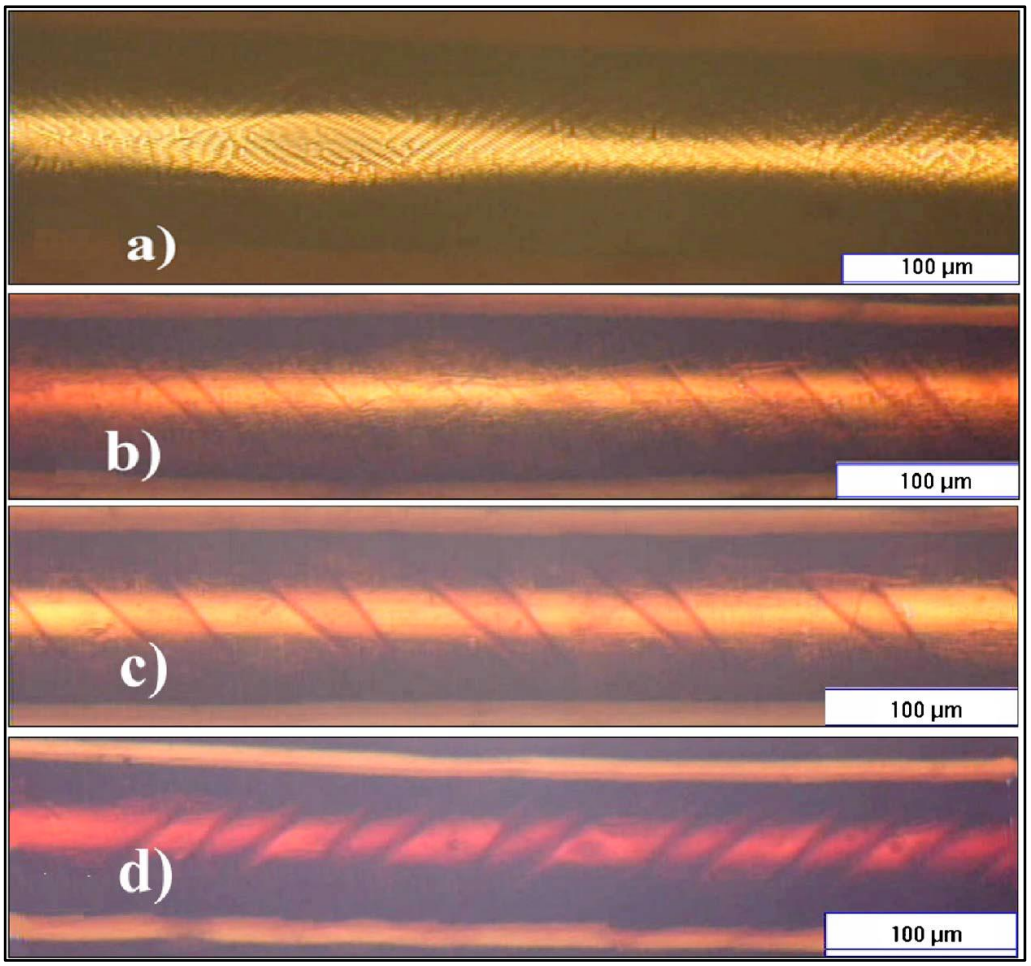

Figure 3-17: Domain structure of $Fe_{73.5}Si_{13.5}B_9Nb_3Cu_1$ a) untwisted and under different values of the applied torsion in the clockwise sense: b) 10 rad/m c) 12.5 rad/m, and in the counter clockwise sense d) -12.5 rad/m [89]

3.6 Annealing amorphous wires

There are different types of annealing such as current annealing, furnace annealing field and stress annealing. Current annealing which is based on Joule heating is commonly used for amorphous wires. When thermal treatment is performed below the sample's Curie temperature, helicoidal anisotropies are easily induced resulting in very interesting magnetic behaviour. Furthermore, if the material is twisted during annealing, induced anisotropies can be achieved [90]. In this paper [90] the relationship between temperatures and current flow through the wire is described as:

$$\Delta T_{max} = T(0) - T(a) = \frac{j^2 \rho}{4k} a^2 \quad (3\text{-}5)$$

Where a is the wire radius, k is thermal conductivity, T_0 is the room temperature, j is the current density (j=I/S), I is the electrical current and S is the cross-sectional area of the wire. By considering an annealing current of 0.36 A, $a=6.2*10^{-5}$, $\rho=1.3*10^{-6}$ Ωm and k=10 $Wm^{-1}K^{-1/4}$, ΔT_{max}=0.11 K, which suggests that under particular boundary conditions, the radial steady state temperature profile is homogeneous far from the ends of the wire. This theory can be used in the case of amorphous wires showing that the z temperature profile turns out to be extremely flat over more than 90 % of the wire length.

Chiriac et al. stated [91] that current annealing amorphous wires would improve their magnetic properties. They [91] proposed a model to calculate the relation between the DC current and temperature by taking into account the linear temperature dependence of the electrical resistivity. The higher the value of DC current, the faster the equilibrium temperature is reached. The temperature distribution was approximately constant in the cross-section of the wire. The calculated values of temperature for different values of current were very close to those found by magnetic measurements of the Curie temperatures.

Gonzalez et al. [92] annealed 125 μm thick, 100 mm long $Fe_{77.5}Si_{7.5}B_{15}$ amorphous wires by passing 400, 425 and 550 mA current through it. The annealing time was chosen by considering the necessary time to reach a stable value of reduced remanence with different intensities of electric current. It was concluded that current annealing increases the relaxation of internal stresses produced from quenching, resulting in increased remanence and reduced coercive field prior to applying tensile stress. Consequently, after annealing the internal stresses were reduced [92]. Results show that the switching field H* by applying tensile stress decreases after certain stress that the remanence reaches its saturation value and the pinning centers at the surface, make the wire magnetically harder and hence an increase of H* is observed. The annealed sample show similar result to as-quenched one but the applied stress for achieving the minimum value of H^* decreases as the value of annealing current increases. For higher stress, H^* increases in a similar way to the as-quenched wire [92]. Moreover, remanence ($m_r=M_r/M_s$) increases with stress then saturates. The stress in which this saturation occurs is 300 MPa for as-quenched wire while it decreases for increasing annealing current.

The coercive field depends on the applied stress in either as-quenched or annealed samples in a manner similar to H^*. Overall, this paper [92] discussed the influence of applied stress on the magnetic properties of the hysteresis loop on as-quenched and annealed positive magnetostrictive wire.

3.7 B-H curve

Some amorphous wires show bi-stable magnetic behaviour due to their unique domain structure. Fe–based amorphous wires, in contrast to amorphous ribbons, have bi-stable hysteresis loops, a consequence of its large Barkhausen jump [40]. Bi-stable simply means two stable states. In the case of AF10, both stable states are along the wire but in opposite's directions. Reversing the magnetisation flips from one state to the other via the large Barkhausen jump. Yamasaki et al. [88] measured the B-H curve for $Co_{72.5}Si_{12.5}B_{15}$, $Fe_{77.5}Si_{7.5}B_{15}$ and $(Fe_6Co_{94})_{72.5}Si_{12.5}B_{15}$ for a 60 Hz sinusoidal field parallel to the wire's length. The B-H curve for Co-based wire as it is shown in Figure 3-18, exhibits properties similar to Fe-based wire. The wire exhibits no irreversible flux change when the amplitude of the drive field is below a certain threshold. Large Barkhausen discontinuities (LBD) take place when the applied field is equal or higher than the critical domain nucleation field H_n. The value of H_n and the fraction of magnetisation participating in LBD of Co-based wire are smaller than Fe-based wire. In contrast, $(Fe_6Co_{94})_{72.5}Si_{12.5}B_{15}$ shows very soft magnetic properties without LBD.

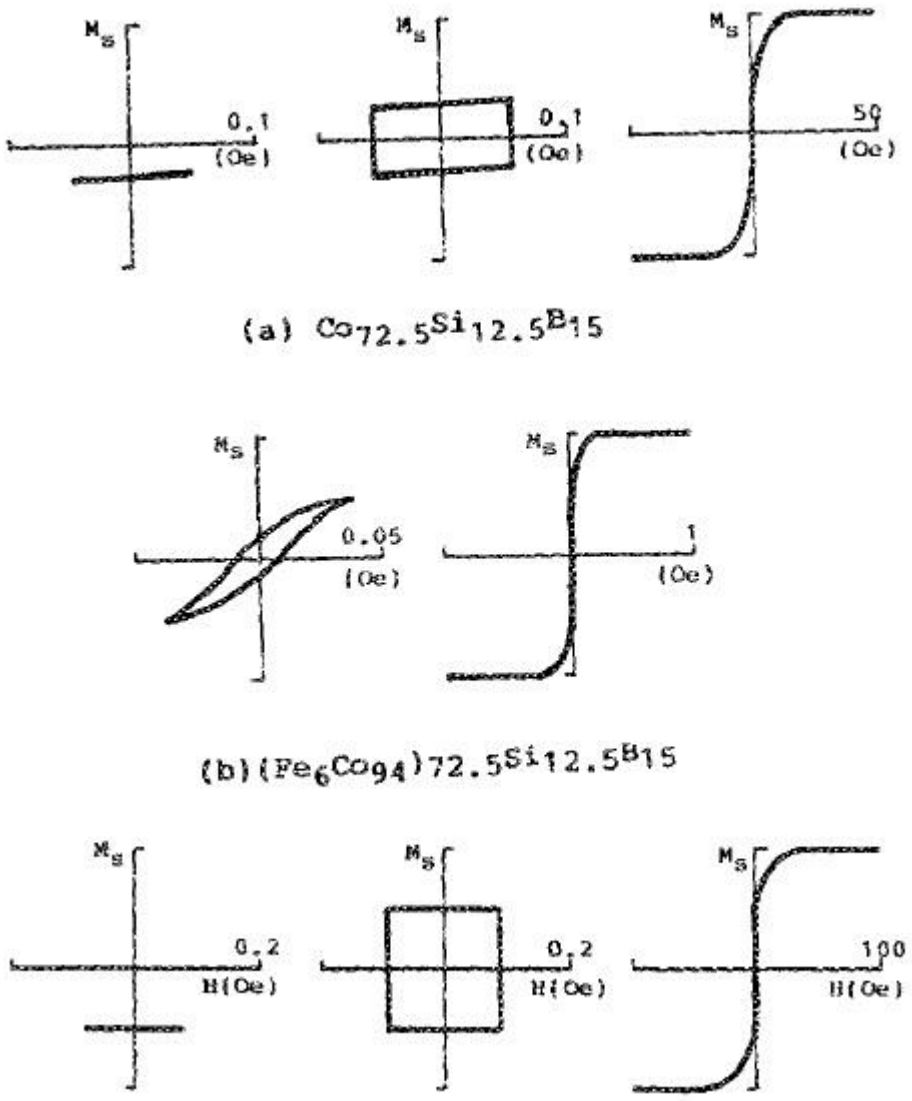

Figure 3-18: B-H loops of as-quenched (a) Co-Si-B, (b) (Fe,Co)-Si-B, and (c) Fe-Si-B amorphous wires measured at 60 Hz [88].

Fe-based $Fe_{77.5}Si_{7.5}B_{15}$ amorphous wire has square-shaped B-H curve related to large Barkhausen jump as shown by Gawronski et al. [93]. Usually Co-rich microwires exhibit inclined hysteresis loop with low coercivity of 4-5 A/m but the magnetic permeability is not high because of the relatively high magnetic anisotropy field. Generally, the best soft magnetic properties are observed for nearly-zero magnetostrictive compositions [36, 94].

The dependence of hysteresis loop on these parameters has been attributed to the magneto elastic energy given by:

$$K_{me} \approx {}^{3}/_{2}\,\lambda_s \sigma_i \quad (3\text{-}6)$$

Where λ_s is saturation magnetostriction and σ_i is the internal stress.

3.8 Strain sensors

Strain sensors are normally used to detect physical deformation and mechanical loading such as stress and strain on the structure. Currently, strain sensors are used in various fields ranging from civil engineering to medical applications [95], [96]. In medical applications, strain sensors are used to monitor physiological parameters such as lung ventilation [97], joint and bone movement [95] and human body motion [98]. Continuous real-time monitoring of these parameters allows a better evaluation of patient's health by physicians [99]. For instance, Gattiker et al. [95] developed a wireless and passive implantable sensor based on ultrasound detection for real-time monitoring of small strains on implants, bones and joints. Another real-time strain sensor is the magnetostrictive amorphous sensor developed by Klinger and co-workers [97] to measure strain by detecting change in the magnetic permeability caused by mechanical loading. The most common and established sensor is resistive and capacitive strain gauges. The capacitive sensor is based on a change of the separation distance between two parallel conductor plates which alter the capacitance of the sensor. Although they are simple and sensitive, they are electronic components that need direct wire interface [100]. Tan et al. presented [100] a passive strain sensor based on the harmonic shift of a magnetically soft material. Also, a passive stress sensor based on magnetic material is presented in [101] and [102]. The resonant frequency of the vibrating magneto elastic ribbon changed with varying applied stress, allowing remote detection of mechanical deformation and loadings. However, this sensor was just applicable to low stress situations since high stress severely dampens the vibration leading to significant weakening of the sensor signal. Kusumoto et al. [103] developed, a fingertip blood vessel pulsation (FTP) sensor with a capillary blood vessel pressure by using CoSiB amorphous wire stress impedance which showed a giant magneto impedance of about 4000. The FTP was placed between the elbow and wrist and measured blood vessel pulsation speed V_{ew}. Measurements between the wrist and fingertip V_{wf} showed V_{ew} was faster than V_{wf}. Mohri et al. [104] developed sensitive, quick response and low power consumption micro magnetic sensors utilising magneto- impedance (MI) and stress- impedance (SI) effects in zero

magnetostrictive and negative magnetostrictive amorphous wires of 30 μm diameter and 2 mm length connected with CMOS MI sensors circuits. The SI sensor using a 20 μm diameter negative-λ amorphous wire showed an equivalent gauge factor of about 4000 for stress (Strain) sensors and a resolution of 0.1 cms^{-2} for acceleration sensors.

3.8.1 Stretchable strain gauges

Strain gauges are stretchable sensors which produce a changing electrical signal in response to applied stress. There are different types of materials and technologies listed in Table 3-2 for strain sensor applications.

Table 3-2: Strain sensor applications on different materials

Material	Method to measure strain
Metallic films [105-107]	Piezoresistive effect
Carbon blacks [12, 108, 109]	Piezoresistive effect or dimension changes
Carbon nanotubes (CNTs) [110-112]	Depended on both the separation of the wrinkled structure and the changes in the wrinkle's geometry to respond the strain below 400%
Graphene [112-115]	Change of resistance due to strain
Silver nanoparticles (AgNPs) [116, 117]	Exploiting the mechanisms including the micro-crack propagation in thin films and the disconnection between sensing elements
Conductive ionic liquids [112, 118, 119]	Change in dimension of ionic liquids
Graphite [120, 121]	Change in contact resistance
Platinum nanobelts [122]	Change of resistance due to strain
Carbon-coated fibre [123] [124]	Measuring their resistance changes under variable loading

a) Metallic strain sensors

   Conventional metal-foil strain sensors consist of a fine wire or metallic film arranged on a flexible substrate in a grid pattern. Despite their simple structure they have low sensitivity (Gauge factor (GF)~ 2) and have small strains (maximum strain of 5 %). This makes them unsuitable for measuring strains associated with human motion [115], [125],[126]. A class of stretchable strain sensors fabricated by thermally evaporating gold film patterns on to silicon substrate or micro plotting liquid metal as conductive wires [105] or tubes [106] has increased the strain by up to 50 % but still suffer from a small GF less than 5.

b) Fabric-based strain sensors

Fabric based deformation sensors can be produced by coating a thin layer of piezoresistive material on conventional fabrics. Fabric-based strain sensors have high wear ability, but slippage of the conductive material on textile fabrics usually deteriorates the measurement accuracy. Moreover, it is difficult to establish a reliable relationship between the applied strain and the kinematic parameters such as bending angles, since the textile sensors have large contact area and human skin tends to be uneven. [127]

c) Nanomaterial- based strain sensors

Among the available nanomaterial-based sensors, CNT-based sensors have demonstrated strong stretchability with maximum strains of 280 % (single-walled CNTs) [128], 400 % (super- aligned CNT films) [129], 450 % (vertically aligned CNT forest), 510 % (multi-walled CNTs), 750 % (wrinkled CNTs) [130] and 960 % (CNT fibres). However, they have the limitation of GF<1. A wearable strain sensor fabricated by depositing nano/micro sized wrinkled CNTs on to an Eco flex substrate has been developed. The wrinkled structure increased the sensor's strain to 750 %, but the GF was small at 0.65 for strains below 400 %.

d) Graphene fibres

Sensors based on Graphene fibres with compression spring architectures exhibited an ultrahigh sensitivity to the detection limit of 0.2 % strain and ability to measure multiple forms of deformations, including strain, bending and torsion [131]. Although they have a wide sensing range (up to 200 % strain) and excellent durability, they still suffer from some limitations in their applications

including the complicated fabrication processes and the non-transparency of the sensor that might affect the appearance of wearable devices [129].

3.9 Bending sensors

Bend sensors, also known as flex/flexion/flection sensors, angular displacement sensors, or flexible potentiometers, directly measure the amount of bend typically as a function of electrical resistance [132]. They are generally fabricated by coating or printing carbon/polymer ink-based materials onto flexible plastic substrates such as polyimide and polyester. When the sensor bends, micro-cracks are introduced into the coated film causing the change in resistance.

The earliest motion control for home entertainment was developed especially for use in the "Power Glove" in 1989 by Abrams [133]. A year later its production ceased due to its imprecision and difficulty of operation [134]. Following this, several manufacturers such as Image science Instruments, Inc.(Images SI) [135] Spectra Symbol, Crop. [136], and flexible point sensor system, Inc.(Flexpoint SS) [137] released their owned flexible bend sensors.

As shown in Figure 3-19-a, Images SI [138] manufactures bi-directional bend sensors with a length of 114.3 mm, which consists of a strip of resistive material sandwiched between two copper foil laminates. According to the manufacturer's specification, the sensor has a nominal resistance of 10 kΩ which decreases gradually by bending in either direction [138]. However, Orengo in [139] developed a piezoresistive bend sensor by Images SI which showed linear increases of resistance from 4 kΩ to 16 kΩ for bending angles ranging from -∏/6 to ∏ rad. Although these bend sensors are used in glove sensing systems [140-142], they have been discontinued since 2010 because of their low accuracy and stability. The off-the-shelf bend sensors manufactured by Spectra Symbol are usually designed with lengths of 55.9 mm or 112 mm, as shown in Figure 3-19-b [143]. They exhibit a linear dependence with bending angle. However, a hysteresis error of 14 % was reported for the 112.2 mm sensor during bending-unbending operation from 0 to ∏/2 rad, much higher than that of bend sensors from Flexpoint SS(about 3 %) [144]. Simone et al. [145] achieved a 112.2 mm sensor over a 7.62 cm diameter tube, 31.8 % decay of initial resistance over time after bending for 30 seconds which is almost three times that of Flexpoint SS. (8.9 %). Moreover, in [144] sensor resistance varied from 8.2 kΩ to 13.1 kΩ when

the sensor was bent from 0 to ∏/2 rad. In contrast, the sensor with Flexpoint SS produced resistance variation of 112 kΩ for the same bending range. It can be concluded that the Flexpoint SS sensors are more stable and sensitive to mechanical deformation than the Spectra Symbol bend sensors.

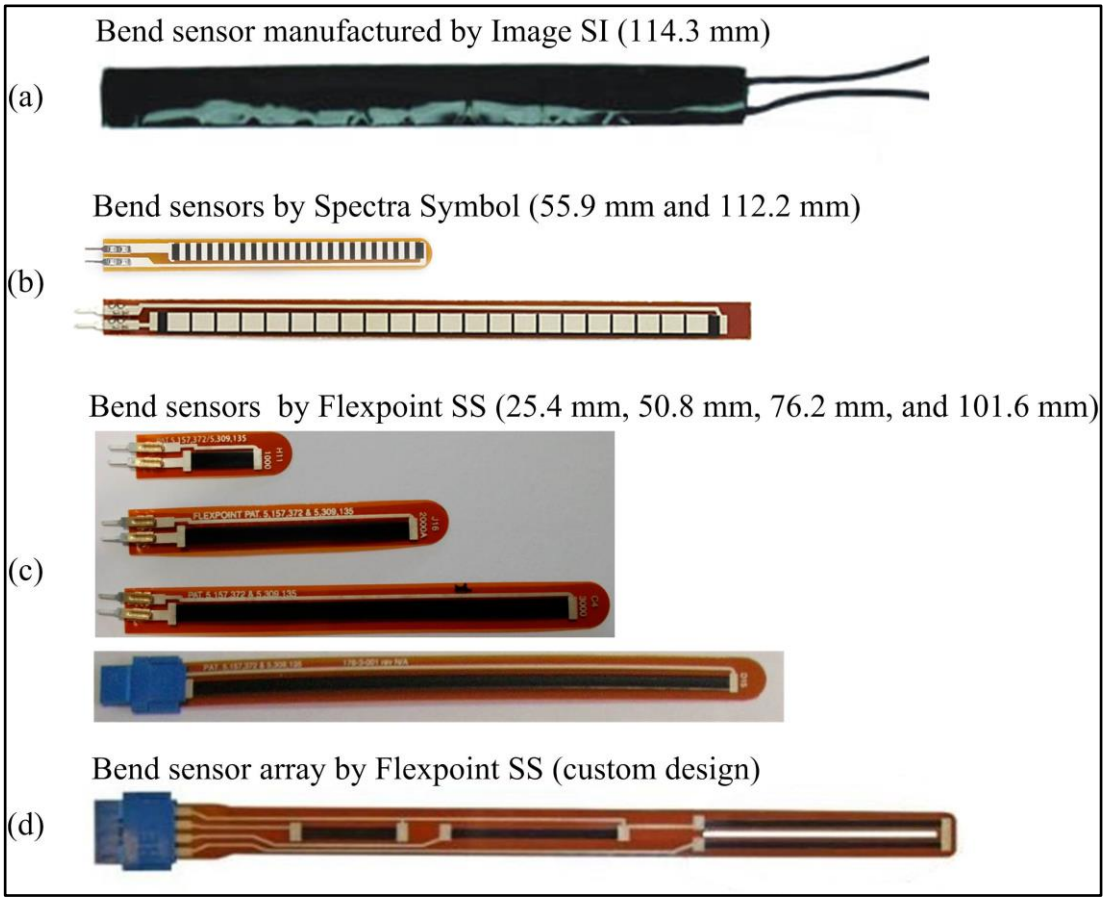

Figure 3-19: Images of commercial bend sensors a) Bi-directional bend sensors manufactured by Images SI [138] b) Bend sensors produced by Spectra Symbol [143] c) Bend sensors with different lengths manufactured by Flexpoint SS [144] d) custom design, bend sensor array produced by Flexpoint SS [146].

Borghetti et al. [144] reported that the resistance of polyimide, polyester and bare bend sensors varied by about 2 %,3 % and 30 % respectively after bending at ∏/2 rad for 180 s. Therefore, the sensors over-coated with polyester or polyimide are generally considered to be more stable than bare bend sensors.

Thin-film bend sensors produced by Flex point SS, are one of the most popular sensors used in applications for tracking finger motion [5, 147-149]. Jurgens et al. [150] have developed a low-cost sensor by screen printing carbon-based electrically conductive ink onto the polyester substrate. The sensor repeatability was 6.5 % with a 100 Ω variation in resistance when bending from 0 to ∏/2 rad.

Melzer et al. [151] designed a new sensor based on the Hall effect. Inorganic functional nanomembranes with polymeric foils were combined to achieve a flexible sensor with sensitivity of -2.3 V $(AT)^{-1}$. The sensor was fabricated on 100 µm thick polyimide foils that withstand mechanical deformations. Only a minor reduction was observed in sensor performance after bending to a radius of 6 mm and returning to the flat state. As shown in Figure 3-20-a,b,c adhering the flexible sensor to a finger creates a wearable sensor. By monitoring the output, the relative position of the finger with respect to a permanent magnet was obtained as shown in Figure 3-20-d and e. For demonstration purposes, eight bismuth Hall sensors were exposed to the field of a permanent magnet Figure 3-20-f,g. A maximum signal was achieved when the magnet was placed above the sensor as shown in Figure 3-20-h. In order to investigate the bending performance, flexible sensor elements were mounted on to sample holders with concave curvatures from 6 to 32 mm. From geometric considerations, these curvatures correspond to strain values in bismuth film of 0.24 % and 1.25 %, respectively. The sensitivity of the unbent sensor was –(0.54±0.01)V $(AT)^{-1}$ which is the highest value for as-prepared sensing elements on the polyimide foils (200 nm thick Bi film). The sensor was positioned in the planar, bent and then again planar arrangement for each radius of curvature measurement. In the flat state, the sensor response remained at the initial sensitivity even after bending into a radius of 6 mm [151].

To conclude, flexible bismuth Hall sensors on polymeric PEEK and polyimide foils were fabricated. The sensor can be bent around the wrist or positioned on the finger to realize the finger position with respect to the magnetic field. The optimised sensor sensitivity was -2.3 V $(AT)^{-1}$ [151].

Alaferdov *et al*. [120] developed a simple and scalable method for fabrication of wearable strain and bending sensors based on high aspect ratio graphite nanobelts, thin films deposited by a modified Langmuir-Blodgett technique on to flexible polymer substrates. The sensing mechanism is based on the changes in contact resistance between individual nanobelts upon substrate deformation. Very high sensor response stability for more than 5000 strain release cycles and a device power consumption as low as 1 nW was achieved. The maximum strain that could be applied to the system was 40 %. Bending tests were carried out for various radius of curvature.

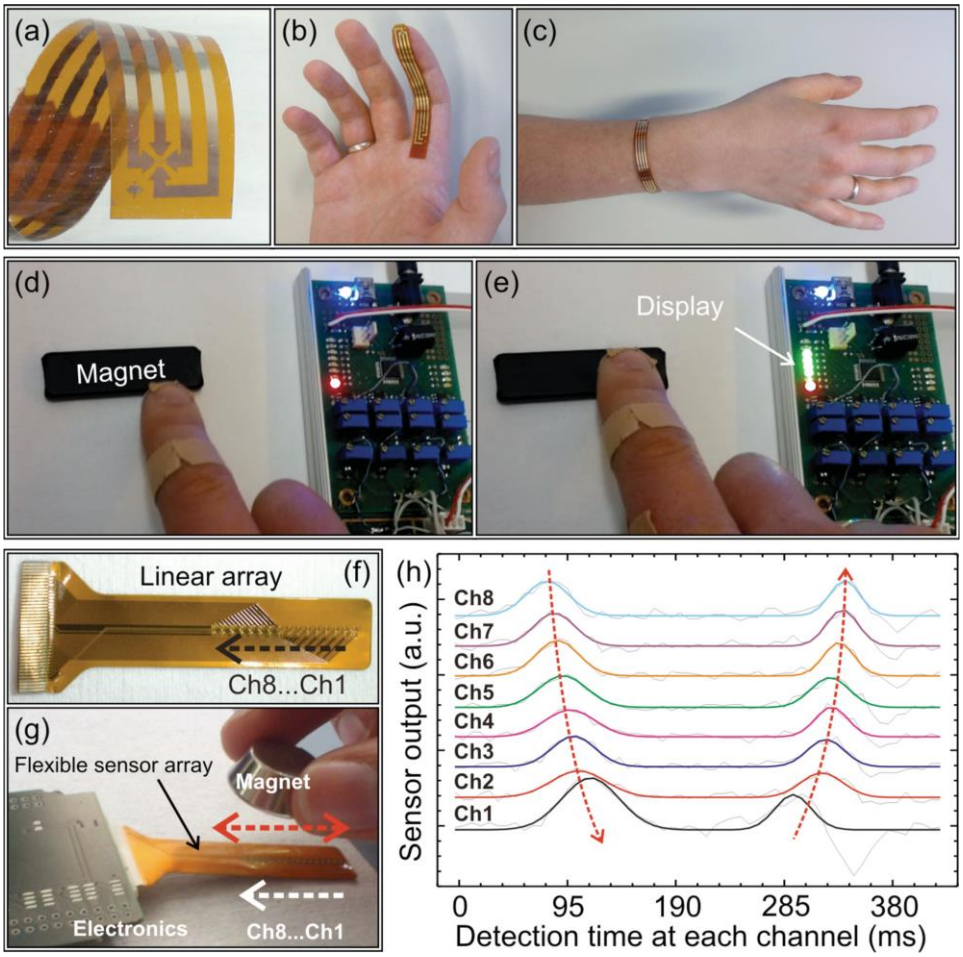

Figure 3-20: The different position of sensor on the finger or on the wrist of a hand [151]

The common limitations and strength of these sensors are listed below:

Strength: they are highly flexible, easy to operate and low cost.

Limitations: time-consuming calibration process, large hysteresis errors and failure to return to the initial state after loading, slow to respond, temporal drift and suffering from significant overshoot in high-speed situations.

Klinger et al. [97] designed a new sensor, simple, inexpensive to manufacture and with adjustable sensitivity for the monitoring articular movements and lung ventilation. This sensor is based on the change of permeability due to mechanical stress and strain. If an amorphous ribbon is glued on to a plastic ribbon with considerably higher thickness, bending this sensor will cause mainly tensile or compression stress in amorphous magnetostrictive material dependent upon the direction of bending. Figure 3-21 shows the amorphous ribbon AR (length l, thickness d_a , width b_a and Young's modulus E_a) attached to a plastic ribbon PR (l, d_p, b_p, E_p) which shows lower Young's modulus but considerably higher thickness.

As a result of bending the composite sensor Figure 3-21a, the tensile stress in the ribbon will dominant for state II and a compressive stress dominates in state III. Consequently, considering the theory of pure bending of beams and taking into account additional simplifications (such as plain cross-sections, negligible thickness of adhesive layer, validity of Hooke's law) the mean strain of the amorphous ribbon is given by [97]:

$$\varepsilon = \frac{1}{l}\frac{d_a}{2} r_d r_b r_E \frac{1 + r_d}{1 + r_d r_b r_E} \tag{3-7}$$

With l equal to the bending radius and $r_d = \frac{d_p}{d_a}$, $r_b = \frac{b_p}{b_a}$, $r_E = \frac{E_p}{E_a}$, the ratios of thickness, widths and Young's moduli for AR and PR layers. Gluing AR on PR, which was pre-bent to the radius of l_0, yielded an effective sensor for elongation x in the connecting line of two sandwiches ends.

For the ratio of bending stiffness $r_d^3 r_b r_E \ll 1$, gluing will not yield considerable change of l_0 and effective overall elongation x will cause a bending radius according to:

$$l \sin(\frac{l}{2l}) = \frac{x}{2} + l_0 \sin(\frac{l}{2l}) \tag{3-8}$$

Thus, roughly the amorphous ribbon will show pure compressive stress according to differentiate stress and strain.

$$\varepsilon = \left(\frac{1}{l} - \frac{1}{l_0}\right)\frac{d_a}{2} r_d r_b r_E \frac{1 + r_d}{1 + r_d r_b r_E} \tag{3-9}$$

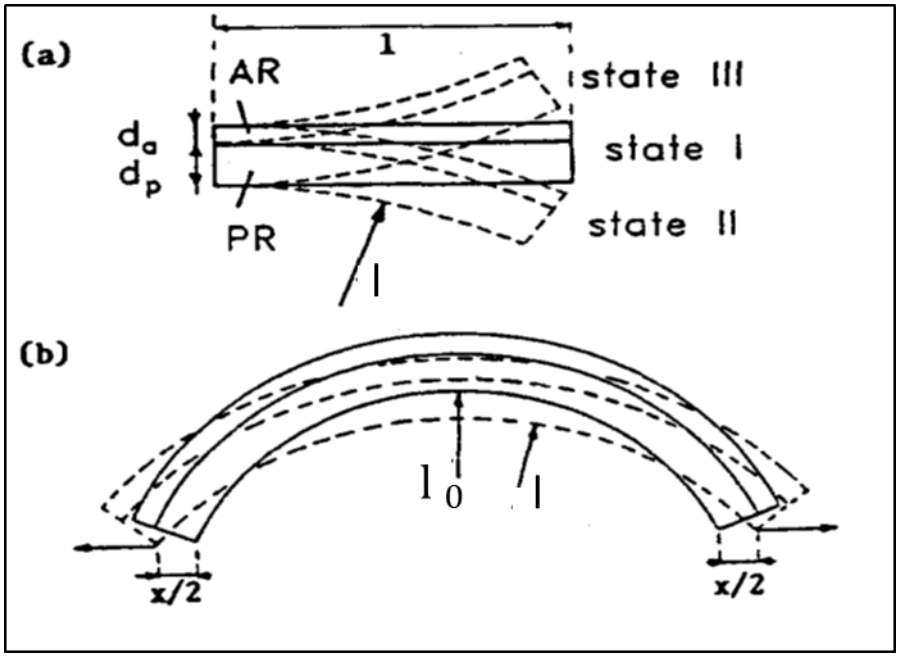

Figure 3-21: a) Compound sensor type in various states of stress b) pre-bent sensor in initial and elongated states

A literature survey regarding the Matteucci effect on amorphous wires, characterising amorphous wires and their application in addition to domain imaging on amorphous wires, annealing and B-H curves were discussed in this chapter. Moreover, different technologies in producing strain and the bending sensors were reviewed. The performance of each type of sensor were briefly presented and their advantages and disadvantages were summarised.

4 The magnetic characterisation and measurement of the Matteucci effect in amorphous wires

4.1 Introduction

The Matteucci effect is the presence of voltage pulses detected at the ends of an amorphous wire when magnetised axially with an alternating field. The amplitude of the voltage pulses changes by application of torsional and axial stresses. The origin of the effect is helical anisotropy brought about by the interaction of the magnetostriction and induced stresses. However, the effect is also significant in near-zero magnetostrictive alloys so the mechanism involved cannot be simply explained in terms of magnetostriction.

Much of the reported characterisation on amorphous wires has been done on long wires ranging in lengths from 10 cm [10] , 12 cm, 13 cm [10, 32], 20 cm [52] , 30 cm [49, 56] to 55 cm [38]. For sensing applications, there has been a lack of investigations into the Matteucci effect for short wires. Amorphous alloys are suitable candidates for small sized magnetic sensors with high stress and magnetic field sensitivities. Typically, they have high maximum tensile strengths (σ_{max}: 2450-3920 MPa), uniform microstructures due to the absence of grain boundaries and high resistivities (ρ: $120 - 190\ \mu\Omega$ /cm). They are also thin with thicknesses of 20-40 μm for ribbons and 50 to 200 μm diameter for wires. Their magnetic properties include high permeability and a small induced anisotropy constant (K_u: 200- 800 J/m^3) [59]. Amorphous wires were chosen for investigation in this thesis because of their exceptional Matteucci voltages and magnetoelastic properties making them potential candidates for strain sensing applications. This chapter describes the experiments conducted to characterise amorphous wires under different conditions of torsion, tensile stress and magnetic field strengths and frequencies in order to optimise properties for sensor applications. Domain imaging and B-H curve characterisation has also been done to provide useful insights into the magnetic anisotropy of the material.

4.2 Amorphous wires which are investigated

The samples used in this thesis are listed in Table 4-1.

Table 4-1: Specification of amorphous wires

Samples	Composition	Diameter (μm)	magnetostrction	Length (mm)	Annealed
AF10	$Fe_{77.5}Si_{7.5}B_{15}$	125	34.5×10^{-6}	114,45,20	1 min by passing 0.5 A current
AC20	$(Co_{94}Fe_6)_{72.5}Si_{7.5}B_{15}$	125	-0.08×10^{-6}	114,45,20	-

As it can be seen in Table 4-1, the amorphous wires investigated in this work were supplied by Unitika Ltd and included $Fe_{77.5}Si_{7.5}B_{15}$ (AF10) and $(Co_{94}Fe_6)_{72.5}Si_{7.5}B_{15}$ (AC20), both 125 μm in diameter with magnetostrictions of 34.5×10^{-6} and -0.08×10^{-6} respectively [36]. AF10 amorphous wire was annealed by passing 0.5 A current for 1 min.

4.3 The measurement system for measuring Matteucci voltage in amorphous wire

To be able to measure the Matteucci voltage in amorphous wires, a system capable of applying both tensile and torsional stresses were needed. To achieve this, the measurement system shown in Figure 4-1 was designed and built. This system used a solenoid to excite the wire with a sinusoidal magnetic field of peak amplitude 1.49 kA/m. The solenoid was powered by a function generator (Key sight Infinivision DS0-X3012T) connected to a power amplifier (Pioneer M-73 stereo power amplifier). A later version of the system substituted the power amplifier with a Keysight BP2961A power source. The magnetising coil frequency varied from 100 Hz to 10 kHz at a peak sinusoidal magnetic field of 1.49 kA/m. A LCMFL-20N load cell, with a nominal capacity of 20 N, was used to measure the tensile stress applied to the wire. Movement of the translation stage (with a resolution of 10 μm), attached to one end of the fixed wire, enabled fine control of the axial stress from 0 to 326 MPa. Torsional stress was applied at intervals of 0.17 rad by a rotation mount with

a precision of 0.002 rad (one arc per minute) from 0 to 2∏ rad. Right angle brackets and post holders at both ends, were mounted on to an aluminium breadboard to support the amorphous wire under test. Experiments were performed on amorphous wires using lengths of 114 mm for basic characterisation and 20 mm and 45 mm for determination of sensor performance.

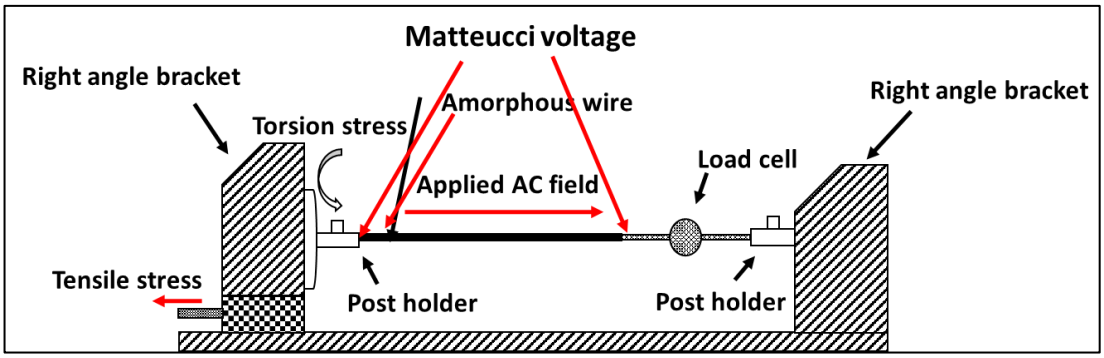

Figure 4-1: The mechanical arrangement used for measuring Matteucci pulses.

All components used in the construction of the system were nonmagnetic and epoxy resin was used to fix the amorphous wires inside the post holders. To measure the Matteucci voltage, the ends of the amorphous wire were connected to thin copper wire using copper sleeves with relative permeability of 0.9. The other ends of the copper wire were connected to an oscilloscope. This method was chosen as it provides a minimal stress connection and avoids soldering which could risk crystallisation of the sample.

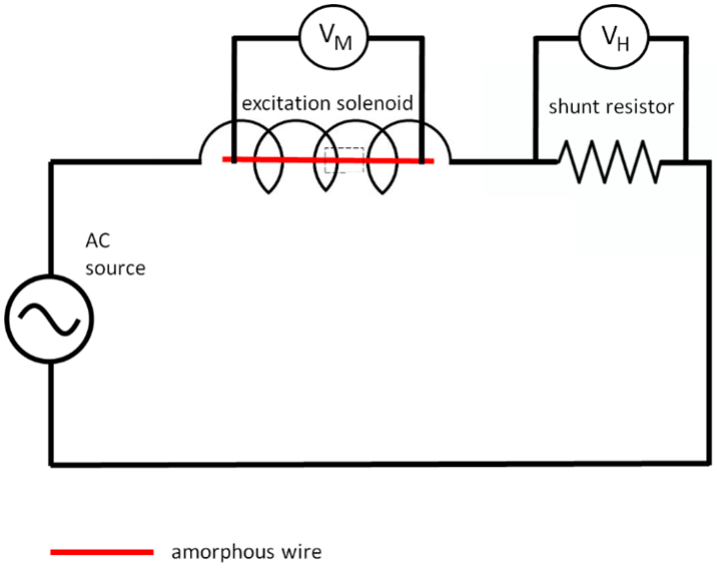

Figure 4-2: Electric circuit of the designed system

The electric circuit for the measurement system is shown in Figure 4-2. The peak magnetic field was determined from the magnetising current by measuring the voltage V_H across a 0.47 Ω non-inductive shunt resistor connected in series with the magnetising winding as shown in Figure 4-2. The value of the magnetic field, H, was calculated using Eq. (4-1) [15] assuming a long thin solenoid geometry as assumed in Eq. (2-2):

$$H = \frac{NV_m}{Rl} \tag{4-1}$$

Where N is the number of turns in the magnetising winding, l is the length of the flux path, V_m is the maximum value of the magnetising voltage and R is the shunt resistance.

The strain gauge meter used was an Omega DP25-S with an operating temperature range of 16 to 71 °C and a load cell operating range between 0 to 20 Newtons (N). Eq.(4-2) was used to calculate the axial stress (σ) using the applied force (F) and the cross-sectional area of the amorphous wire (A).

$$\sigma = F/A \tag{4-2}$$

Prior to measurements, the Load cells were calibrated using suspended known weights in the set-up shown in Figure 4-3. The weight (W) of an object due to the force of gravity on the object is defined in Eq.(4-3) as the mass (m) times the acceleration of gravity (9.81 m/s^2). The measured force was determined using Eq. (4-3). Figure 4-4 is a plot of the measured force, from the load cell, against the calculated force. The calibration was performed by loading the load cell gradually starting from zero weight to a maximum value of 4.92 N. The measurements were repeated six times before averaging, resulting in a linear plot which can be seen in Figure 4-4.The coefficient of determination (R^2) in this figure, is one. The coefficient of determination is used to analyze how differences in one variable can be explained by differences in another variable. The uncertainty of the measurements will be discussed in section 4.3.

$$F = W = 9.81m \tag{4-3}$$

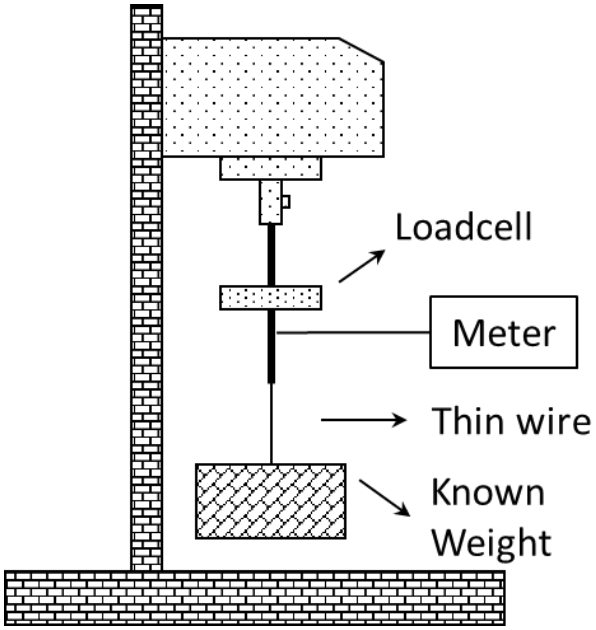

Figure 4-3: The system used to calibrate the load cells comprised of a known weight attached to the load cell vertically

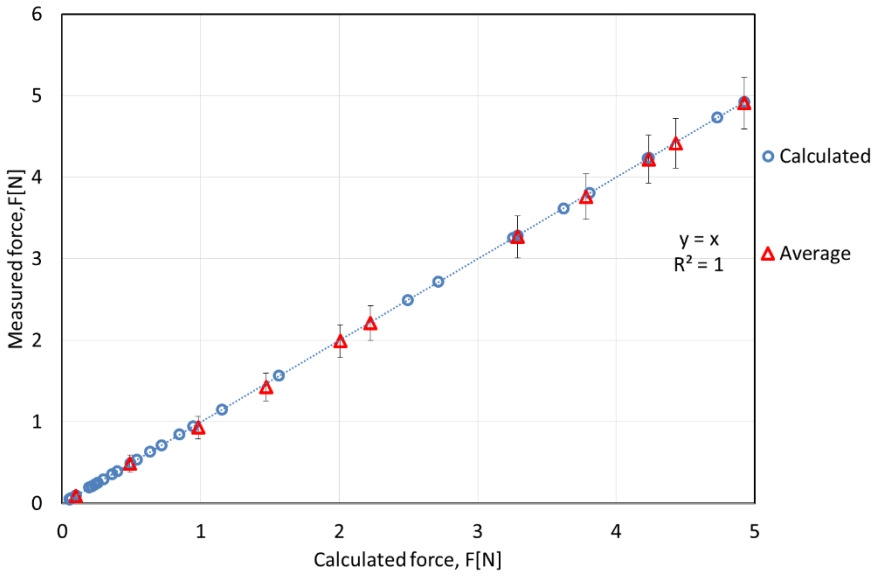

Figure 4-4: Load cell characteristic, measured force against ideal force

4.4 Uncertainty

Measurement uncertainty has many sources including instrument limitations, random environmental effects, operator error etc. There are established rules for how to calculate an overall estimate of uncertainty from these individual error contributions. The usual way to quantify spread in a reading is a standard deviation

(SD). The SD of a set of numbers tells us how different the individual readings typically are from the average of the set. The complete process of calculating the estimated SD for a series of n measurements can be expressed mathematically as:

$$S = \sqrt{\frac{\sum_{i=1}^{n}(x_i - \bar{x})^2}{(n-1)}} \quad (4\text{-}4)$$

Where x_i is the result of i[th] measurements and $\bar{x}$ is the arithmetic mean of n measurements.

There are two approaches to estimate uncertainties, type A and type B evaluations. Type A evaluations: uncertainty estimates using statistics (usually from repeated readings)

Type B evaluations: uncertainty estimates from any other information. This could be from past experience of the measurements, from calibration certificates, manufacturer's specifications, from calculations, from published information, and from common sense.

However, all contributing uncertainties should be expressed at the same confidence level, by converting them into standard uncertainties. A standard uncertainty is a margin whose size can be thought of as plus or minus one SD. The standard uncertainty tells us about the uncertainty of an average (not just about the spread of values).

When a set of several repeated readings has been taken (for A-type estimate of uncertainty), the estimated standard uncertainty u is calculated from the Eq. (4-5).

$$u = \frac{S}{\sqrt{n}} \quad (4\text{-}5)$$

Where S is standard deviation and n is the number of measurements in the set [152].

The measurements of the load cell calibration in the previews section were repeated six times and by using Eq.(4-5), the SD were calculated, then uncertainty budget was calculated in

Table 4-2. The calculated uncertainty for stress was ranging from 0.04 to 0.3 N as shown in Figure 4-4.

Table 4-2: Uncertainty budget for Load cell

	Source of uncertainty	Value	Probability distribution	Divisor	Standard uncertainty
V_{RP}	SD Repeatability of Matteucci effect	0.7 N	Normal	1	0.7 N
W	Resolution of Scale (g)	0.005 g	Rectangular	√3	0.00028 g

4.5 Matteucci voltage on positive and slightly negative amorphous wires

Figure 4-5 shows the input magnetic field and Matteucci voltage for AF10 amorphous wire. When the applied field changes direction, a voltage peak is generated at the ends of the amorphous wire as the domains are influenced by the helical anisotropy due to twisting. When the applied field changes direction, a voltage peak is produced with opposite polarity.

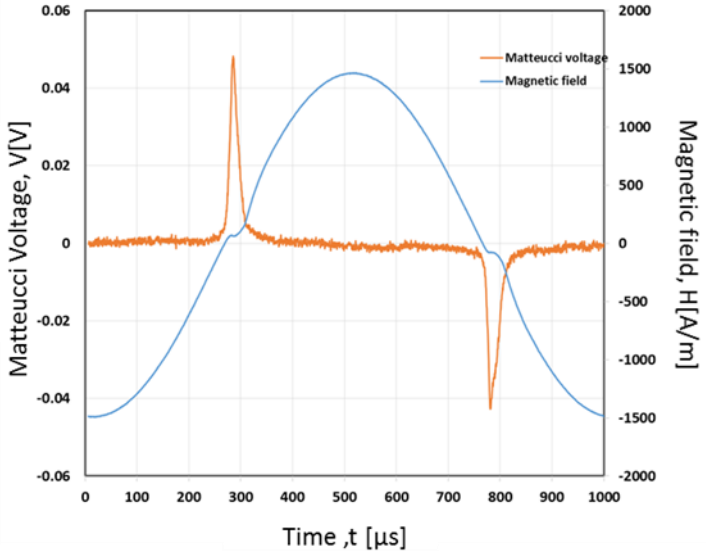

Figure 4-5: Input signal and produced Matteucci voltage for AF10 amorphous wire magnetised in 1 kHz frequency, 1.5 kA/m magnetic field, twisted 0.08 rad/cm (29.57 MPa torsion stress).

Figure 4-6 shows the output Matteucci voltage in positive magnetostrictive (AF10) and negative magnetostrictive (AC20) amorphous wires respectively. Positive magnetostrictive wires have clearly defined single positive and negative voltage peaks whereas the voltage peaks in negative magnetostrictive wire (AC20) exhibit a small peak immediately followed by a reverse peak. Under the same conditions, the Matteucci voltage for AF10 amorphous wires was almost two and a half times greater than that for AC20. Magnetic domains in the outer shell of AF10 are in the radial direction as it is shown in Figure 2-13. Applying torsion will cause the magnetic moments to rotate towards the circular direction in both the inner core and the outer shell. In AC20, the domains in the outer shell are already lined up in the circumferential direction as it is shown in Figure 2-13 [40]. As AC20 has a slightly negative magnetostriction, twisting will tend to cause the magnetic moments to align perpendicular to the torsional stress direction. Therefore, under zero axial stress conditions, the Matteucci voltage is less in AC20 compared to AF10 due to the difference in the magnitudes are their magnetostriction constants.

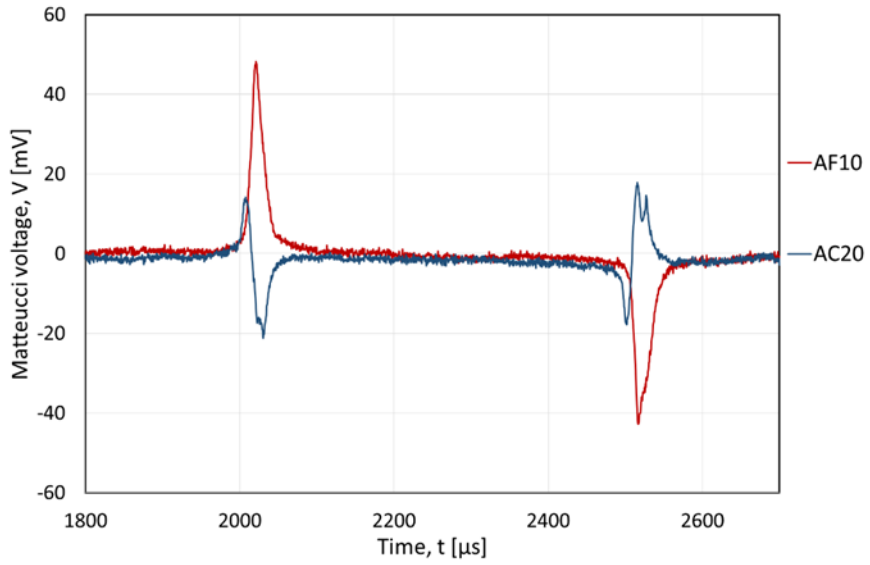

Figure 4-6: The output Matteucci voltage for AF10 and AC20 amorphous wires at 1 kHz frequency twisted 0.08 rad/cm (29.57 MPa torsion stress) by applying 55 MPa tensile stress.

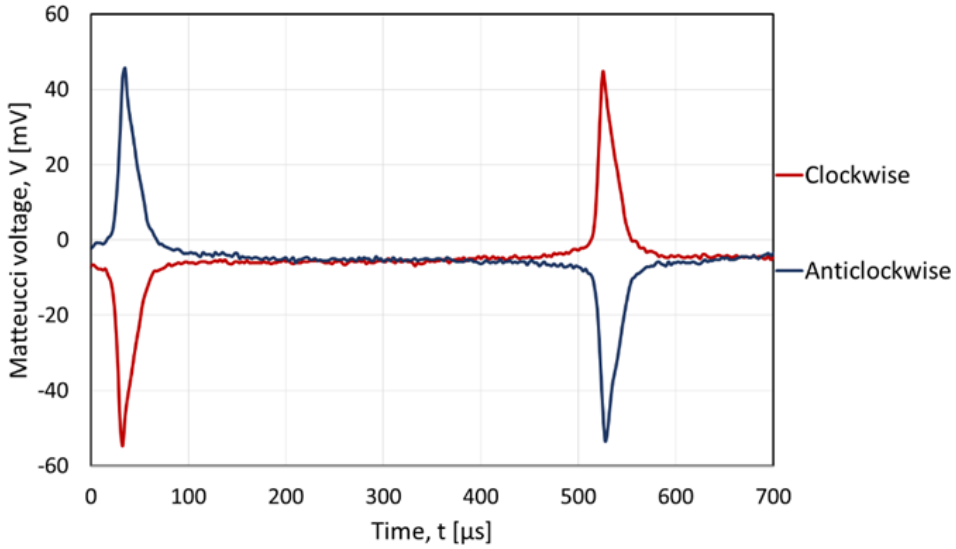

Figure 4-7: The Matteucci voltage in AF10 amorphous wire for both clockwise and anti-clockwise twisting with 1 kHz magnetisation.

Figure 4-7 shows that the Matteucci voltage reverses with a ∏ rad phase change when twisting goes from a clockwise to the anti-clockwise direction. This is because the magnetic domain orientation also changes. A schematic representation is shown in Figure 4-8 and illustrates how domains which are initially in the radial direction (Figure 4-8-a), change to a helical direction (Figure 4-8-b) by twisting anticlockwise and then reversing direction for clockwise twisting (Figure 4-8-c).

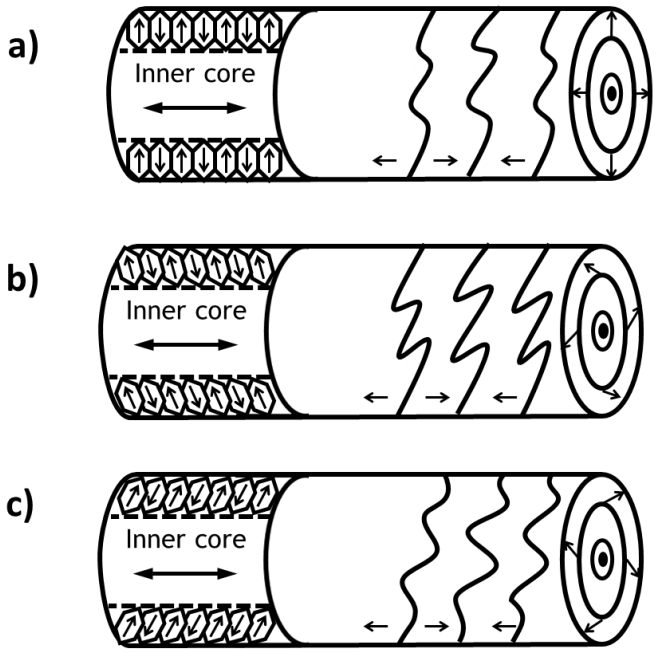

Figure 4-8: The change of the orientation of domains in AF10 amorphous wire a) domains in the radial direction, b) Twisted wire and domains changed to helical direction c) Twist inversed and domains changed direction

4.6 The influence of magnetising amplitude, magnetising frequency and length of amorphous wire on the Matteucci voltage

Figure 4-9 represents the variation of peak Matteucci voltage (V_m) versus applied field H for AF10 amorphous wire magnetised at 1 kHz frequency for different twisting angles ranging from 0.87 to 3.49 rad (corresponding to 0.08 rad/cm to 0.31 rad/cm) in 0.87 rad steps for 114 mm length amorphous wire. As the magnetic field increases, the Matteucci voltage linearly increases. This was observed for all twisting angles in the measurement range. According to the Eq.2-21, by increasing the magnetic field, the axial flux density component increases and hence the Matteucci voltage increases. Furthermore, the higher the twisting degree, the higher the induced voltage due to $\Delta M_{\emptyset}$ changes as the magnetic domains partially align with the axial field direction. The sensitivity has been calculated in Eq. (4-6) using the ratio of the change of the Matteucci voltage due to the change of the applied magnetic field.

$$\text{Sensitivity} = \frac{V1 - V2}{H1 - H2} \tag{4-6}$$

Where V1 is the voltage for magnetic field (H1) and V2 is the measured voltage for magnetic field H2. As Figure 4-9 shows the sensitivity has doubled as twisting increases from 0.87 to 3.49 rad but the linearity, as determined by the coefficient of determination (R^2), has stayed the same. The Matteucci voltage in AF10 shows very high linearity of 0.99 with changing magnetic field. It should be noted that a minimum drive field of 20 A/m at 1 kHz frequency and 0.08 rad/cm twisting angle was required for the Matteucci voltage to be observed since the wire exhibited no irreversible flux change below this value of field. In [32] it has been reported that 50 A/m is the minimum magnetic field for the Matteucci voltage to appear. The frequency and twisting angle are not mentioned in [32], and the wire length was 300 mm compared to 114 mm used in this work. Therefore, a direct comparison is not possible along with an explanation for the difference in minimum field.

Figure 4-10 shows the Matteucci effect as a function of length of AF10 amorphous wire. Increasing the length of the wire also leads to an increase in the Matteucci voltage as predicted by Eq.(2-22). Three different lengths of wire, 114 mm (in fact as 100 mm length solenoid was used to excite the amorphous wire, the effective length of the wire is 100 mm) 30 mm and 50 mm were chosen. A point to note is that the Large Barkhausen effect appears in wires more than 70 mm long. The results show that the Large Barkhausen jump does not affect the trend in Matteucci voltage with wire length. The Matteucci voltage as a function of length increases linearly with a coefficient of determination equal to (R^2) 0.92 and an output sensitivity of 0.36 mV/mm calculated from the slope in Figure 4-10.

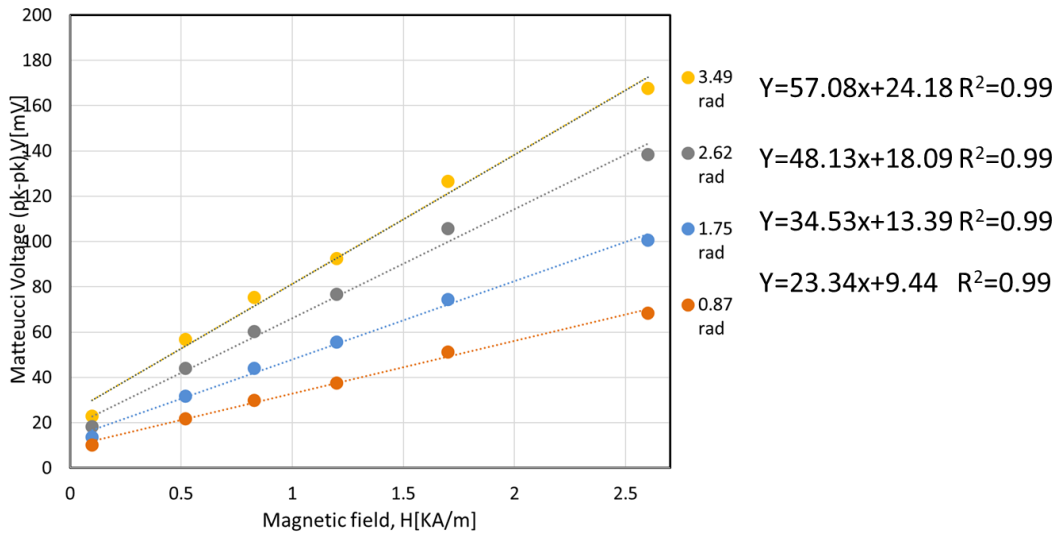

Figure 4-9: The variation of Matteucci voltage due to the magnetic field on 114 mm length AF10 Amorphous wire magnetised at 1 kHz frequency

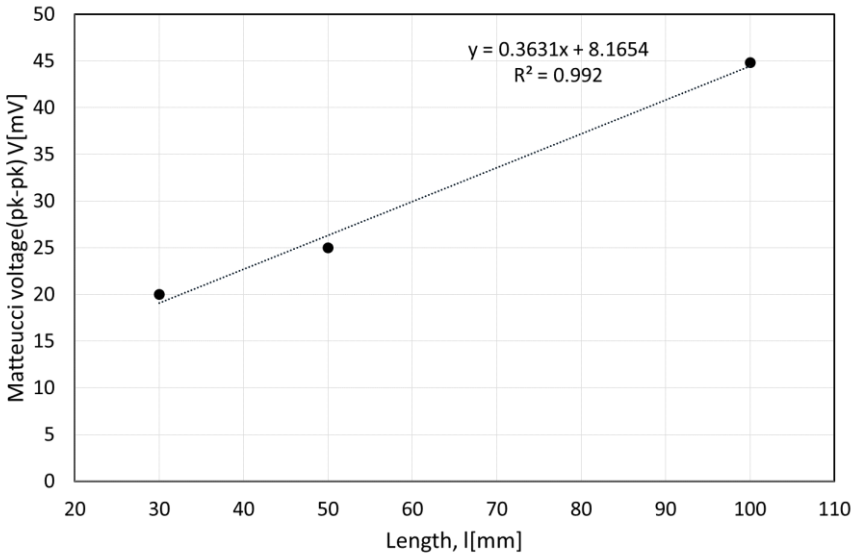

Figure 4-10: The variation of Matteucci voltage due to the length of wire, 0.08 rad/cm twisting angle (29.57 MPa torsion stress) on 114 mm, 50 mm and 30 mm AF10 amorphous wire which is magnetised in 1 kHz and 1.49 kA/m magnetic field

4.7 Influence of tensile and torsion stress on the Matteucci voltage

Figure 4-11 and Figure 4-12 illustrates the variation of the peak to peak Matteucci voltage as a function of twist angle and magnetising frequency for 114 mm lengths of AF10 and AC20 amorphous wires with a 55 MPa tensile stress. This level of stress was chosen because of the high Matteucci voltage shown in Figure 4-14, whilst avoiding the region below 55 MPa which provided reduced voltages at frequencies higher than 7 kHz. For both wires to be comparable with each other the same tensile stress has been chosen for AC20 amorphous wire. The experiments were repeated three times to average the data shown in Figure 4-11 and Figure 4-12. The uncertainties were measured using Eq.(4-5) and are shown as errors bars for each point in Figure 4-11 and Figure 4-12. Increases in excitation frequency and angle of twist both led to increases in Matteucci voltage due to Faraday's law of induction the faster the flux variance in the region higher the Matteucci voltage, and increased helical anisotropy. A comparison of the two compositions reveals similar behaviour with both exhibiting some degree of asymmetry dependent on the direction of the twist. The most striking difference is in the amplitude of the

Matteucci voltage being approximately two and a half times greater in the positively magnetostrictive alloy compared with the negative magnetostrictive alloy. It seems that Matteucci voltage saturates after certain volume of twist which is because of domains have moved to helical direction and twisting more does not have any influence in Matteucci voltage.

To calculate torsion stress from twist the following equation is used [153]:

$$\tau = \frac{G \times \theta \times r}{L} \qquad (4\text{-}7)$$

Where θ is twisting angle, G is shear modulus, r is the radius of wire and L is the wire length. For AF10 amorphous wire G is 62 GPa according to [154]. The same number is assumed for AC20 in this equation. Therefore, for the twisting angle from 0 to 2∏ rad, the torsion stress is calculated from 0 to 213 MPa.

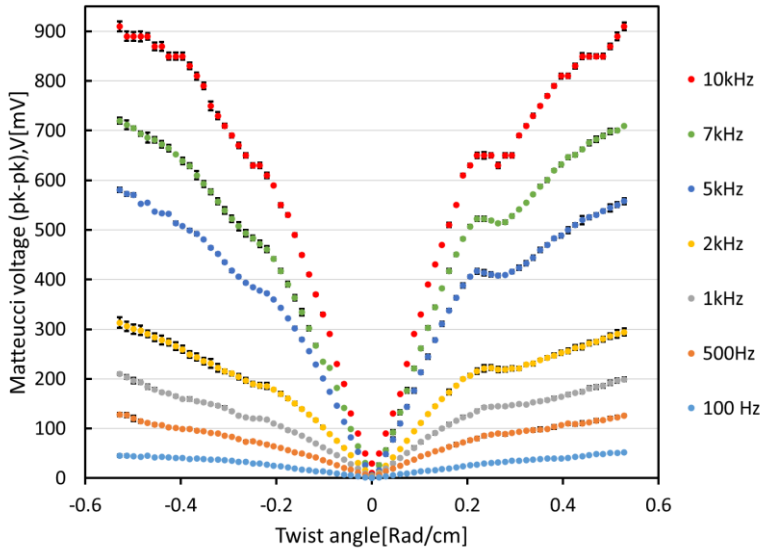

Figure 4-11: The variation of Matteucci voltage due to the twisting angle on 114 mm AF10 amorphous wire with 55 MPa tensile stress.

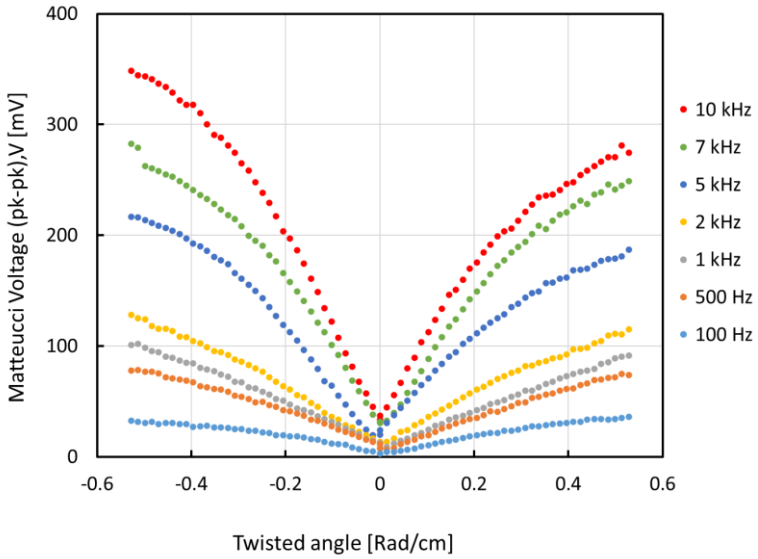

Figure 4-12: The variation of Matteucci voltage due to the twisting angle on 114 mm AC20 amorphous wire with 55 MPa tensile stress.

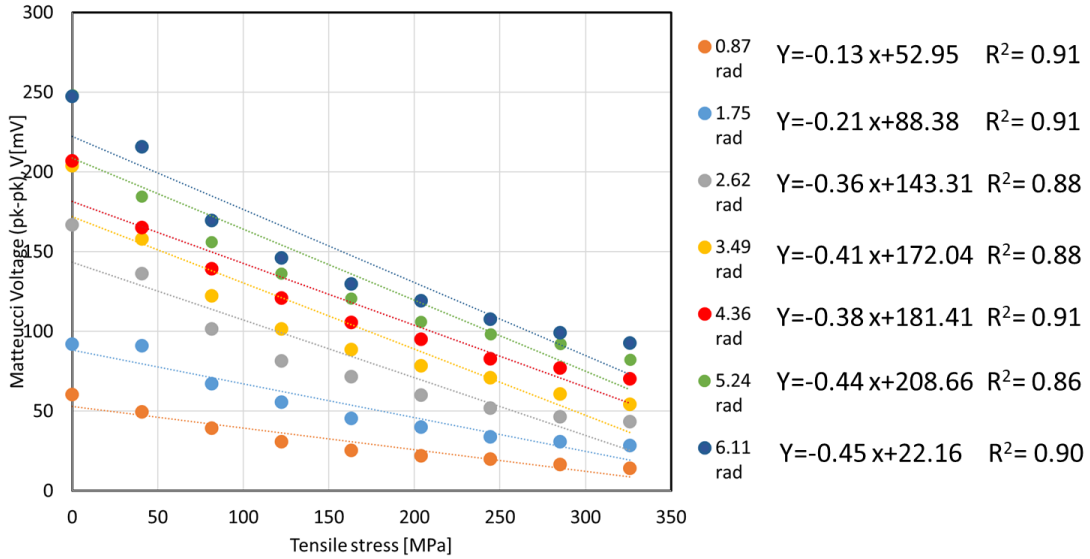

Figure 4-13: The variation of Matteucci voltage due to tensile stress and twisting on 114 mm AF10 amorphous wire magnetised in 1.49 kA/m and 1 kHz magnetic field

Figure 4-13 shows the variations of Matteucci voltage due to tensile and torsion stress on 114 mm length AF10 amorphous wire. As it can be seen, tensile stress varies from 0-326 MPa while torsion stress changes from 29.57 to 207.34 MPa according to Eq.(4-8). Figure 4-13 shows the sensitivity of the Matteucci effect increases from 0.13 to 0.45 mV/MPa by increasing the twisting angle. The coefficient of determination is approximately 0.9 for all twist angles indicating that the linearity is similar in all cases. In later measurements, 0.87 rad was chosen as

a suitable twist angle (0.08 rad/cm (29.57 MPa torsion stress) for 114 mm wire) because this falls within the linear range before plateauing in Figure 4-11. The variation of peak Matteucci voltage with tensile stress with a fixed twist angle for 114 mm lengths of AF10 and AC20 wire are shown in Figure 4-14 and Figure 4-15 respectively. In this case, the magnetising frequency range was 100 Hz to 10 kHz for AF10, and 1 kHz to 10 kHz for AC20 with a twist angle of 0.08 rad/cm. Tensile stress was applied from 0 to 326 MPa. The frequency range of AC20 was reduced because the Matteucci voltage was too small to measure at the lower frequencies. The behaviour of each type of wire is distinct and attributable to the difference in the sign of their magnetostriction. The sign of the magnetostriction coefficient significantly influences the domain structure in amorphous wire with circumferential and radial domain patterns in AC20 and AF10 respectively [40]. In AF10 amorphous wire, the Matteucci voltage decreases as tensile stress rotates the magnetisation vector away from the helical direction. However, in AC20 amorphous wire, the Matteucci voltage increases with increasing axial stress as more domains become aligned in the circumferential magnetisation direction. In addition, Figure 4-15 indicates that sensitivity to tensile stress increases from 0.12 to 0.21 mV/MPa with increasing frequency. As in AC20 amorphous wire axial stress will increase circumferential anisotropy even further because of negative magnetostriction. The maximum SD in both Figure 4-14 and Figure 4-15 were 0.02, 0.03 respectively and the minimum SD was 0.00 for both cases.

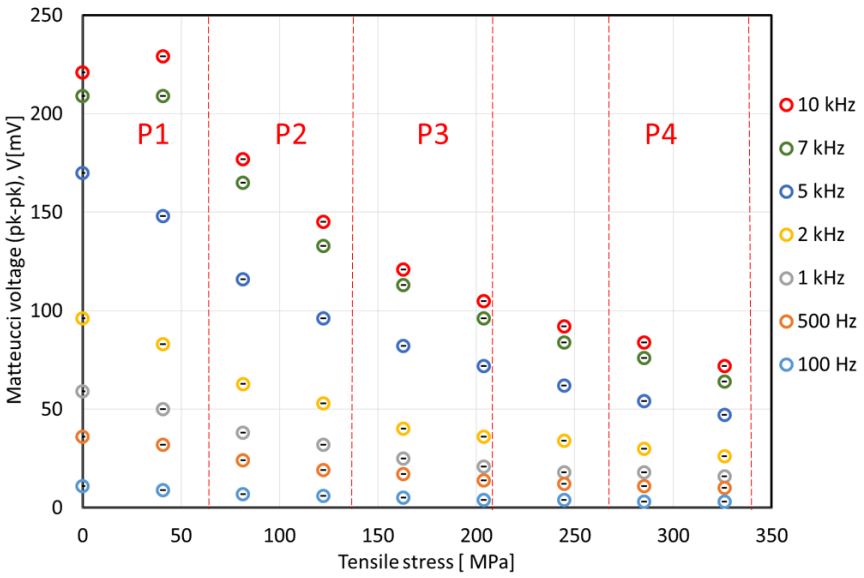

Figure 4-14: The variation of Matteucci voltage due to tensile stress on 114 mm AF10 amorphous wire with a 0.08 rad/cm twist angle (29.57 MPa torsion stress).

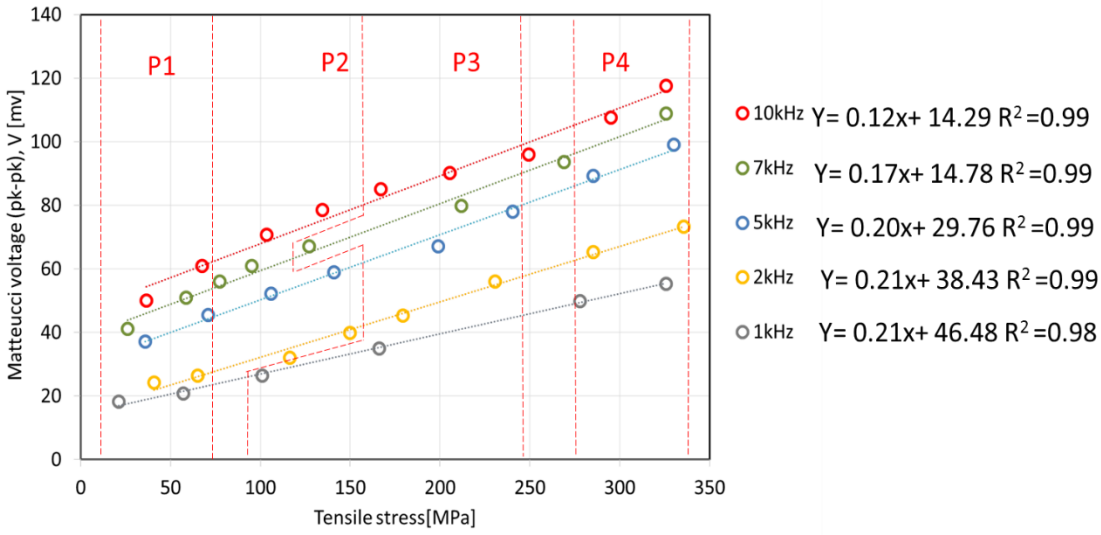

Figure 4-15: The variation of Matteucci voltage due to tensile stress on 114 mm AC20 amorphous wire with a 0.08 rad/cm twist angle (29.57 MPa torsion stress).

Finally, Figure 4-16 shows the Matteucci voltage due to the tensile stress on a 45 mm length of AF10 amorphous wire. The Matteucci voltage decreases as tensile stress increases as also seen in the longer wires (Figure 4-14). As expected, the Matteucci voltage is lower in amplitude compare to 114 mm length amorphous wire but the linearity has increased to a maximum of 0.93 (R^2 value) at 5 kHz.

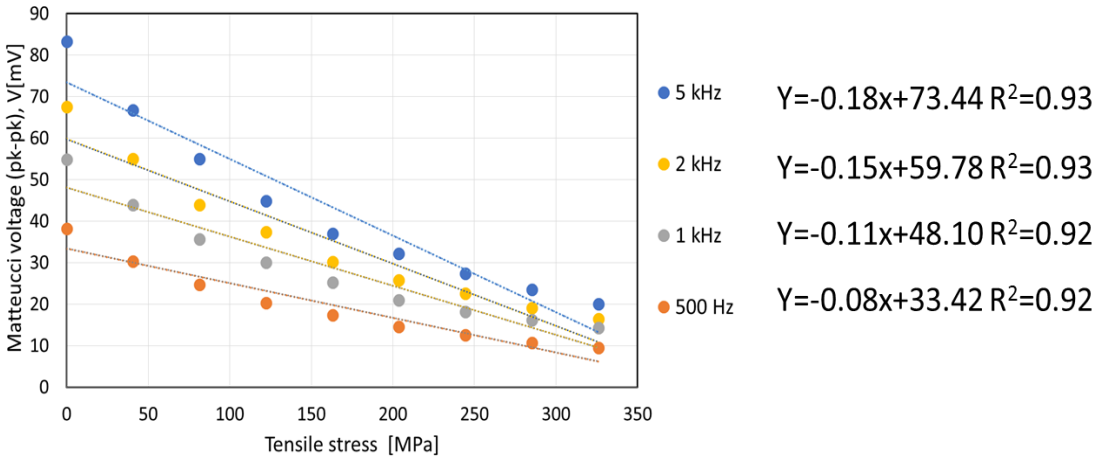

Figure 4-16: The variation of Matteucci voltage due to tensile stress on 45 mm AF10 amorphous wire with a 0.19 rad/cm twist angle (74.92 MPa torsion stress).

4.8 Gauge factor

For strain gauges, the Gauge factor (GF) is the ratio of relative change in electrical resistance R to the mechanical strain ε. The gauge factor is defined as:

$$GF = \frac{\frac{\Delta R}{R}}{\frac{\Delta L}{L}} = \frac{\frac{\Delta R}{R}}{\varepsilon} \tag{4-8}$$

Where ΔL is the absolute change in length, ΔR is the change in strain gauge resistance due to axial strain and R is the unstrained resistance of strain gauge.

To evaluate the sensitivity of amorphous wires, an equivalent strain gauge factor for AF10 and AC20 amorphous wires was calculated. To derive the strain (ε) from the measured stress (σ) we assumed a value of 1.58 x 10^{11} Pa [155] for the Young's modulus of amorphous wire and used Eq.(4-9).

$$\varepsilon = \frac{\sigma}{E} \tag{4-9}$$

$$Equivalent\ Gauge\ Factor = \frac{\Delta v_m}{v_m} \times \frac{1}{\varepsilon} \tag{4-10}$$

Eq.(4-10) defines an equivalent gauge factor using the change in Matteucci voltage which is defined in Eq.(4-11). v_i is the Matteucci voltage for different stresses and v_0 is the initial Matteucci voltage with no stress. ε is the strain in the wire defined by Eq.(4-9). Equivalent gauge factors (EGF) for AC20 and AF10 114 mm length

amorphous wires were calculated at frequencies ranging from 0.1 kHz to 10 kHz and a 0.08 rad/cm twist angle.

$$\frac{\Delta v_m}{v_m} = \frac{v_{i+1} - v_i}{v_0} \tag{4-11}$$

Figure 4-17 and Figure 4-18 show the EGF measured for AF10 and AC20 in four tensile stress regions indicated by P1 to P4 in Figures 4-14 and 4-15. For the parameters given above, the highest EGF for AF10 was 70 at 100 Hz. This data shows that the stress sensitivity of the Matteucci voltage in AF10 drops off with stress amplitude but the EGF dependence with frequencies is less clear. In contrast, AC20 has higher EGF's with a best value of 150 at 2 kHz. There are smaller variations in EGF over the whole stress range which is indicative of AC20's better linear variation of Matteucci voltage with stress.

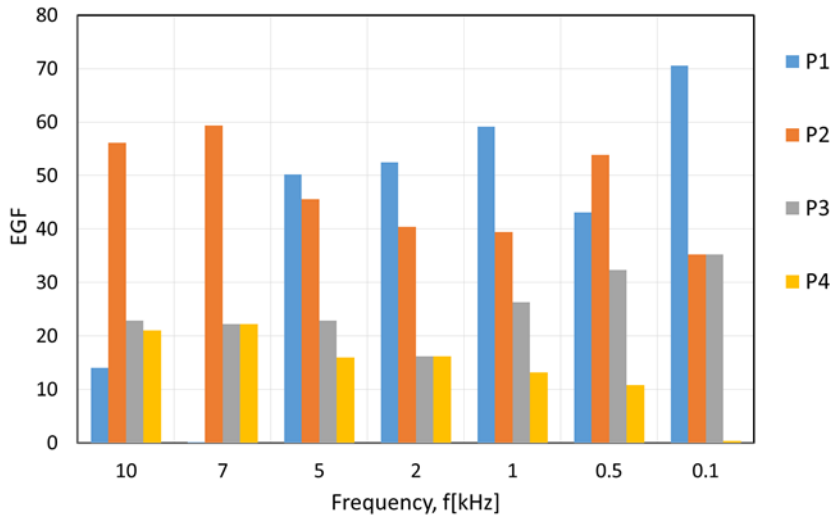

Figure 4-17: The sensitivity of AF10 amorphous wire in frequencies from 100 Hz to 10 kHz in different positions which are marked in Figure 4-14.

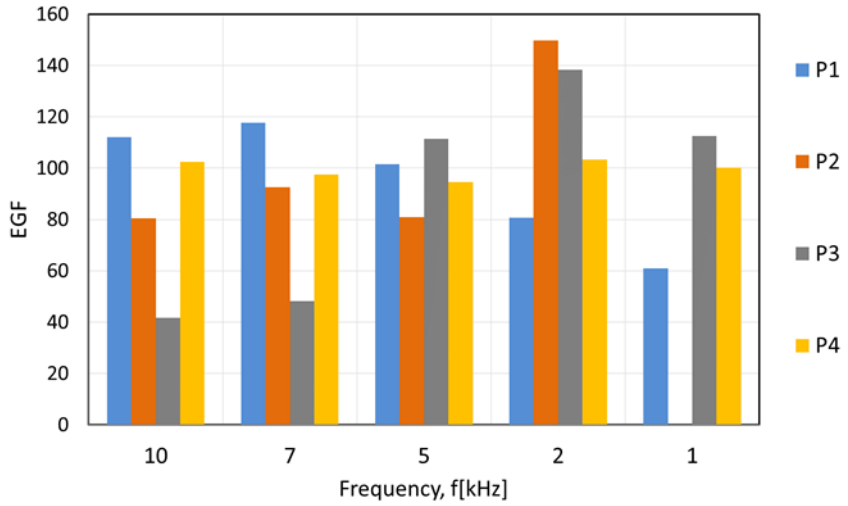

Figure 4-18: The sensitivity of AC20 amorphous wire in frequencies from 100 Hz to 10 kHz in different positions which are marked in Figure 4-15.

4.9 DC and AC B-H curves

B-H measurements were performed on 114 mm length and 125 μm diameter as-cast and annealed AF10 and AC20 amorphous wires by applying a DC magnetic field using a 585 mm long solenoid with 364 turns. The magnetic field (H) was calculated from Eq.(4-1) by measuring the current passing through a resistor (1.3 Ω). AF10 was annealed by passing 0.5 A current for 1 min through the wire.

The flux density (B) was measured by using a flux meter connected to a secondary pick-up coil with 12 layers, a total of 10330 turns, 60 mm in length and a cross-sectional area of 9.45 mm^2. To compensate for the air flux, the amorphous wire was removed from the coil and the air flux measured. This was then subtracted from the flux measurements obtained with the wire present. The electrical circuit schematic and the measurement system for measuring the B-H curve are shown in Figure 4-19 and Figure 4-20 respectively. As it can be seen the existing setup consists of a power amplifier (Kepco) to amplify the DC current which passes through the excitation coil, a flux meter (Lakeshore, 480) was connected to the secondary coil to measure the magnetic flux density (B). As Figure 4-19 shows the output of the flux meter and current across the shunt resistor were controlled using a LabVIEW program.

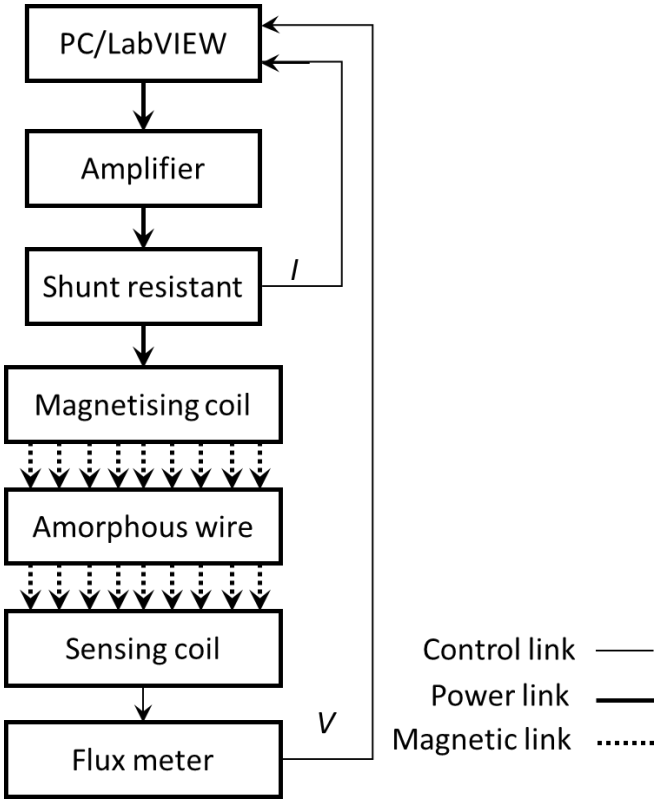

Figure 4-19: Schematic of the electrical circuit for measuring B-H curve and Matteucci voltage.

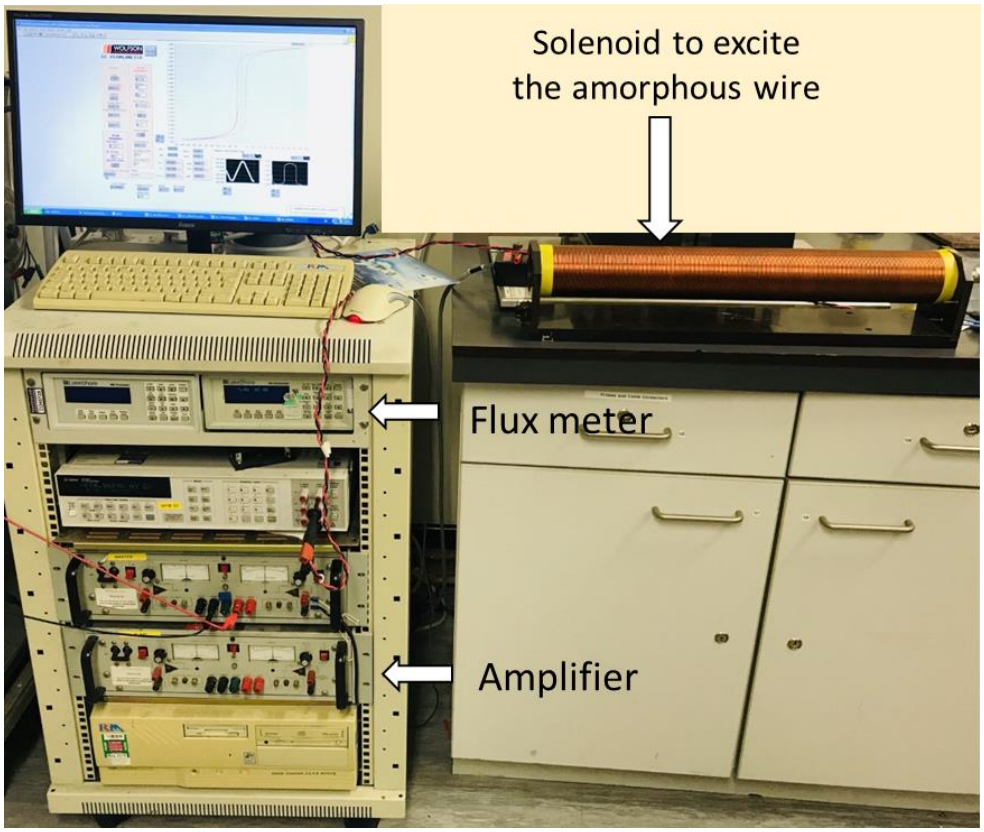

Figure 4-20: The system designed to measure B-H loop

AC B-H measurements were performed on 114 mm length AF10 and AC20 amorphous wires by applying a sinusoidal magnetisation field (1.5 kA/m amplitude, 1 kHz) using a 100 mm long solenoid, 5 mm in diameter and 168 number of turns. The magnetic field (H) and flux density (B) were calculated from Eq.(4-1) and (4-12) respectively. To compensate for air flux, two identical coils were connected in series-opposition with only one coil enwrapping the amorphous wire as shown in Figure 4-21.

$$B = \frac{\int V_M}{NA} \tag{4-12}$$

In this equation V_M is the voltage of the secondary coil around the amorphous wire, A is the cross-sectional area of the amorphous wire, N is the number of turns of the secondary coil, i.e. 111.

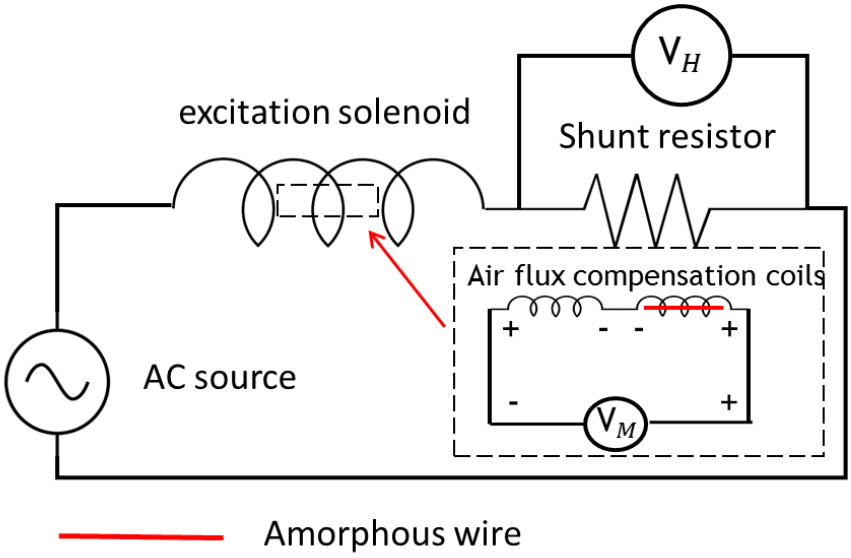

Figure 4-21: Electric circuit to measure the AC B-H curve

Figures 4-22 to 4-24 show the effect of annealing AF10 by passing a 0.5 A current for 1 min through the amorphous wire in air. In Figure 4-22, the B-H curves for as-cast and annealed AF10 amorphous wire exhibit a clear difference in their shapes. In the case of the annealed wire, the approach to magnetic saturation occurs more rapidly compared with the as-cast wire. This is even clearer in Figure 4-24 which shows that the annealed wire is closer to saturation at 5 kA/m. Inspection of the hysteresis loops at very low field shows an obvious difference between two wires. The annealed wire exhibits a distorted B-H characteristic in the first quadrant unlike the as-cast wire which exhibits the classic single Barkhausen jump that occurs in AF10 wires with lengths exceeding 70 mm [40]. It is unclear what is causing the

distorted B-H loop but it may be an indication of partial crystallisation resulting in the presence of two different magnetic phases.

Figure 4-23 shows the coercivity field and Residual magnetic flux for the as-cast amorphous wire is 4.5 A/m and 0.7 T respectively, and for the annealed wire is 3.1 A/m and 0.57 T respectively. The coercivity field has decreased as a result of annealing along with a reduction in the residual magnetic flux.

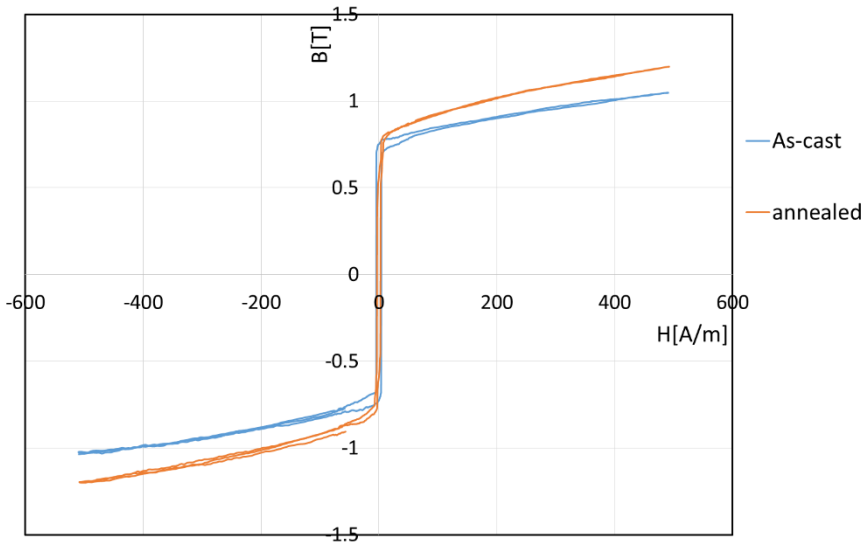

Figure 4-22: DC B-H curve with magnetic amplitude of 500 A/m for as-cast and annealed AF10 amorphous wire with air compensation

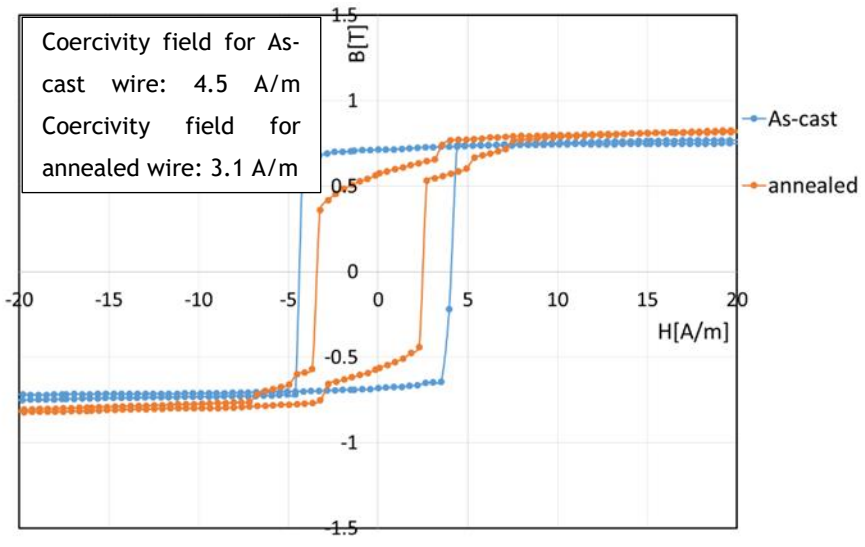

Figure 4-23: Zoomed DC B-H curve for as-cast and annealed AF10 amorphous wire with air compensation

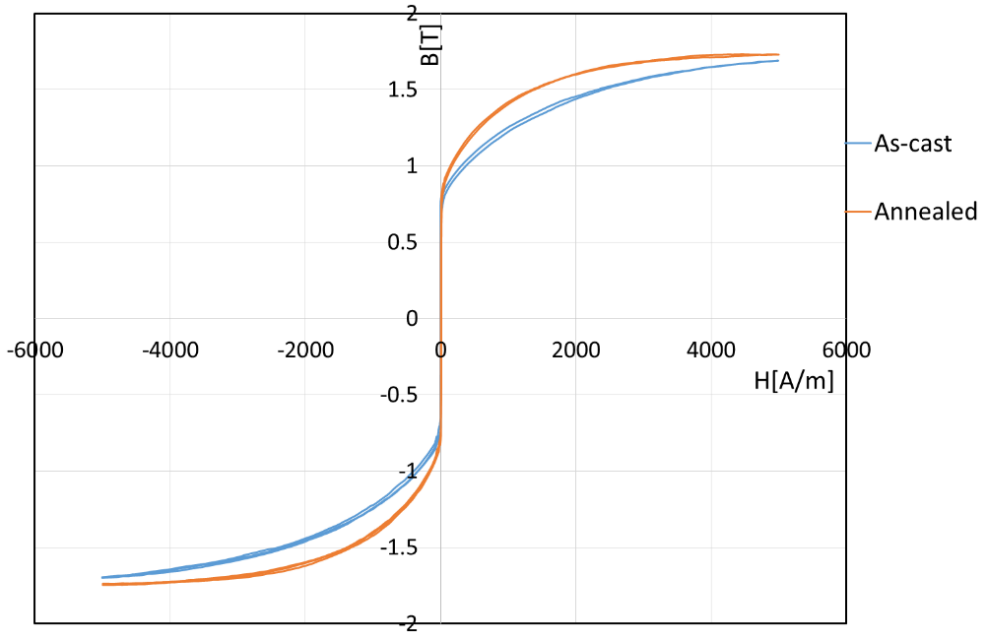

Figure 4-24: DC B-H curve with magnetic amplitude of 5 kA/m for as-cast and annealed AF10 amorphous wire with air compensation

In Figure 4-24, the B-H curves at 5 kA/m show a magnetisation of 1.7 T and 1.73 T for as-cast and annealed AF10 respectively. This is very close to what is reported for as-cast AF10 amorphous wire by Unitika which is 1.6 T [28].

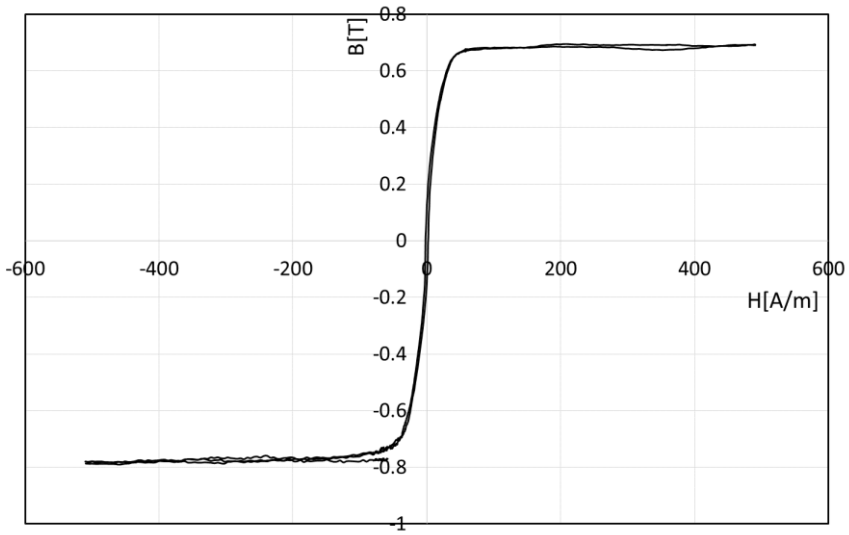

Figure 4-25: DC B-H curve with magnetic amplitude of 500 A/m for AC20 amorphous wire with air compensation

Figure 4-25 shows the B-H curve, at low fields, for AC20 amorphous wire exhibited an s-shaped hysteresis as reported in [9]. Figure 4-26 shows the coercivity field and Residual magnetic flux for AC20 amorphous wire equalled 1.9 A/m and 0.11 T

respectively. Compared with the positive magnetostrictive wire (AF10) it shows less coercivity field and residual magnetic flux.

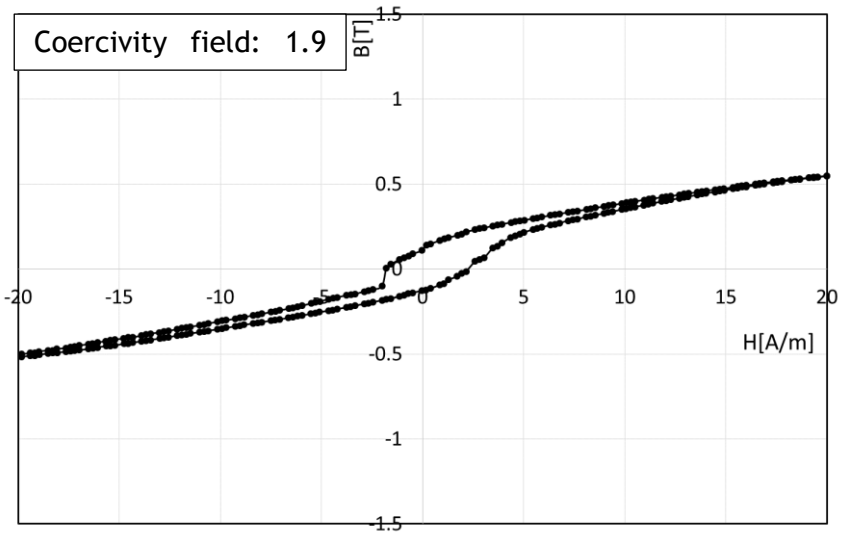

Figure 4-26: DC B-H curve for AC20 amorphous wire with air compensation

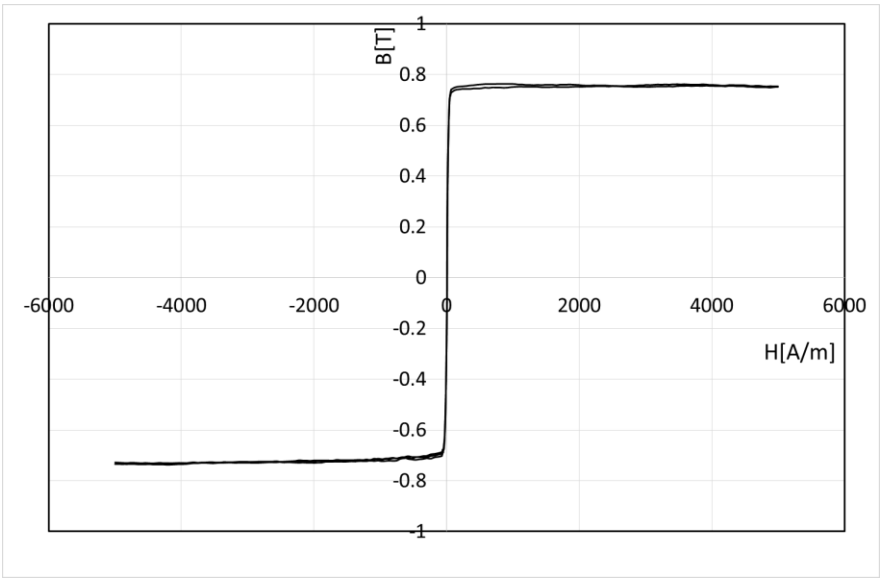

Figure 4-27: DC B-H curve with magnetic amplitude of 5 kA/m for AC20 amorphous wire with air compensation

Figure 4-27 shows the saturation magnetisation is 0.72 T for AC20 amorphous wire. This is very close to what is reported by Unitika which is 0.8 T [28].

To conclude, AF10 amorphous wire has a squarer B-H curve compared to AC20 amorphous wire due to a large Barkhausen jump as reported in the literature [40]. Secondly, AC20 has less coercivity and residual flux density than AF10 and saturates at much lower magnetising fields. And finally, coercivity and residual magnetic flux

for annealed AF10 wire are less than as-cast wire because annealing reduces the stress anisotropy inside the wire [17].

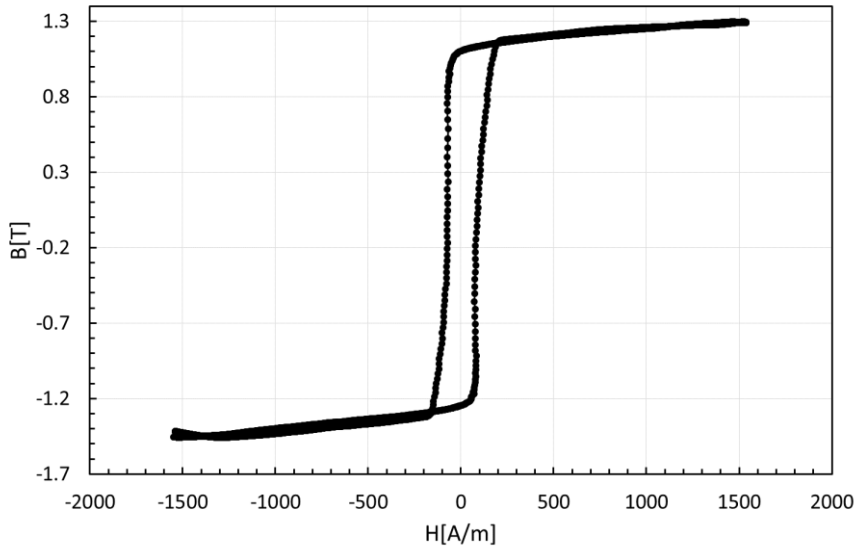

Figure 4-28: AF10 amorphous wire AC B-H curve magnetised in 1.49 kA/m and 1 kHz frequency

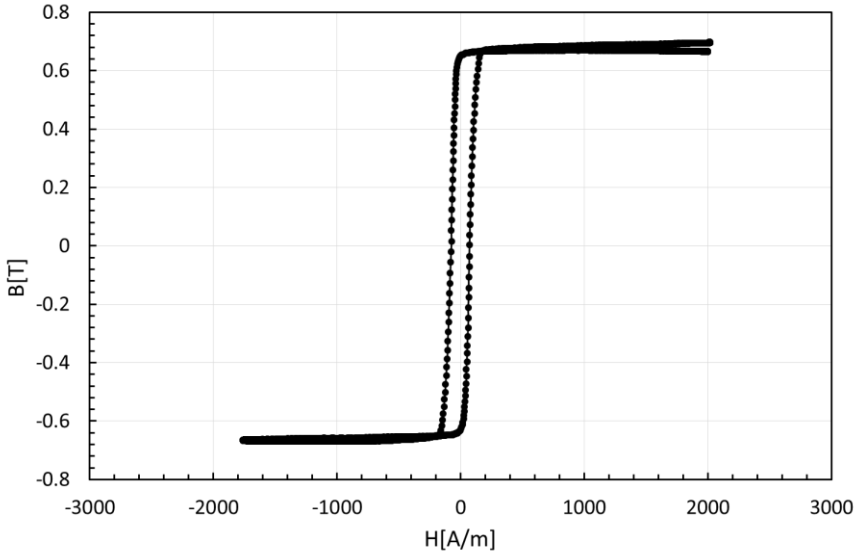

Figure 4-29: AC20 amorphous wire AC B-H curve magnetised in 1 kHz frequency

To investigate the AC character of AF10 and AC20, B-H curves were obtained at 1 kHz magnetisation as shown in Figure 4-28 and Figure 4-29. The saturation magnetisation was 1.42 T and 0.7 T and the coercivity field was 76 A/m, and 72 A/m for AF10 and AC20 respectively. The coercivity fields were higher than those observed for DC magnetisation because of eddy currents at higher frequencies. The

skin effect is the tendency of an AC current to become distributed within a conductor such that the current density is largest near the surface of the conductor, and decreases with greater depths in the conductor. The electric current flows mainly at the "skin" of the conductor, between the outer surface and a level called the skin depth. The skin effect causes the effective resistance of the conductor to increase at higher frequencies where the skin depth is smaller, thus reducing the effective cross-section of the conductor. The skin effect is due to opposing eddy currents induced by the changing magnetic field resulting from the AC current.

4.10 X-ray results

X-rays are transverse electromagnetic radiation, like visible light but with a shorter wavelength. The range of wavelengths which is commonly used for X-ray crystallography is between 0.5 to 2.5 Å [156].

Atoms scatter X-ray waves, primarily through the atoms' electrons. An X-ray striking an electron produces secondary spherical waves emanating from the electron. This phenomenon is known as elastic scattering, and the electron is known as the scatterer. A regular array of scatterers produces a regular array of spherical waves. Although these waves cancel one another out in most directions through destructive interference, they add constructively in a few specific directions, determined by Bragg's law:

$$2d \sin\theta = n\,\lambda_w \qquad (4\text{-}13)$$

Here d is the spacing between diffracting planes, θ is the incident angle, n is any integer, and λ_w is the wavelength of the beam. These specific directions appear as spots on the diffraction pattern called reflections. Thus, X-ray diffraction results from an electromagnetic wave (the X-ray) impinging on a regular array of scatterers (the repeating arrangement of atoms within the crystal).

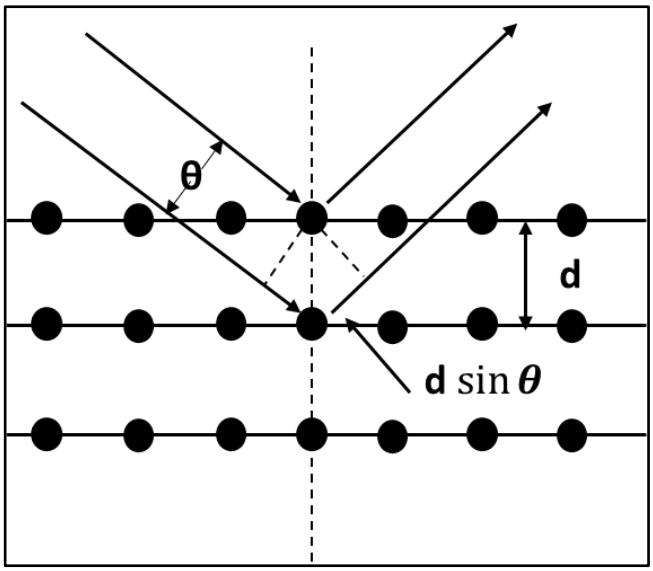

Figure 4-30: Interference between waves originating at two scattering centres

As Figure 4-30 shows, the incoming beam (coming from upper left) causes each scatterer to re-radiate a small portion of its intensity as a spherical wave. If scatterers are arranged symmetrically with a separation *d*, these spherical waves will be in sync (add constructively) only in directions where their path-length difference $2d \sin\theta$ equals an integer multiple of the wavelength λ_w . In that case, part of the incoming beam is deflected by an angle 2θ, producing a reflection spot in the diffraction pattern [156].

To confirm the amorphous nature of AF10 and AC20, wires of both types, and of pure iron as a reference sample, were cut into lengths of 30 mm for X-ray analysis. 50 lengths of each type were glued on to glass slides to form a continuous and homogeneous surface. Table 4-3 shows details of the X-Ray machine settings for these experiments. X-ray wavelength was 1.59 Å for AF10 amorphous wire and 1.79 Å for AC20 and Fe, the step size was 0.02 and scan step time 0.6 s for AF10 and 0.5 s for AC20 and Fe. The X-ray results for AF10, AC20 and Fe are presented in Figure 4-31. The x-axis in the chart refers to the scattering angle 2θ (Theta) and the y-axis refers to the intensity of photons per second. Figure 4-31 confirms that AF10 and AC20 are primarily amorphous. AC20 is highly amorphous as no peaks were detected in its X-ray characteristic. Slightly partial crystallinity was observed in AF10 with Bragg spacings at 5.49 ± 0.03 Å and 3.64 ± 0.03 Å. Both peak sizes are very small, with one of them indicating the possible presence of Fe_2O_3 (Bragg spacings of 3.67 Å) [157] due to oxidation over time. In the crystalline iron wire, two distinct Bragg spacings were detected at 2.03 Å and 1.43 Å corresponding to a body centre

cubic iron phase. The results demonstrated that compared to the crystalline iron sample, both AF10 and AC20 have maintained their amorphous nature despite having been in storage for a number of years.

Table 4-3: X-Ray settings

Material	Wavelength, K-Alpha2 [Å]	Step size [2*Theta]	Scan step time [s]
AF10	1.59	0.02	0.6
AC20	1.79	0.02	0.5
Fe	1.79	0.02	0.5

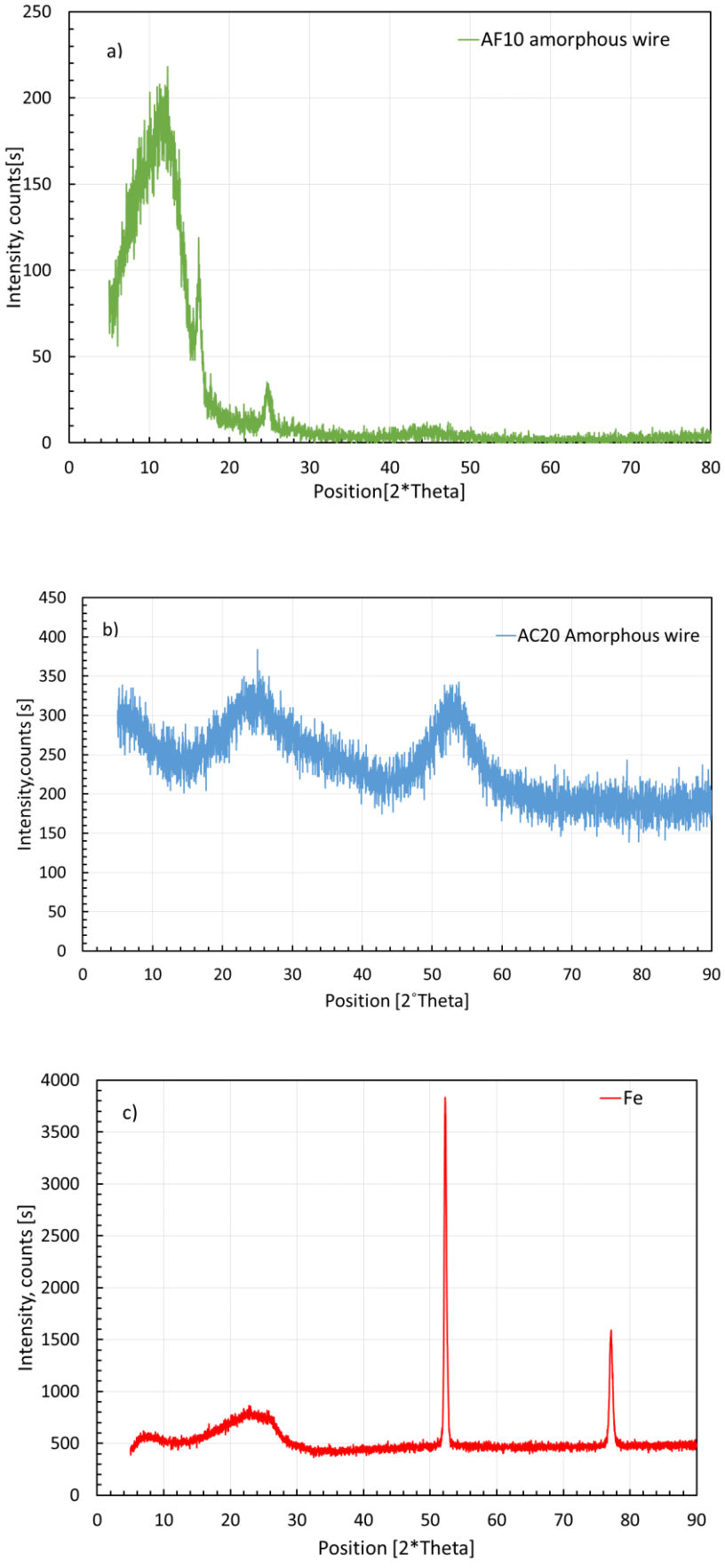

Figure 4-31: a) X-ray results on AF10 b) AC20 amorphous wires compare to c) Fe

4.11 Domain imaging

Two different types of domain imaging methods, the Bitter technique and Kerr microscopy were performed on AF10 and AC20 amorphous wires as they help us to have a better understanding of the magnetic anisotropy of the material.

4.11.1 Bitter technique

The Bitter technique combined with optical microscopy was used for magnetic domain observations. The Ferro fluid (DHYS1-A Hydro domain observation fluid) used in this investigation was supplied by Liquids Research Ltd (viscosity $\eta < 5$cp, mean particle size 6 nm and saturation magnetisation 8 mT). To enhance the image contrast, a magnetic field of 1.1 kA/m (see Figure 4-32) was generated perpendicular to the wire axis using a 126 turn coil measuring 20 mm deep and 90 mm diameter. Prior to observation, to see the influence of twisting on domains structure, the wires were manually twisted and glued to a glass microscope slide. To ensure a uniform field in the region of interest, wire lengths were restricted to 50 mm in length.

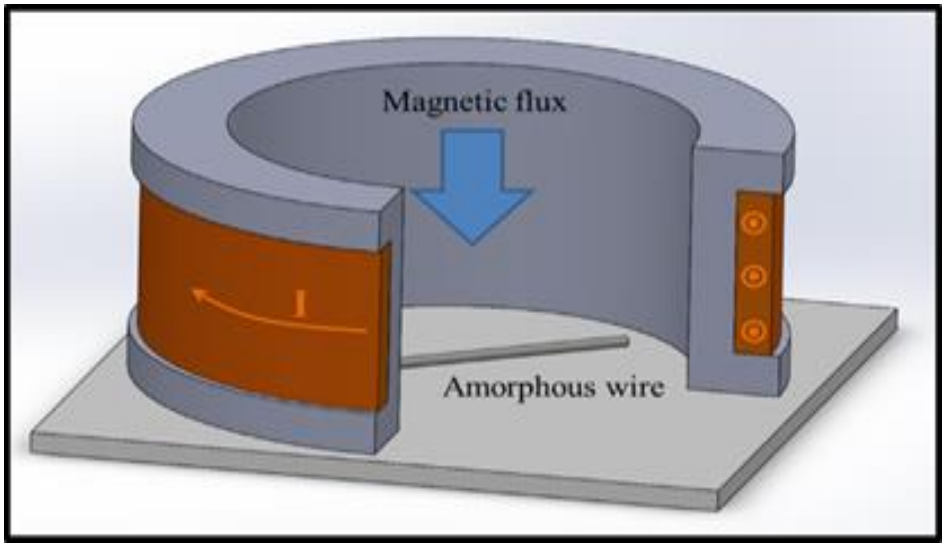

Figure 4-32: The set-up used for generating the field for contrast enhancement

Figure 4-33 consists of a series of images showing the evolution of the magnetic domain structure with increasing torsion. There is a clear transition from a circumferential zigzag pattern to an arrangement of regularly spaced parallel domain walls running oblique to the wire circumference. Closer inspection of the region between the zigzag walls reveals a fine structure of bar domains. This is

consistent with the formation of closely spaced closure domains associated with the radial domain structure previously reported in $Fe_{77.5}Si_{7.5}B_{15}$ wires [50]. As the helical

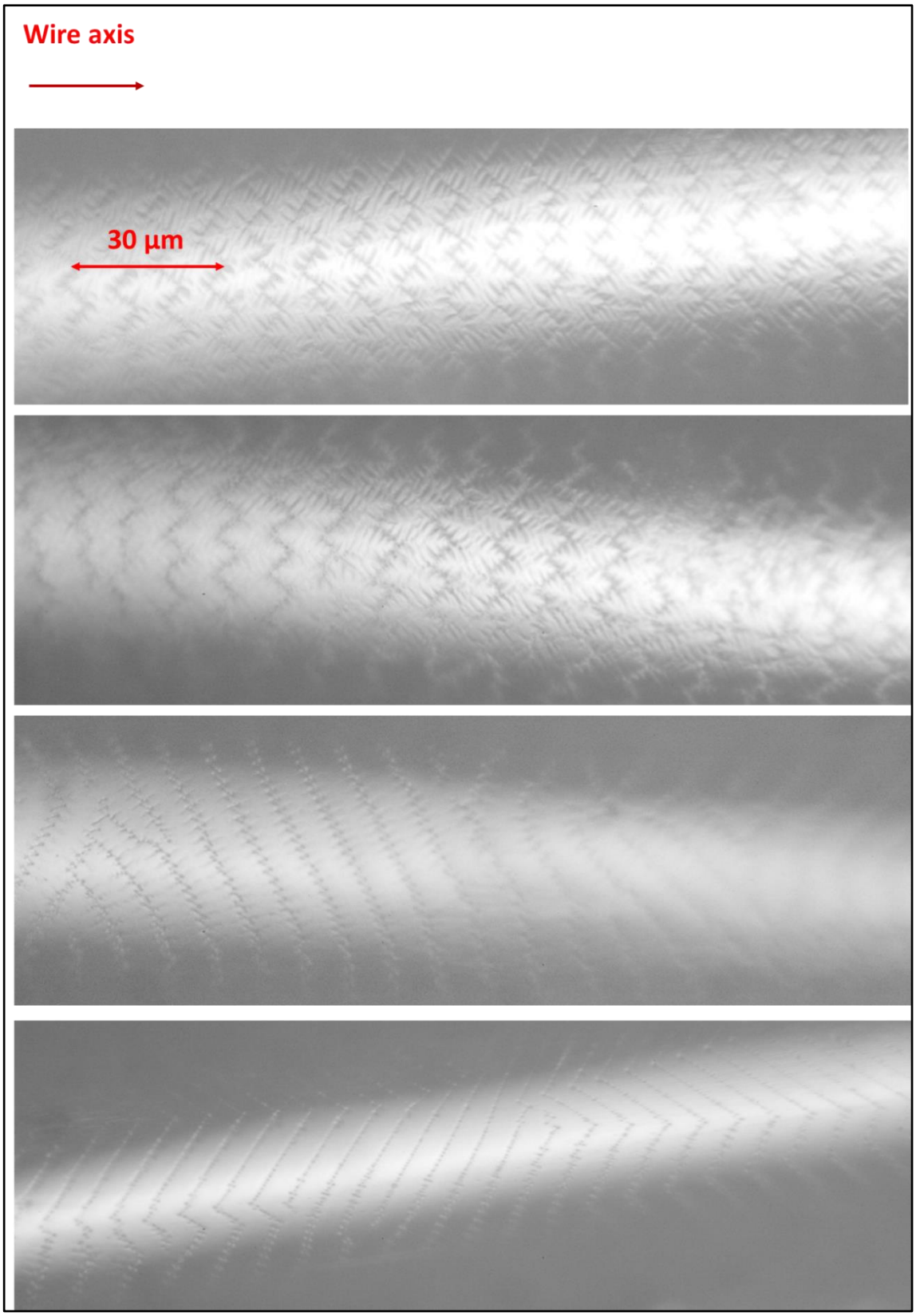

Figure 4-33: Domain structure of a 50 mm length AF-10 Amorphous wire with an applied perpendicular magnetic field of 1.1 kA/m and twist angles of a) zero, b) Π/2, c) Π and d) 2Π.

anisotropy increases, the fine domain structure disappears leading to the parallel wall arrangement consistent with domain magnetisation coincident with the wire surface and the directions of maximum shear stress. Mohri et al. [48] also observed zig-zag walls by using the Bitter technique on AF10 amorphous wire which is explained in chapter 3 in detail.

4.11.2 Kerr microscopy

The influence of the magnetisation on the state of light are known as magneto-optical effects. One particular type of magneto-optical effect is the Kerr effect which is extensively for magnetic domain imaging.

Kerr microscopy is best performed on an optically flat plane surface, in this work however, the curved wire surface limited the field of view that was possible. Furthermore, to study the effect of twisting on the domain structure, a new system was designed as shown in Figure 4-34. The wire was fixed at each end by using chucks with a twisting mount placed at one end of the wire. The system used a Neoark BH-780-IP polarising microscope. Images were taken on 20 mm length AF10 and AC20 amorphous wires at 50 times magnification enabling high resolution images (lens resolution 1 μm) as shown in Figure 4-35 and Figure 4-36. The dark and light contrast in Figure 4-35 represents the radial domain structure in positive magnetostrictive amorphous wires.

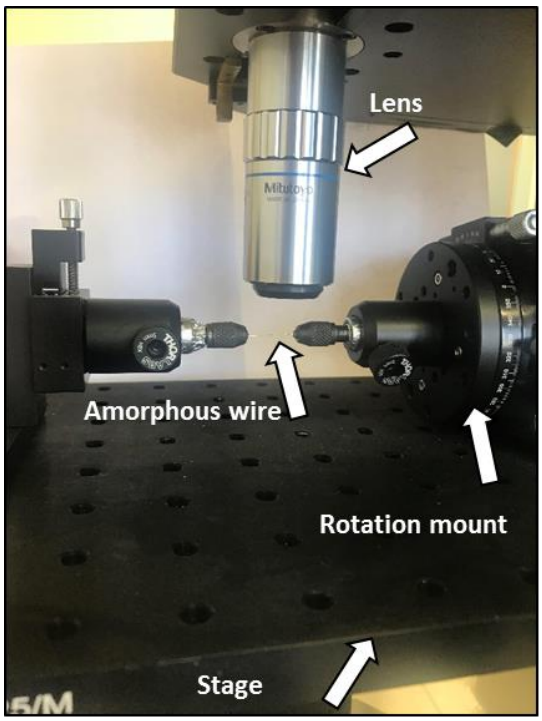

Figure 4-34: Designed twisting system under the microscope for Kerr microscopy

Figure 4-35-a shows a schematic view of domain images by Kerr microscopy. The domain boundary rotates by an angle α relative to the wire axis. The darker contrast indicates a component of magnetisation into the image plane and the lighter contrast out of the image plane. Twisting from 0 to ∏/2 rad (corresponding to 0 to ∏/4 rad/cm) in AF10 shifted the domain wall boundary by 32 μm along the wire as shown in Figure 4-35-b-h. Figure 4-36 shows a vortex domain structure in AC20.

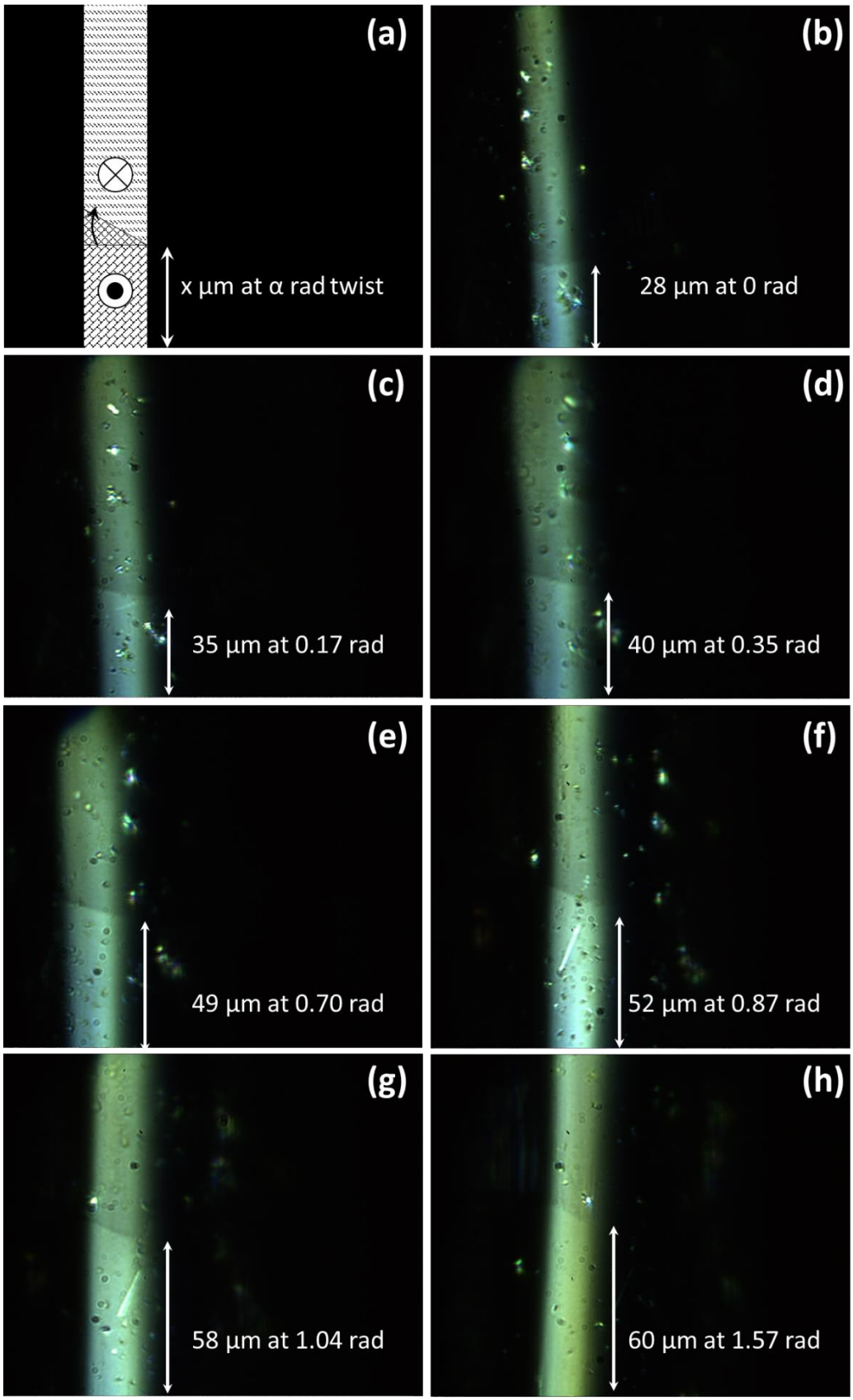

Figure 4-35: The schematic view of the domain boundary with α rad twisting, the boundary rotates by angle α b-h) Longitudinal Kerr microscopy on 20 mm AF10 amorphous wire under different twisting from 0 to ∏/2 rad (corresponding to 0 to ∏/4 rad/cm).

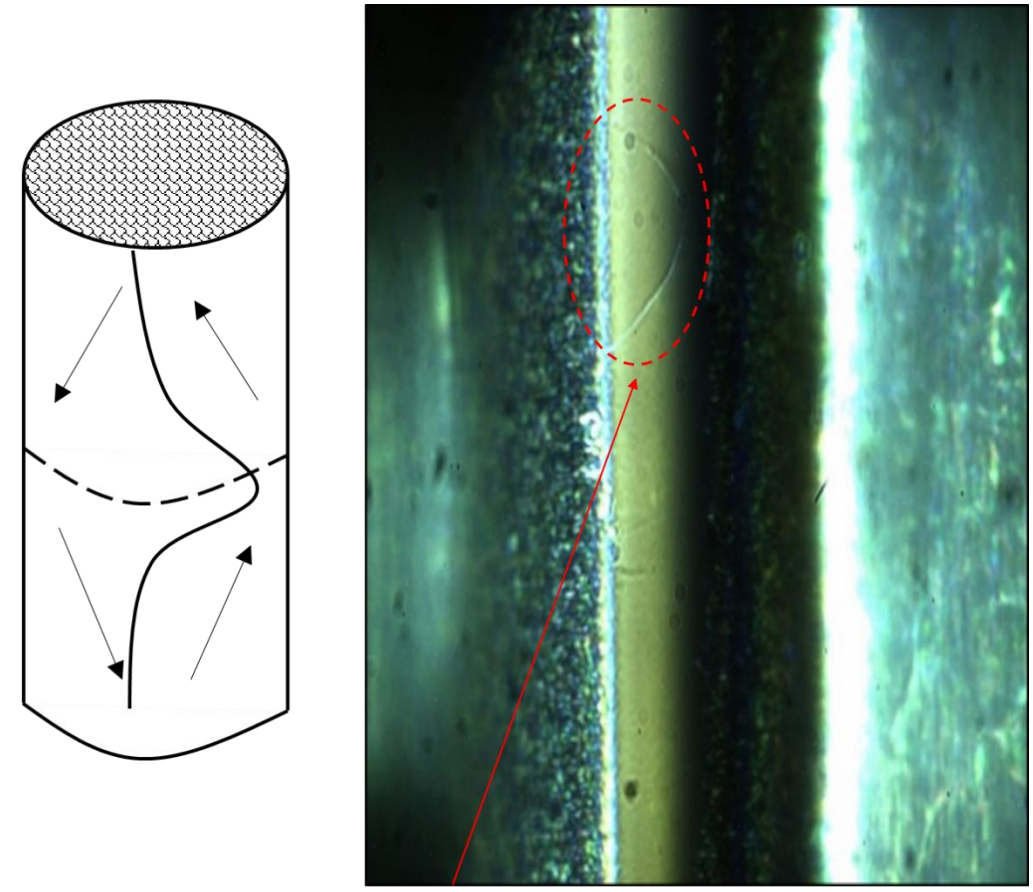

Figure 4-36: Kerr microscopy on 20 mm AC20 amorphous wire

Chizhik et al. [84] also indicate vortex domain images for AC20 amorphous wire. Ideally to see a vortex domain structure, AC20 amorphous wire should be magnetised in the axial direction however, it was still possible to image such a domain without magnetisation as shown in Figure 4-37-b. A schematic diagram for the domain structure is shown in Figure 4-36-a. The domains are pointing in a circular direction around the vortex area. The change of magneto-optical contrast is observed in some areas which are attributed to the rotation of magnetisation. Another reason for the vortex structure could be the shape anisotropy of the wire. The non-planar nature of the sample can cause the formation of magnetisation fluctuations of the vortex type [158]. We were not able to see bamboo like domains as the wire should be magnetised in a circular direction to be able to see this structure.

4.12 Annealing amorphous wires

To eliminate induced stresses during wire fabrication, annealing was done on AF10. The 114 mm long AF10 amorphous wire was annealed for 1 min by passing a 0.5 A DC current and twisting the wire ∏ rad. Therefore, three types AF10 amorphous wires as-cast, annealed and twisted annealed were studied. The current was limited to less than 0.5 A to avoid crystallisation. Annealing and twisting induce an anisotropy in wire after cooling. These parameters were selected based on the work Kane et al. [159] and Gonzalez et al. [160]. The latter used current annealing of 550 mA for 1 min in AF10 to achieve a fully square hysteresis loop shows and complete relaxation of internal stresses. Figure 4-37 and Figure 4-38 show the results of applying tensile and torsion stress respectively on wires magnetised at a field amplitude of 1.49 kA/m and 1 kHz frequency. Results in Figure 4-37 show that annealing has little impact on the Matteucci voltage when the tensile stress exceeds around 50 MPa although the annealed wire (without twisting) does have slightly higher Matteucci values. The most striking difference are the significantly higher Matteucci voltages at zero tensile stress for both annealed wires. This may be due to the elimination of manufacturing residue stresses. Figure 4-39 shows with the application of a 55 MPa tensile stress, the Matteucci voltages in the 0 to 3.49 rad range are not significantly affecting by annealing.

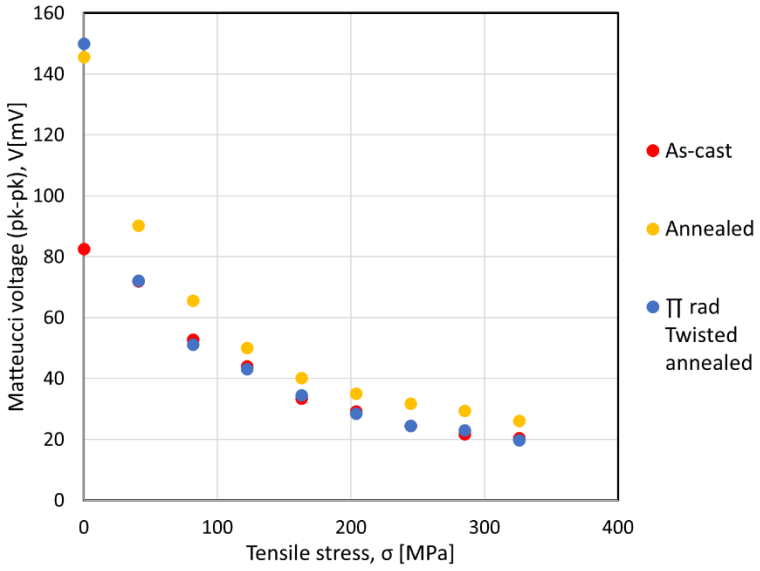

Figure 4-37: Matteucci voltage as a function of tensile stress on 114 mm annealed and as-cast AF10 amorphous wires which are magnetised in 1.49 kA/m magnetic field and 1 kHz frequency and twisted 0.08 rad/cm (29.57 MPa torsion stress).

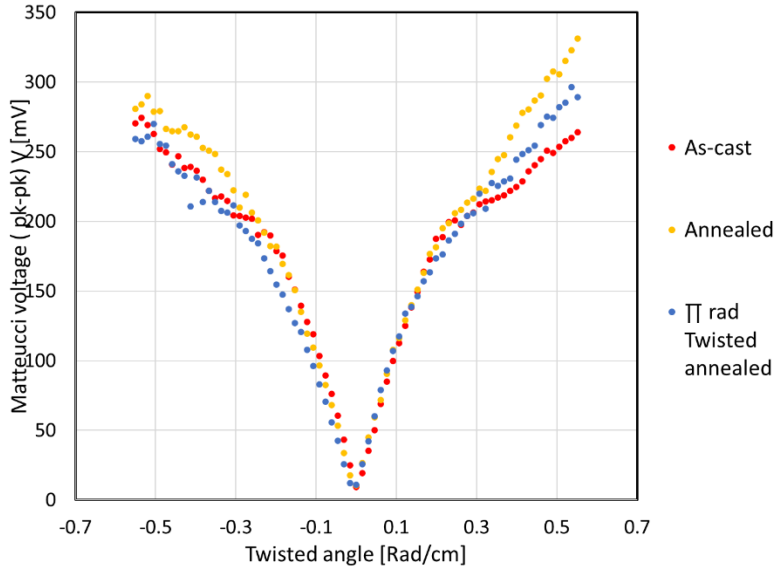

Figure 4-38: Matteucci voltage as a function of torsion stress on 114 mm annealed and as-cast AF10 amorphous wires which are magnetised in 1.49 kA/m magnetic field and 1 kHz frequency by applying 55 MPa tensile stress.

4.13 Summary

To summarise, a new system has been designed to characterise amorphous wires and it has been demonstrated that:

1. The Matteucci effect in amorphous wire is very sensitive to both axial and torsional applied stresses.
2. The near-zero magnetostrictive wire surprisingly produces a Matteucci output comparable to that found in the highly magnetostrictive alloy, and with much better sensitivity at 2 kHz frequencies compare to other frequencies. In this respect, AC20 shows greater potential as a candidate for strain sensing.
3. The Matteucci voltage increases as the length of the wire increases.
4. The Matteucci voltage increases with tensile stress in AC20 amorphous wires but decreases in AF10 amorphous wires.
5. Annealing increased the Matteucci voltage at small tensile stresses, but values converged at larger stresses.
6. Domain imaging by the Bitter technique shows zigzag domain structure in AF10 amorphous wires. By twisting the wire from 0 to 2∏ rad (corresponding to 0 to 2∏/5 rad/cm) a transition from a circumferential zigzag pattern to an arrangement of regularly spaced parallel domain walls occurs.

7. Domain imaging by Kerr microscopy shows movement of a domain boundary in response to twisting from 0 to ∏/2 rad (corresponding to 0 to ∏/4 rad/cm) in AF10 amorphous wire. A vortex domain structure was observed in AC20 amorphous wire.
8. AF10 and AC20 produced an equivalent gauge factor over two orders of magnitude greater than that obtained in a conventional resistive strain gauge, show they are good candidates for strain sensors.
9. The sensitivity of the Matteucci voltage due to tensile stress was also demonstrated in shorter wires of length 45 mm making them possible candidates for wearable sensor applications.

5 Development of a strain sensor and a flexible bend sensor by utilising the Matteucci effect in amorphous wires

5.1 Introduction

According to the findings in the chapter 4, the Matteucci voltage in both positive and slightly negative magnetostrictive amorphous wires changes with tensile stress leading to the prospect of strain sensors with high gauge factors. Sensors exploiting the Matteucci effect on amorphous wires have these advantages:

1. The Matteucci effect is high in amorphous wires compare to amorphous ribbon or other ferromagnetic materials as they are more sensitive to applied stress [10].
2. The Matteucci effect is sensitive to the H-field amplitude and frequency, wire dimensions, tensile stress, torsion and bending stresses. Therefore, the tensile and bending sensitivity can be fine-tuned by setting the torsion, H-field or other wire parameters.
3. There is no need to use a pick-up coil for measuring the Matteucci voltage.
4. Geometrically, amorphous wires have an advantageous shape with a circular cross-section and smooth surface which makes it suitable to wind a coil directly on the wire [59].

Three novel sensors based on the Matteucci effect were developed in this work, one measuring strain and two flexible strain and bending sensors. Strain gauges developed in this thesis have significantly greater gauge factors compared to conventional strain gauges and other strain sensors. The two types of flexible sensors were designed, one using a planar coil and the other using a flexible solenoid to excite the amorphous wire. Finite element modelling was also used in the initial design work of the planar coil. Linearity and repeatability of each sensor were investigated and are discussed.

5.2 Strain sensor design consideration

125 µm thick $Fe_{77.5}Si_{7.5}B_{15}$ (AF10) and $Co_{68.15}Fe_{4.35}Si_{12.5}B_{15}$ (AC20) amorphous wires were investigated in this work. A schematic diagram for the proposed strain sensor is shown in Figure 5-1-a and the measurement system is shown in Figure 5-1-b. It comprises of a solenoid to excite the amorphous wire with a sinusoidal magnetic peak field of 1.49 kA/m and a LCMFL-20N load cell to monitor the applied tensile load on the wire. Fine tuning of the axial stress was made possible with precise movement (10 µm) of the translation stage attached to one end of the wire. The rotation mount enabled precise control of applied torsion with a precision of 0.002 rad (one arc per minute). All experiments were performed on 20 mm length amorphous wire to assess sensor performance. The magnetic field was determined from the magnetising current by measuring the voltage V_H across a 0.47 Ω shunt resistor connected in series with the magnetising winding as shown in Figure 5-1. The value of the magnetic field H was calculated assuming a long solenoid as described in Eq.(4-1).

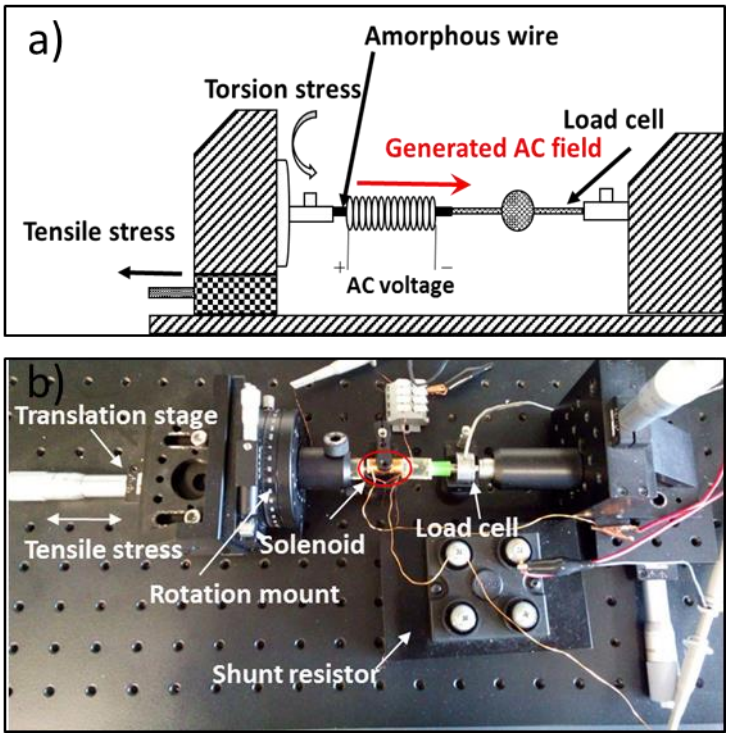

Figure 5-1: a) Schematic diagram of strain sensor b) 20 mm experimental rig

5.3 Results of the strain sensor

The variation of peak-to-peak (pk-pk) Matteucci voltage with tensile stress for 20 mm lengths of AF10 and AC20 amorphous wire are shown in Figure 5-2. The magnetising frequency of 2 kHz was chosen as according to Figure 4-18, 2 kHz has the highest EGF in AC20 amorphous wire. Moreover, wires were subjected to a twist angle of 0.43 rad/cm (168 MPa torsion stress). The Matteucci voltage decreases in AF10 amorphous wire by increasing tensile stress while increasing in AC20 amorphous wire due to the different domain structure in both wires.

To evaluate amorphous wire as a potential candidate for strain sensing, an equivalent strain gauge factor (EGF) for AF10 and AC20 amorphous wires was calculated as described in Eq.(4-10), in four different regions named 1-4 as shown in Figure 5-2. By achieving high gauge factors for amorphous wires in chapter 4, sensors with smaller lengths were investigated for use as potential wearable sensors. To measure the uncertainty in the equivalent gauge factor, summation in quadrature was used to combine the individual uncertainty contributions as in Eq.(5-1).

$$R = {}^{\frac{x}{y}}\Big/_{z} \rightarrow \frac{u(R)}{R} = \sqrt{(\frac{u(x)}{x})^2 + (\frac{u(y)}{y})^2 + (\frac{u(z)}{z})^2} \quad (5\text{-}1)$$

Where u(R)/R is the relative uncertainty in R and u(x)/x, u(y)/y and u(z)/z are the relative uncertainties in x, y and z respectively [152].

The relative uncertainty for EGF is calculated from Eq.(5-2) and shown in **Table 5-1**.

$$\frac{u(EGF)}{EGF} = \sqrt{(\frac{u(\Delta V)}{\Delta V})^2 + (\frac{u(V_0)}{V_0})^2 + (\frac{u(\sigma)}{\sigma})^2} \quad (5\text{-}2)$$

Where u(EGF)/EGF is the relative uncertainty in EGF and $u(\Delta V)/\Delta V$, $u(V_0)/V_0$ and $u(\sigma)/(\sigma)$ are the relative uncertainties in difference between voltages of different strain measurements, initial voltage and strain gauge resolution (0.005 N) respectively.

The good linearity seen in Figure 5-2 for AC20 (R^2 = 0.99) enabled the fitting of a trendline to determine the gauge factor which was equal to 601 ± 30 taken over the whole stress range. In the case of AF10, individual EGF's were calculated for different stress regions (1-4) due to the non-linear decrease in Matteucci voltage with stress. EGF varied from 806 to 72 as shown in Table 5-1 demonstrating

excellent performance at lower tensile stress but becoming progressively less sensitive with increasing tensile stress.

In summary, over the stress range investigated (0 - 326 MPa), AF10 produced the highest gauge factor but this was limited to low tensile stresses. In contrast AC20 produced consistent EGF's over the whole stress range with values only around 34 % smaller than AF10's maximum EGF value of 806.

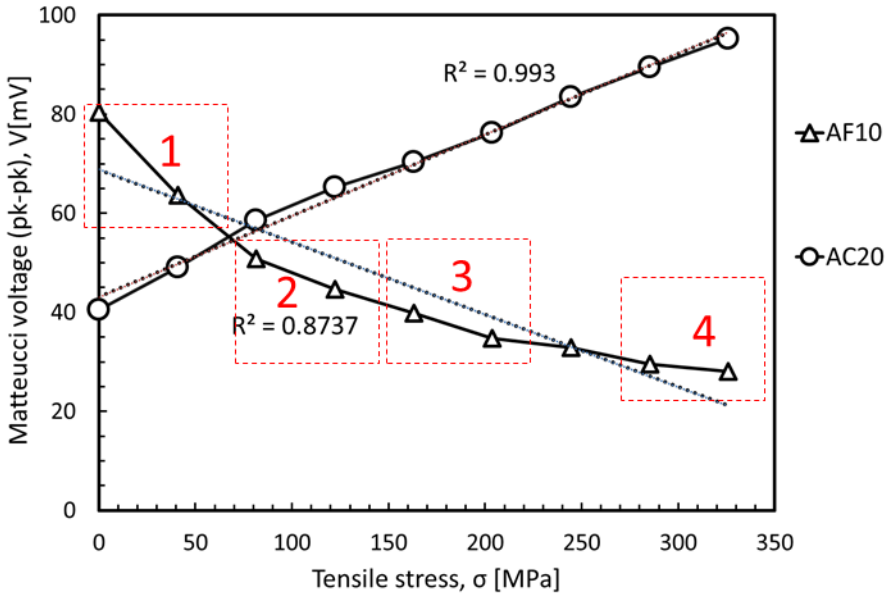

Figure 5-2: Variation of peak-to-peak Matteucci voltage as a function of tensile stress in 20 mm long AC-20 and AF10 Amorphous wires which were twisted 0.43 rad/cm (168 MPa torsion stress) and magnetised at 1.49 kA/m, 2 kHz.

Table 5-1: Gauge factor determination

Amorphous wire	Position	$\frac{\Delta V_m}{V_m}$	$\Delta\sigma$ (MPa)	EGF	Uncertainty of EGF
AF10	1	0.20	40.74	806	78
AF10	2	0.07	40.74	296	32
AF10	3	0.06	40.74	248	53
AF10	4	0.02	40.74	72	114
AC20		0.15	40.74	601	30

The viability of amorphous wire to function as a strain sensing device was investigated.

It is demonstrated that the Matteucci effect in AF10 and AC20 amorphous wires is very sensitive to both axial and torsional applied stresses. The Matteucci voltage generated in near-zero magnetostrictive wire is comparable to that found in the highly magnetostrictive alloy and is more linear as a function of tensile stress.

The highest gauge factor is 806 $\pm$ 78 for the sensor with AF10 amorphous wire. This is an excellent result compared to the much smaller gauge factors of other sensing types referenced in Table 5-2. Ink-based resistive strain sensors and Carbone nanotube-based strain sensors change nonlinearly with strain while the proposed AC20 and AF10 amorphous wire sensors have a linearity (R^2) of 0.99 and 0.89 respectively. Repeatability of the sensor was evaluated using the SD and was a minimum of 0.08 mV for the AF10 strain sensor and 0.15 mV for the AC20 strain sensor. Equivalent values were not available for the other sensors. The strain range calculated for the proposed wire sensors was 0.25 % in this work which is not the maximum capacity of the sensor. For the other sensors [161]- [130], values differ from 50 % to 750 % which shows the stretchability of the sensors, however they are not linear in these ranges.

Table 5-2: Strain sensor's comparison

Sensor	Linearity	Sensitivity (GF)	Strain range
*AF10 strain sensor	0.87	806	0.25 % strain
**AC20 strain sensor	0.99	601	0.25 % strain
Ink-based resistive strain sensor [161]	nonlinear	3.8±0.6	400 % strain single axis
Carbone nanotube based strain sensor [110]	nonlinear	0.82 for (Strain<40 %) 0.06 for (Strain> 60 %)	280 % strain single axis
AgNP based stretchable strain sensor [162]	linear	2.05	-
Conventional metal foil strain sensor [115], [125], [12]	-	~2	100 % strain
Wireless strain sensors fabricated from amorphous carbon [13]	Linear	0.534	51% strain
Single-walled CNT [128]	-	<1	400 %
super- aligned (CNT films) [129]	-	<1	450 %
wrinkled (CNTs) [130]	-	0.65	750 %

Note: '-'means the literature did not report the corresponding performance index.

5.4 Flexible strain sensor based on PCB printed planar coil

In this work, the main objective was to produce a flexible sensor, capable of measuring strain and bending. To excite the amorphous wire several planar coil geometries were modelled in ANSYS Maxwell FEM (Finite Element Method) software. And then fabricated as flexible printed circuit boards (PCB). The PCB consisted of a non-conductive flexible polyester substrate laminated between two layers of patterned copper.

5.4.1 FEM theory

The concept of FEM was first proposed in the field of structural mechanics in 1956 due to the emergence of computers [163]. Today finite element method has become one of the most frequently used methods to solve engineering equations. This method requires intensive use of computers and can be used to solve a problem in one, two or three dimensions. The finite element method consists of using simple approximations of unknown variables to transform partial differential equations into algebraic expressions.

Making algebraic equations for the entire domain of a structure is extremely difficult, so the structure is divided into a number of small elements. These elements are connected to nodes. By putting all the element equations together and solving them, the unknown variables at nodes can be obtained explicitly. The field quantity is then interpolated by a polynomial over an element at non-nodal points.

5.4.1.1 Geometry

The geometry of the design was drawn in ANSYS in 3D as shown in Figure 5-3. All the parameters which are defined in the model are listed in Table 5-3. Two identical 46 turn copper spirals with track width equal to 0.125 mm, track separation equal to 0.125 mm and thickness equal to 0.3 mm was modelled. The two spiral coils were positioned overlapping with a separation of 0.125 mm equal to the diameter of the amorphous wire. Furthermore, the magnetic isolation boundary condition specifies the magnetic field to be contained within the model thus the normal component of the flux on the boundary is zero. An initial value applied to the outer boundary of

the model and contained magnetic vector potential was set to zero. The size of this simulation volume was 27×25×5.95 mm.

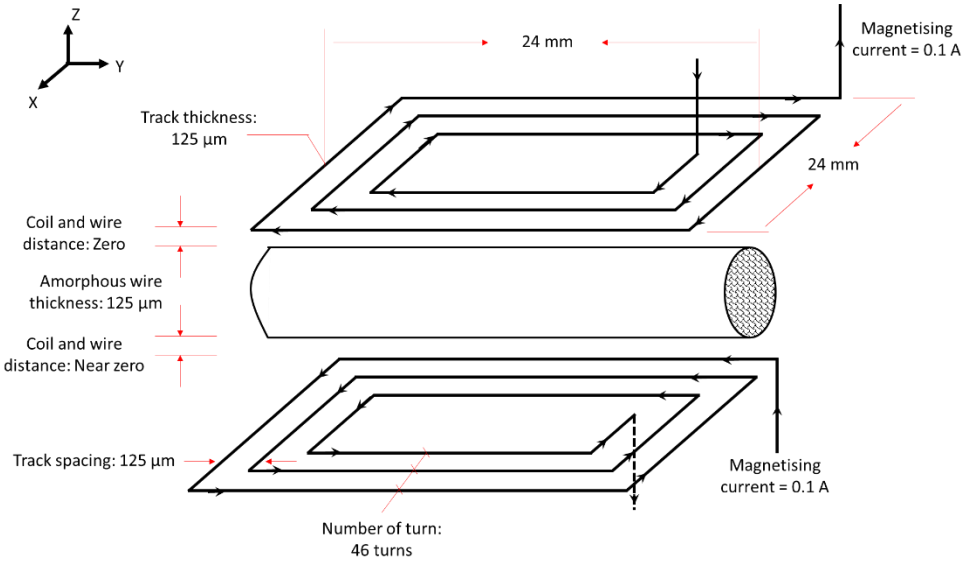

Figure 5-3: Planar coils schematic design – Not to scale

Table 5-3: The ANSYS model parameters

Parameter name	Value (mm)
Distance between turns	0.125
Width of spiral	0.125
Thickness/height of the spiral	0.03
Number of turns	46
Volume of simulation	27×25×5.95

5.4.1.2 Meshing and solving

Meshing is the process used to divide the physical domain into a set of simple geometric elements which are usually triangular or quadrilateral for 2D and pyramid for 3D. The finite element method approximates the solution within each element by minimizing an associated error function. Meshing a geometry is an essential part of the simulation process and is crucial for obtaining the best results in the fastest manner. If the mesh size is too coarse, then the solution would quickly converge (if converges) with a big error and if the mesh is too fine the computation time will be too long and may never converge in a reasonable time. As a rule of thumb, the minimum mesh size should be smaller than one third of the smallest area/corner in the geometry which is to be solved. For the geometry shown in Figure 5-3, the minimum dimension of the region for which a solution was obtained was 125 µm.

Therefore, maximum mesh size of 40 µm can be used however the minimum mesh size of the model was set to 100 nm. The typical solving time of this design was around 45 min using a computer with core i7 processor and 16 GB RAM. The current of 8.1 X 10^6 A/m^2 was applied in the x-direction as shown in Figure 5-3. Simulation results show that a magnetic field of 400 A/m along the Y direction was generated at the centre of the two coils. Figure 5-4 shows, the generated magnetic field in the Y direction from Y=0 the start of the coil, to 24 mm the edge of the coil.

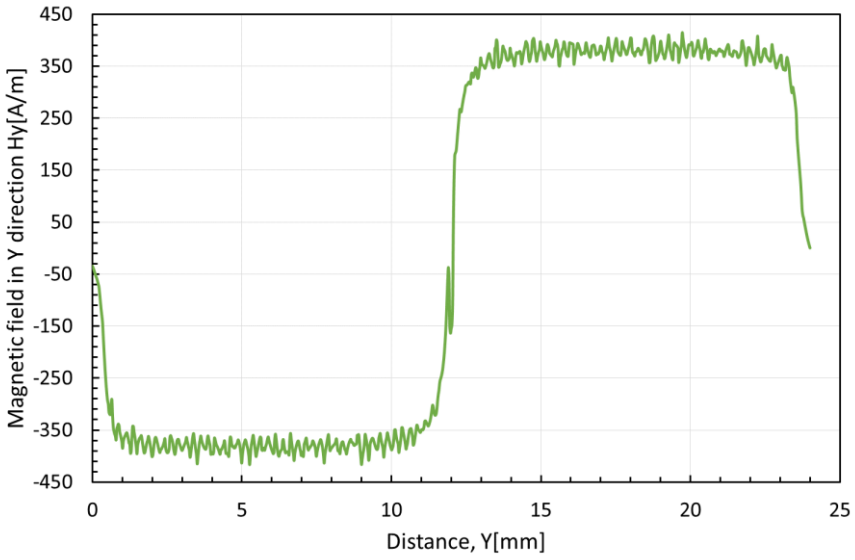

Figure 5-4: Magnetic field produced between two square coils modelled in ANSYS.

5.4.2 PCB Planar coil

The final design for single planar coil, shown in Figure 5-6, generates a field component parallel to the coil plane equal to 200 A/m at a distance of 62.5 µm using a 0.1 A current which was chosen to limit coil heating. A square coil was chosen as it generates a uniform field in the Y direction. As Figure 5-6-b shows, the square coil contains 46 turns with a track width of 0.125 mm and a spacing of 0.125 mm. According to Ampere's law Eq. (4-1), passing a current through the planar coil generates a magnetic field around each track. The resultant magnetic field in the Y direction parallel and close to the coil surface would be uniform as shown in Figure 5-5. This uniform magnetic field is a superposition of the smaller magnetic fields generated by each track. A similar magnetic field is generated in the X direction but in this case has little impact since the wire element was aligned along the Y direction.

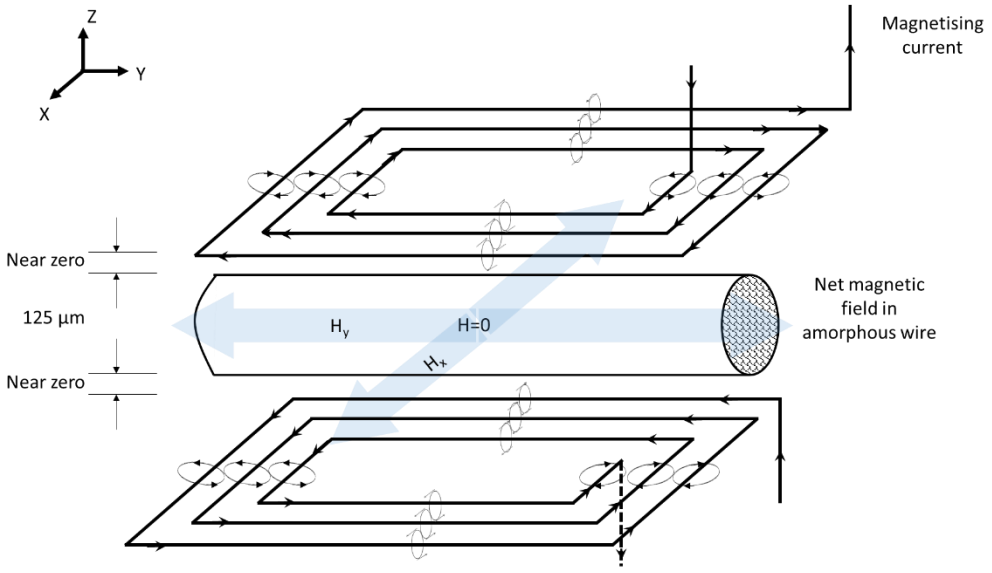

Figure 5-5: The magnetic field distribution in between the two planar coils

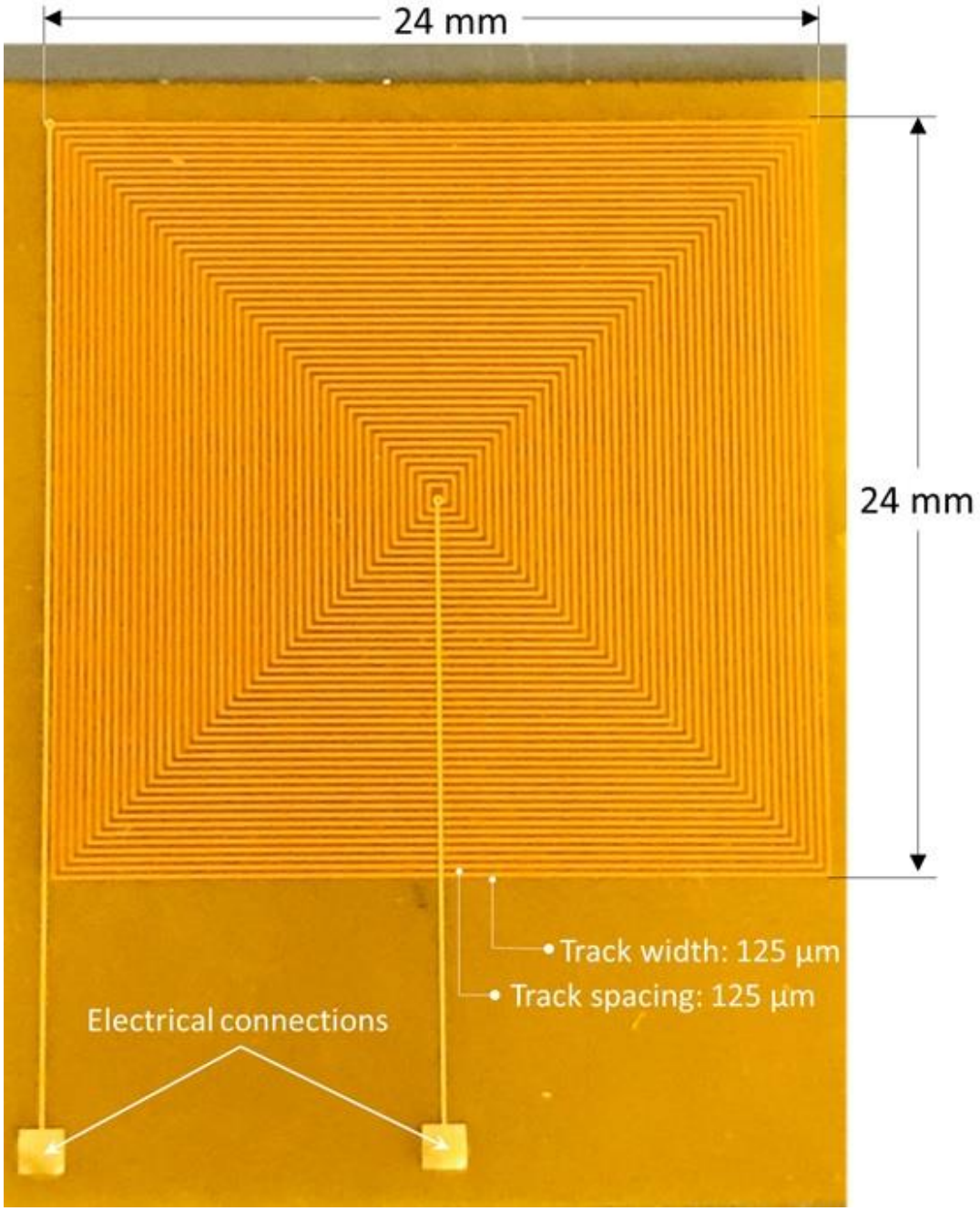

Figure 5-6: 24×24×0.13 mm, 46 turn planar printed coil on a flexible PCB substrate with 0.125 mm track size and 0.125 mm track spacing.

5.4.3 Flexible strain sensor

AF10 amorphous wire was used in this sensor as it has bigger Matteucci voltage output compare to AC20 and high gauge factor. According to Figure 4-17, AF10 amorphous wire has the highest gauge factor for 100 Hz however the Matteucci voltage is small at this frequency. To provide a large Matteucci voltage, 500Hz was

selected as the operating frequency whilst maintaining a respectable gauge factor of 70 % of the highest value. The schematic diagram of the sensor and the experimental set-up are shown in Figure 5-7-a,b respectively. The sensing element comprised of a 45 mm long 125 µm diameter wire. Two planar coils were positioned under and above the wire with a 125 µm separation equal to the wire diameter. The planar coils were fabricated on to a flexible polyester film made by Quick-tech Ltd. To increase the field, the wire was sandwiched between two planar coils used to excite the wire with a total sinusoidal magnetic field of amplitude 400 A/m. A LCMFL-20N load cell, with a nominal capacity of 20 N, monitored the tensile load applied to the wire. And a rotation mount was placed to twist the wire to the desired value which was 0.70 rad/cm (271 MPa torsion stress).

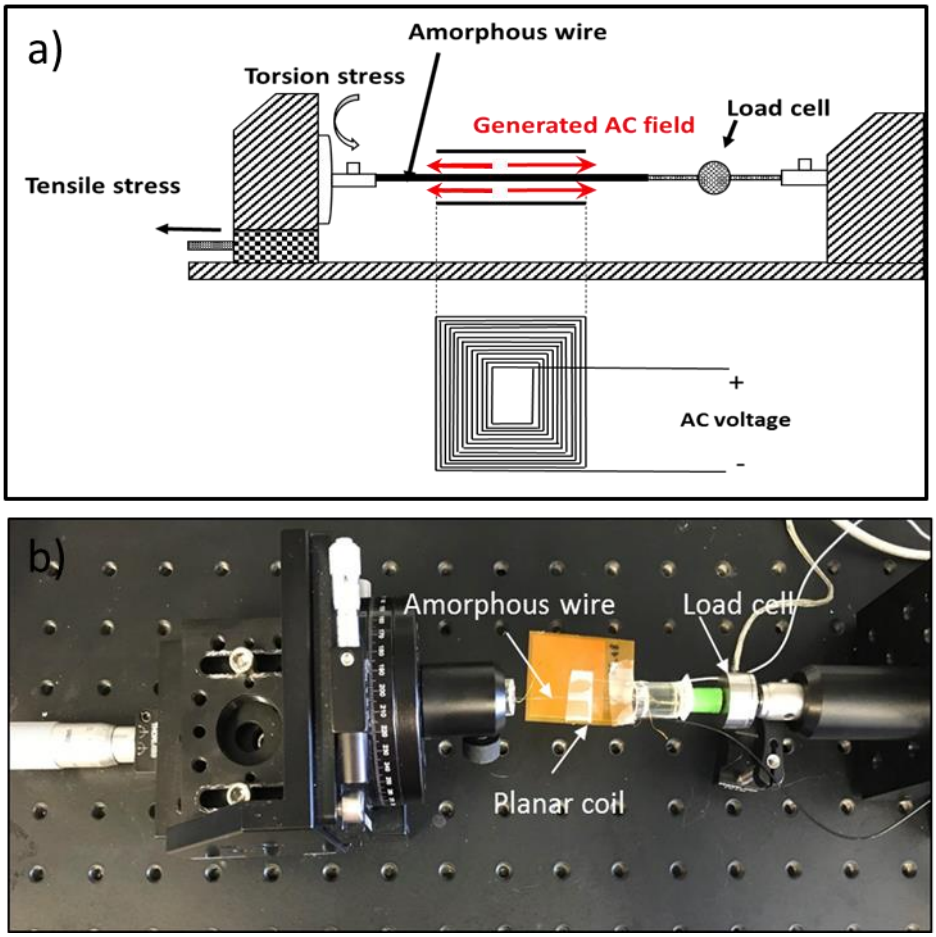

Figure 5-7: a) Schematic diagram of the sensor. Note: The wire was tightly sandwiched between the two coils. The diagram's components are not drawn to scale. b) Experimental set-up; 45 mm long sensor

5.5 Results of the proposed strain sensor

A 45 mm long positively magnetostrictive $Fe_{77.5}Si_{7.5}B_{15}$ (AF10) wire was energised by two planar coils generating an alternating magnetic field. The peak output Matteucci voltage shown in Figure 5-8, was only 1 mV. This low voltage occurs because the magnetic fields produced by each planar coil (see Figure 5-4) are opposing and therefore cancelling each other out. Since a well-defined Matteucci voltage does appear, albeit small, this indicates an asymmetry exists within this particular sensor. Figure 5-9 demonstrates the stress sensitivity of this sensor. Using the relative change in Matteucci voltage divided by the strain in the wire an equivalent gauge factor of 767 was calculated. This demonstrates the feasibility of this approach. Dimitropoulos et al. developed a micro-fluxgate sensor using a similar approach with $Fe_{77.5}Si_{7.5}B_{15}$ amorphous wire and a planar coil [60]. In his design, the amorphous wire was soldered across half of the square coil to achieve magnetisation in one direction. Extending the work described in this thesis in a similar fashion, should improve the Matteucci output level significantly.

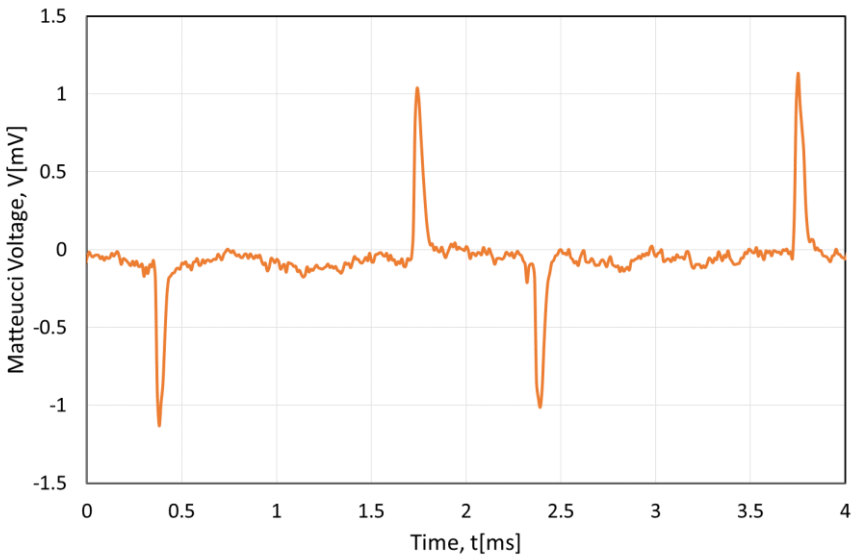

Figure 5-8: Output Matteucci voltage on 45 mm AF10 amorphous wire, magnetised with 400 A/m at 500 Hz frequency , 150 MPa tensile stress, twisted 0.70 rad/cm (271 MPa torsion stress).

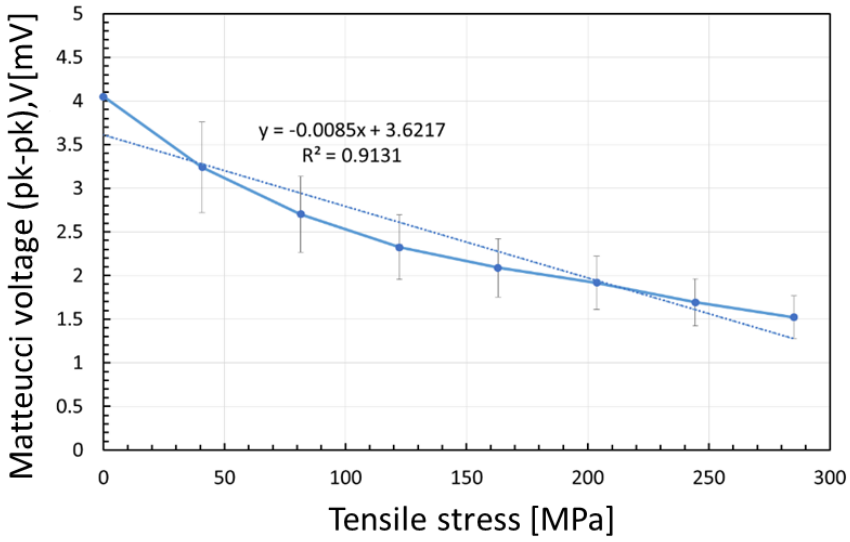

Figure 5-9: Variation of Matteucci voltage by applying tensile stress on $Fe_{77.5}Si_{7.5}B_{15}$ amorphous wire, Twisting: 0.70 rad/cm (271 MPa torsion stress), Magnetic field: 400 A/m, Frequency: 500 Hz, Length: 45 mm.

In conclusion, a simple strain sensor has been developed which is light (0.9 g) and has high strain sensitivity equivalent to a gauge factor of 767. There is scope to develop the sensor further by utilising the field from only half of the planar coil's geometry. Also, the integration of a pre-torsioned wire and planar coil into a self-contained package is still to be realised.

5.6 Bending sensor

Bending is the combination of compression and tensile stress as it can be seen in Figure 5-10. If the force pulls the member (tension) it results in a tensile stress and if the force pushes the member (compression) it results in compressive stress. By far, the bending stress effect in GMI amorphous wires is actually less known. Nevertheless, the investigation of this effect is particularly important in applications such as current sensors [6]. We do this study to see the effect of bending on Matteucci effect on amorphous wires.

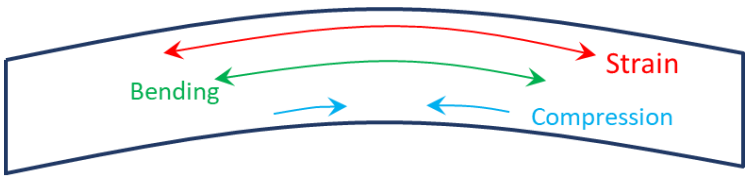

Figure 5-10: Bending stress distribution

5.6.1 Flexible bending Sensor design considerations

The output Matteucci voltage in the proposed sensor in the previous section was small and overheating occurs for currents more than 0.1 A. Therefore, another sensor design was investigated using a flexible solenoid and $Fe_{77.5}Si_{7.5}B_{15}$ amorphous wire. As the schematic diagram of the sensor shows in Figure 5-11, the sensing element consisted of a 45 mm long, 125 μm thick amorphous wire. The amorphous wire was placed inside a flexible tube 0.3 mm in diameter and 30 mm long. A coil with 200 turns of 0.11 mm diameter wire, formed a solenoid able to excite the amorphous wire with a sinusoidal magnetic field of amplitude 0.9 kA/m by passing 0.135 A current through it. Both ends of the amorphous wire were physically connected to copper measurement leads to pick up the Matteucci voltage. The whole arrangement was embedded inside silicone rubber (Dragon skin 30 from Smooth-on Company).

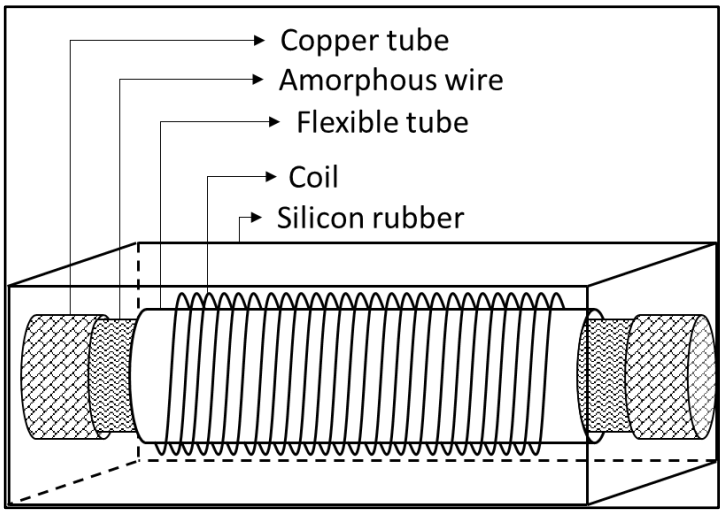

Figure 5-11: Schematic diagram of the bending sensor

Dragon skin 30 was chosen to give enough flexibility for the sensor to bend but also stay stiff enough to support the coil. The wire was twisted 0.70 rad/cm (271 MPa torsion stress) with the rotation mount as shown in Figure 5-13 before allowing the silicone rubber to cure. This angle was chosen because according to Figure 5-12, it gives high enough Matteucci voltage before going to the nonlinear region. The finished dimensions of the sensor were 3 mm height, 5 mm width and 50 mm length. To test the bending sensitivity of the sensor two types of curvature surfaces, A and B, were printed as shown in Figure 5-14. The first curvature surface (A) was used by taping the sensor on to the curved surface to induce bending stress in the sensor. However, the action of the tape also induced tensile stresses. The second type of

surface (B) included a groove to hold the sensor, this avoided the induced fixing stresses seen using A. Curvature measurements were obtained using both types of surfaces. The sensor was installed on different curvature diameters ranging from 40 mm to 90 mm in steps of 5 mm, and the Matteucci voltage was measured. The curvature surfaces were designed in Solid works and printed by a 3D printer as shown in Figure 5-15. There is a groove to place the sensor in, and additional slots for aiding the removal of the sensor and placing the electrical connections. As the sensor was 50 mm long, the curvature surfaces cannot be under 40 mm in size.

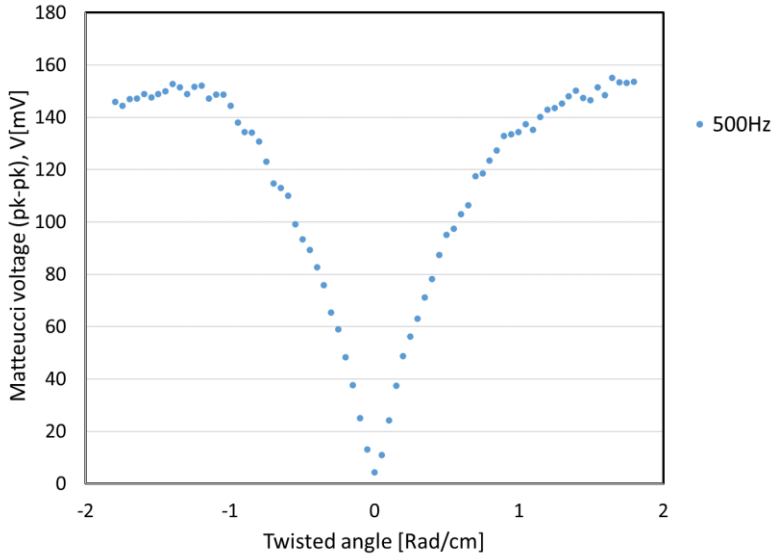

Figure 5-12: Matteucci voltage due to twisting angle on 45 mm length AF10 amorphous wire which is magnetised in 1.49 kA/m magnetic field and 500 Hz frequency by applying 55 MPa tensile stress.

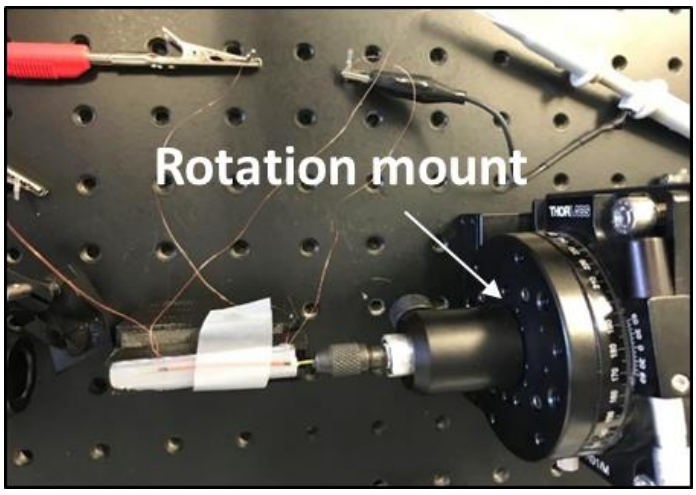

Figure 5-13: Rotation mount for twisting the amorphous wire

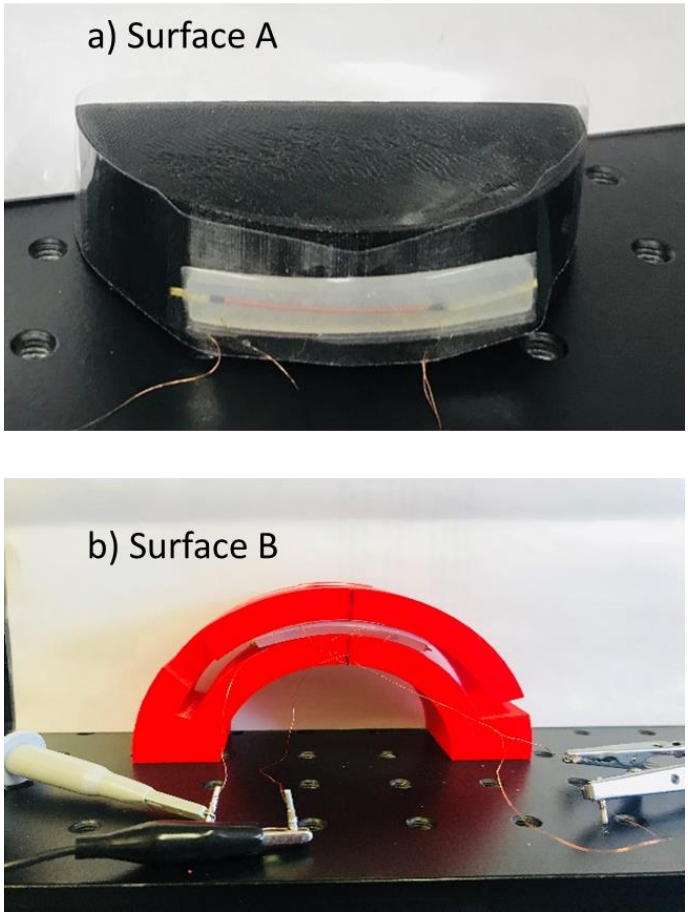

Figure 5-14: Two different curvature surfaces a) A surface and b) B surface.

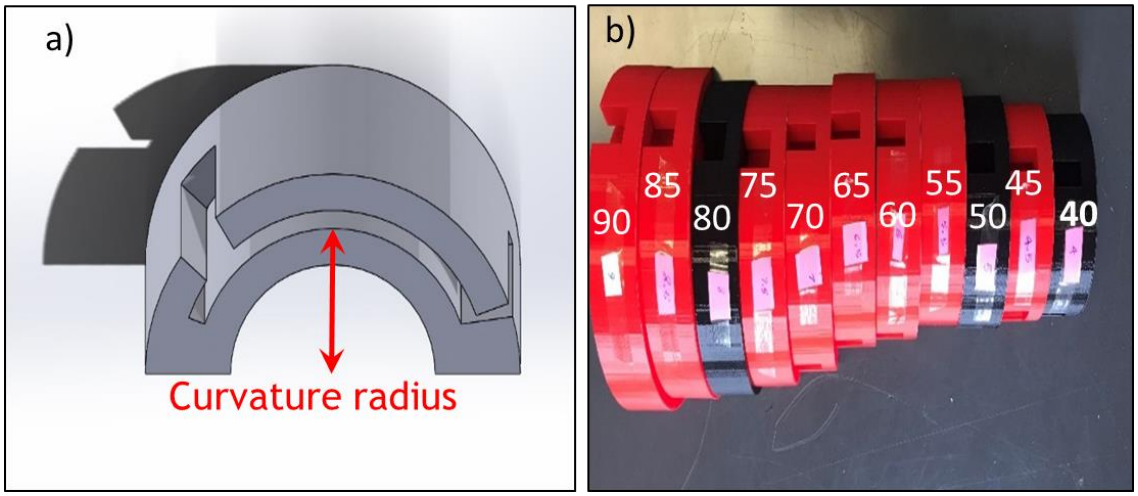

Figure 5-15: a) Solid work design of curvatures b) Printed curvature surfaces designed to test the sensors in sizes varying from 40 mm to 90 mm

5.7 Results and discussion of flexible bending sensor

The output Matteucci voltage shown in Figure 5-16 is 40 mV peak. Experiments were repeated ten times for each curvature and averaged as shown in Figure 5-17. The maximum and minimum uncertainties in the Matteucci voltage were 1.38 mV and 0.31 mV respectively for A surfaces and 0.4 mV and 0.08 mV respectively using the B surfaces. Uncertainty was calculated using Eq.(4-5). Figure 5-17 shows that better linearity was achieved and more than doubling of the sensitivity was measured using the B surfaces.

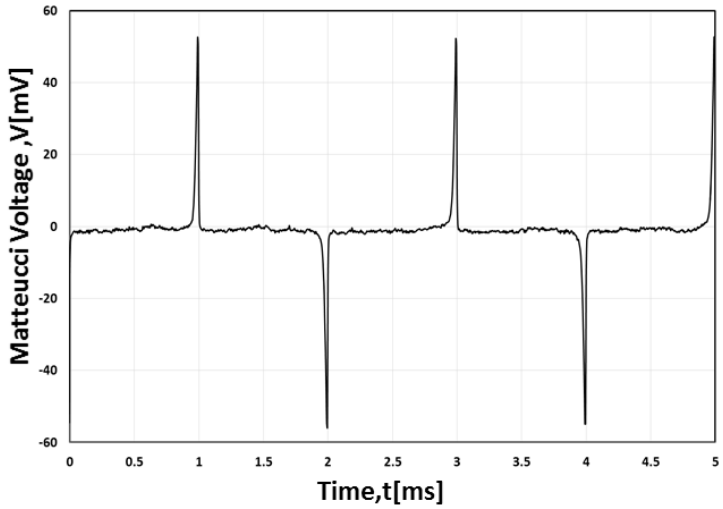

Figure 5-16: Output Matteucci voltage for the sensor magnetised with 0.9 kA/m magnetic field at 500 Hz frequency

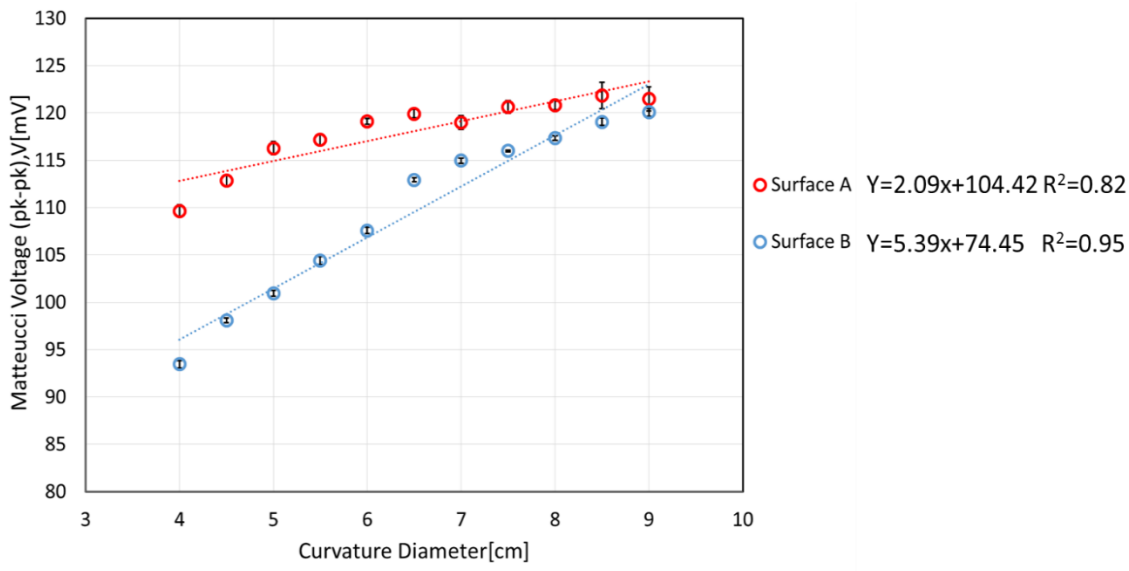

Figure 5-17: The variation of peak to peak Matteucci voltage due to different curving surfaces A and B on 45 mm long, 0.70 rad/cm twisted (271 MPa torsion stress) AF10 amorphous wire magnetised with 0.9 kA/m magnetic field at 500 Hz. Each measurement was conducted 10 times and then the results were averaged.

Four sensors named S1- S4 were fabricated to evaluate the repeatability.

The fabrication process for S1 and S2 involved constructing a 3D printed mould with an internal cavity measuring 3x5x50 mm as shown in Figure 5-18. This enabled embedding the sensor with silicone rubber i.e. dragon skin 30. During the embedding process the amorphous wire and solenoid were placed inside the cavity with the wires protruding through holes at the ends of the mould. Sensors, S1 and S2, were made by using several stages of silicone embedding. First stage involved partially embedding the coil and amorphous wire inside a thin silicone rubber layer. In the next stage, a second mould was used in which the wire/solenoid assembly was inserted. One end of the wire/solenoid was pressed against the mould, the other end was left exposed. The whole assembly was coated with a second layer of silicone thereby fixing the exposed wire end. The final stage was to rotate the uncoated wire end by 0.70 rad/cm as shown in Figure 5-19 whilst simultaneously embedding the whole arrangement in a third coating of silicone.

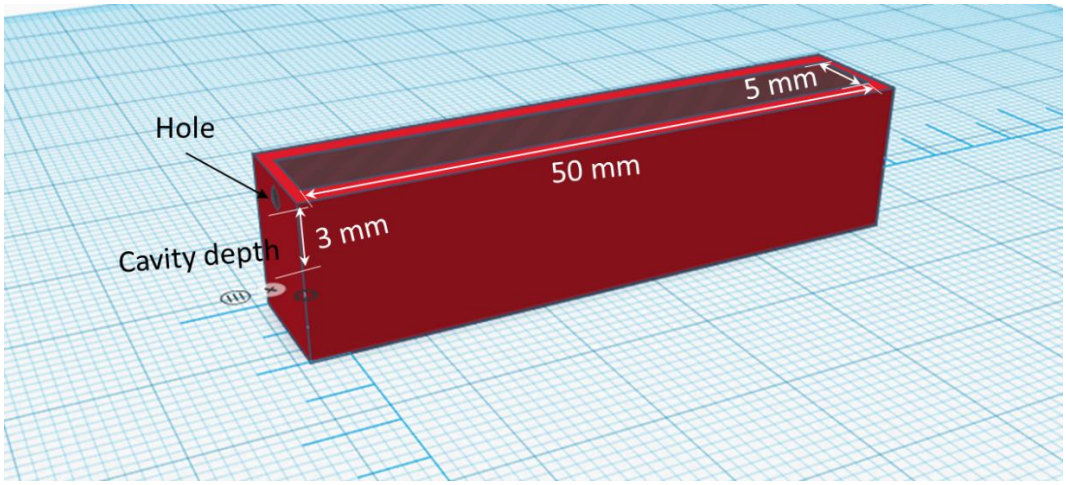

Figure 5-18: The mould to be filled by silicon rubber and making the sensor

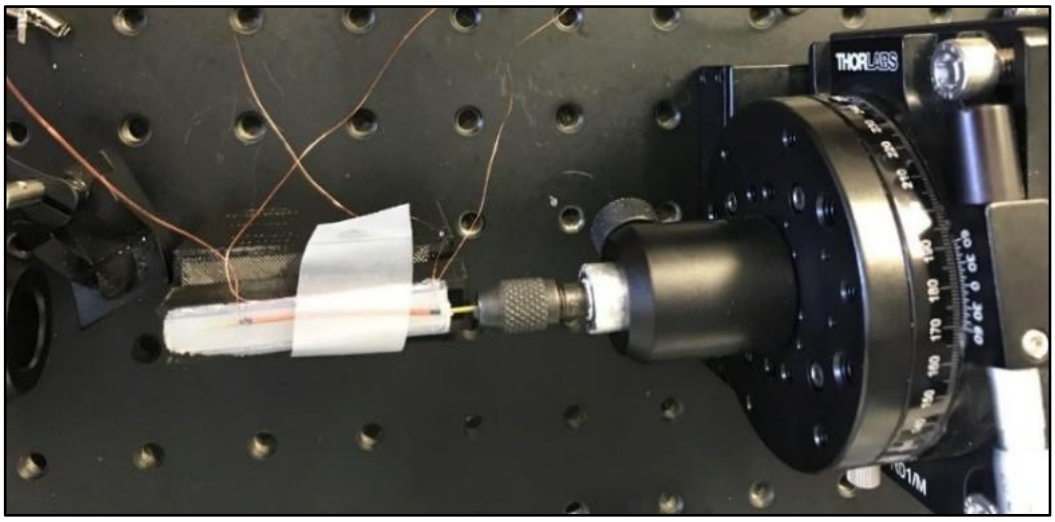

Figure 5-19: Holding amorphous wire from one end, method number one

Experiments were repeated by attaching and removing the sensors to each curved surface ten times. Each set of ten measurements consisted of two groups of five measurements spread over two days to check there were no time dependent changes such as the untwisting of the wires. The results for S1 and S2 are shown in Figure 5-20 and Figure 5-21 respectively. Each point in Figure 5-24 and Figure 5-25 are the average of five measurements. The SD in these measurements (average of

five measurements SD_5) were calculated using Eq.(4-5), for S1 and S2 were 1.29 mV and 0.58 mV respectively.

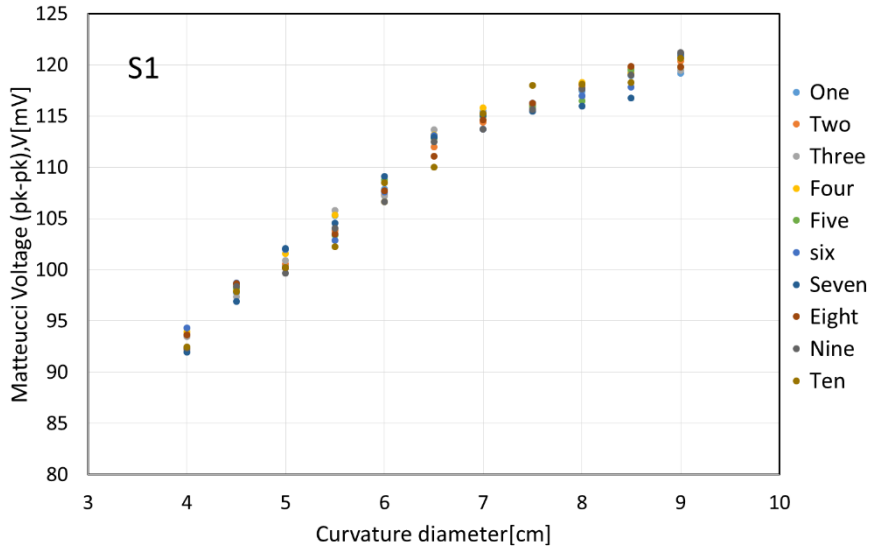

Figure 5-20: S1 -The variation of peak to peak Matteucci voltage due to different curving diameter on 45 mm AF10 amorphous wire magnetised with 0.9 kA/m magnetic field, 500 Hz frequency and twisted 0.70 rad/cm (271 MPa torsion stress)

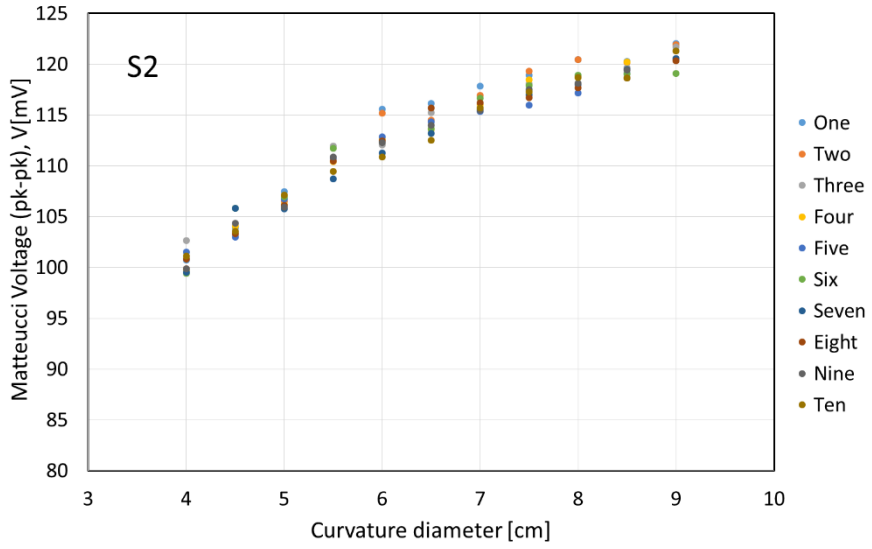

Figure 5-21: S2 -The variation of peak to peak Matteucci voltage due to different curving diameter on 45 mm AF10 amorphous wire magnetised with 0.9 kA/m magnetic field, 500 Hz frequency and twisted 0.70 rad/cm (271 MPa torsion stress)

To make sensors S3 and S4 another method was developed which has improved the uncertainty compare to method one. In this method the ends of the wire were connected to chucks to maintain wire straightness and to exert a twisting of 0.70

rad/cm as shown in Figure 5-16. The mould was filled with silicone rubber and left to solidify for one hour. The fabricated sensors S3 and S4 are shown in Figure 5-23.

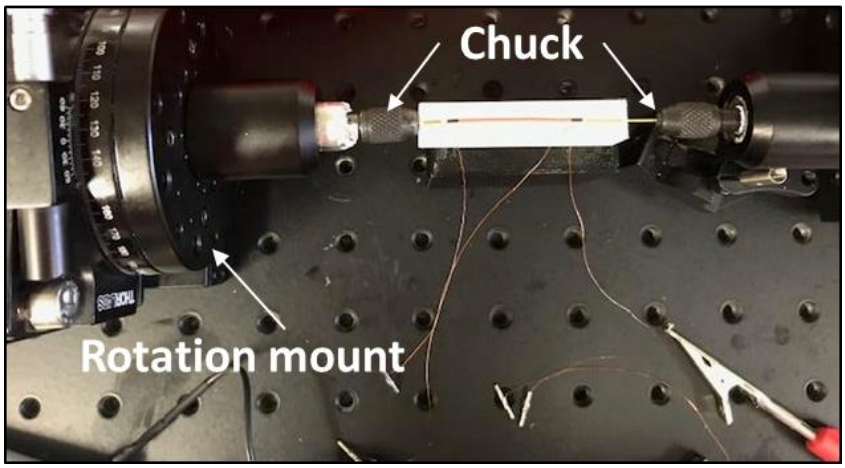

Figure 5-22: Holding amorphous wire from both sides. Method number one

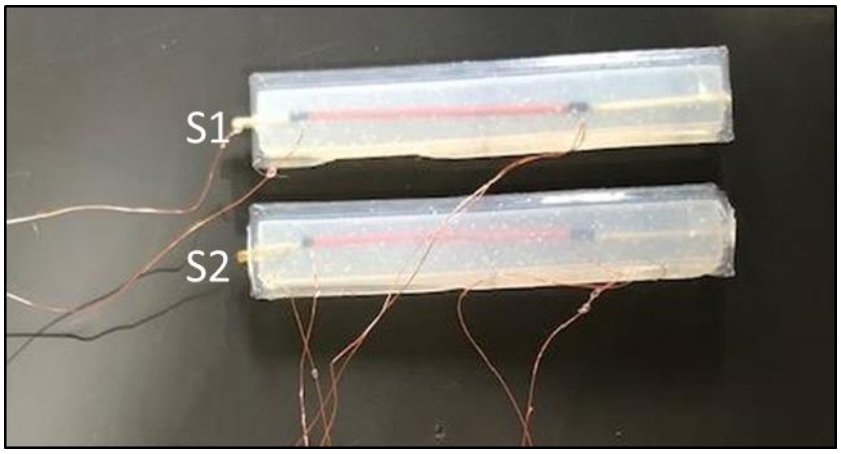

Figure 5-23: 3×5×50 mm sensors with 125 µm diameter, 45 mm length AF10 amorphous wire laid in silicon rubber

The same bending and measurement procedures used for S1 and S2 were repeated for sensors S3 and S4, the results are shown in Figure 5-24 and Figure 5-25. The SD_5 in these measurements (average of 5 measurements in each point) for S3, S4 are 0.63 mV and 0.52 mV respectively.

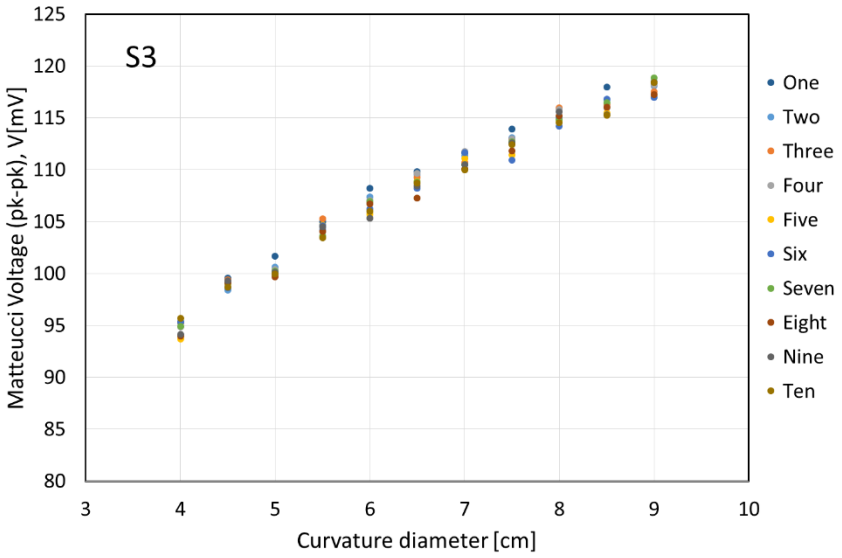

Figure 5-24: S1 - The variation of the peak to peak Matteucci voltage due to different curving diameter on 45 mm long, 0.70 rad/cm twisted (271 MPa torsion stress) AF10 amorphous wire magnetised with 0.9 kA/m magnetic field at 500 Hz.

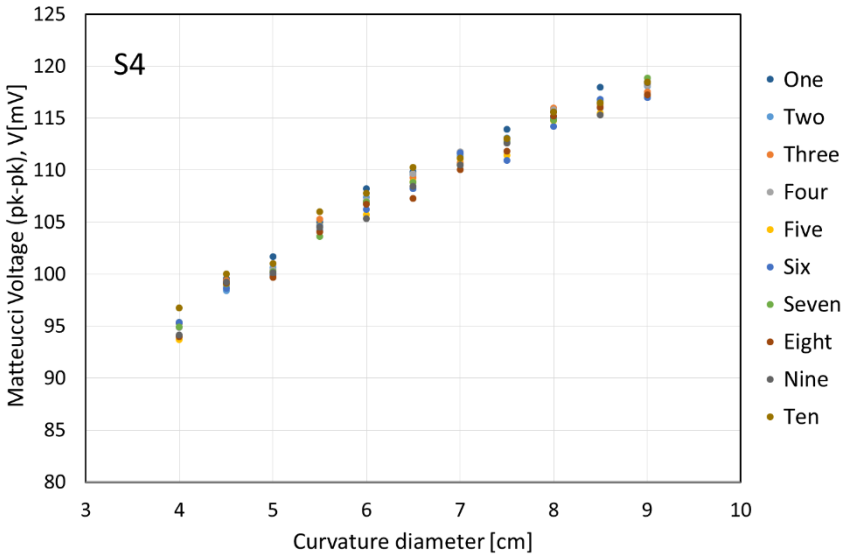

Figure 5-25: S2 - The variation of the peak to peak Matteucci voltage due to different curving diameter on 45 mm long, 0.70 rad/cm twisted AF10 amorphous wire (271 MPa torsion stress) magnetised with 0.9 kA/m magnetic field at 500 Hz.

Figure 5-26 shows a comparison between all four of the sensors after fitting a linear trendline. To measure the sensitivity, the ratio of voltage change is divided by curvature change described in Eq.(5-3) in mV/cm. V1 is the voltage for curvature (C1) and V2 is the measured voltage for curvature C2.

$$\text{Sensitivity} = \frac{V1 - V2}{C1 - C2} \tag{5-3}$$

According to Figure 5-26, S1 and S2 have a sensitivity of 5.45 and 3.95 mV/cm and a linear response to curvature with coefficients of determination equal to 0.95 and 0.94 respectively.

S3 and S4 have a linear response to curvature and coefficients of determination equal to 0.98 and 0.96 and sensitivity of 4.45 mV/cm and 2.79 mV/cm respectively. Discrepancies in performance between each sensor may be due to differences in internal stresses when cutting the wire elements.

Other uncertainty parameters included length of the amorphous wire 45 ± 0.30 mm, the volume size of the sensor $750 \pm 17.00\ mm^3$, number of turns 200 ± 1.00, length of the coil $30 \pm 0.30\ mm$, the magnetic field $900 \pm 9.54\ A/m$, frequency $500 \pm$0.57 mHz, twisting 0.70 ± 0.001 rad. By comparing the coefficients of determination, the linearity for S3 and S4 (0.98 and 0.96) are more than S1 and S2 (0.95 and 0.94). Furthermore, the uncertainty of sensitivity has decreased from 0.02 mV/cm in S2 to 0.005 mV/cm in S4 as shown in Table 5-5. Consequently, fixing both ends of the amorphous wire during preparation (method number two) has increased linearity and decreased uncertainty.

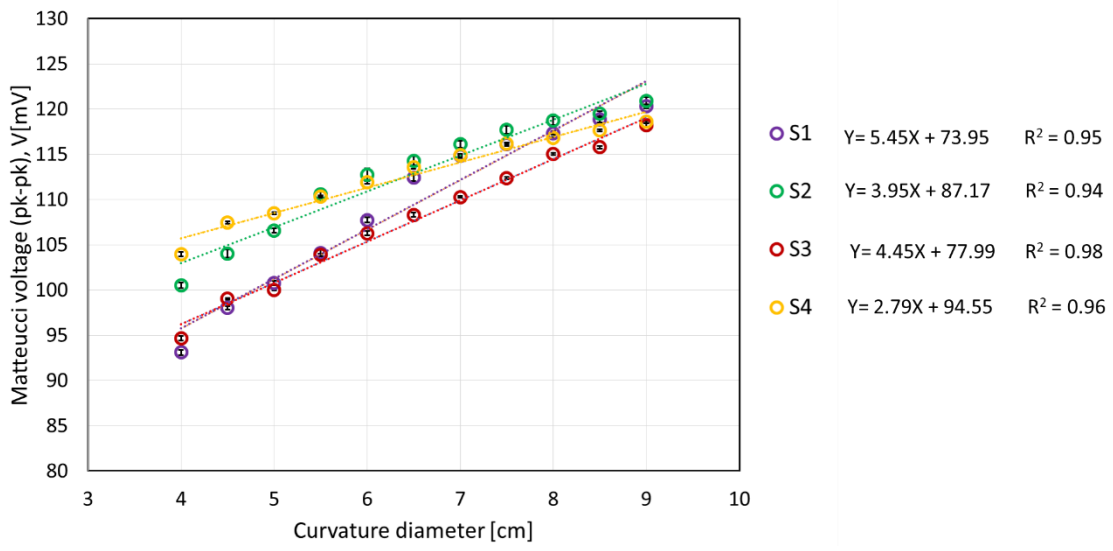

Figure 5-26: Comparison between four sensors made with AF10 amorphous wire, magnetised in 0.9 kA/m magnetic field and 500 Hz frequency, twisted 0.70 rad/cm

5.8 Flexible bending sensor with annealed amorphous wire

As the method used to make S3 and S4 (method number two) had less uncertainies, three more sensors named SA1, SA2, TSA were made using the same method but using annealed AF10 amorphous wire. Annealing was conducted by passing a 0.5 A current through the wire for one minute. To see the effect of twisting, two of the wires were annealed without any twisting (SA1 and SA2) and the third one was twisted by 0.70 rad/cm (TSA). The results are shown in Figure 5-28. To evaluate the repeatability, the SD was calculated using Eq.(4-5) for the average of 5 measurements in each point. The maximum SD was 0.61 mV, the minimum was 0.18 mV for the SA1, 0.37 mV and 0.16 mV for the SA2 and 0.62 mV and 0.33 mV for the TSA. An uncertainty budget is included in Table 5-4 and a comparison of the uncertainties for all of the sensors is summarised in Table 5-5. Table 5-4 shows a statistical evaluation of repeatability given to one standard deviation assuming a normal distribution. For a normal distribution, one standard deviation encompasses 68.27% of the area under the curve as shown in Figure 5-27. This means that there is about 68% confidence that the measured value y lies within the stated limits. When it is possible to assess only upper and lower bounds of an error, a rectangular distibution should be assumed for the uncertainty associated with this error. Then if a_i is the semi-range limit, the standard uncertainty is given by [164]:

$$u(x_i)=\frac{a_i}{\sqrt{3}} \qquad (5\text{-}4)$$

Therefore the uncertainty of equipments has been calculated by using Eq.(5-4). Where a_i is the resolution of oscilloscope and micormeter respectively.

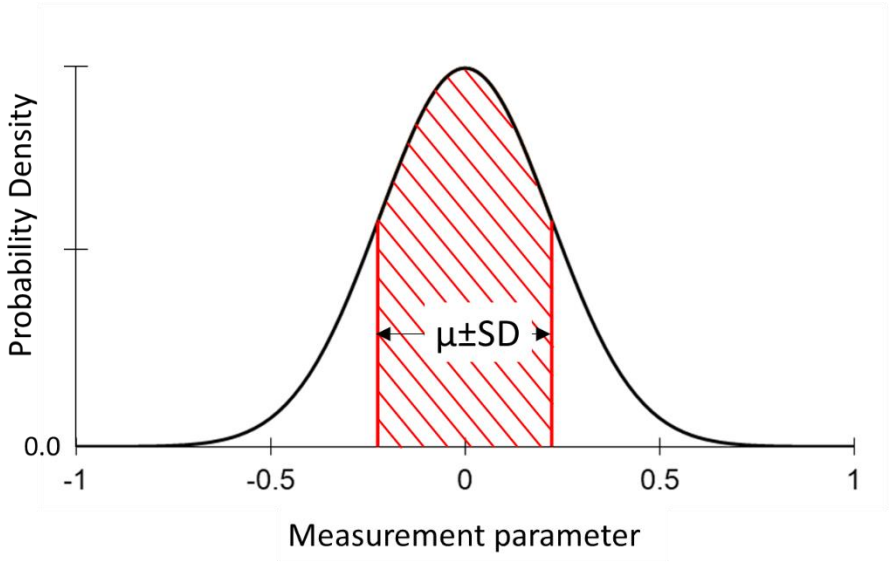

Figure 5-27: Normal distribution. The hatched area represents 1 standard deviation (SD) from the centre of the distribution (μ). This corresponds to approximately 68 % of the area under the curve.

As it can be seen in Table 5-5, the SA1 has the highest sensitivity and linearity of 5.62 mV/cm and 0.98, which shows that annealing has had a modest effect improving the sensor's performance. S4 has the smallest sensitivity of 2.79 mV/cm and TSA has the smallest linearity of 0.92. S4 with the lowest sensitivity has the minimum SD of 0.16 mV but the sensor with the twisted annealed wire with the lowest linearity has also the maximum SD of 0.47 mV. The twisted annealed and annealed sensors (TSA,SA1,SA2) have higher sensitivity in general compared to S1-S4 , however S3 and S2 are comparable with the annealed ones with the highest linearity and sensitivity occurring in SA1. Overall, SA1 is the best sensor, although all sensor performances are comparable except for S4.

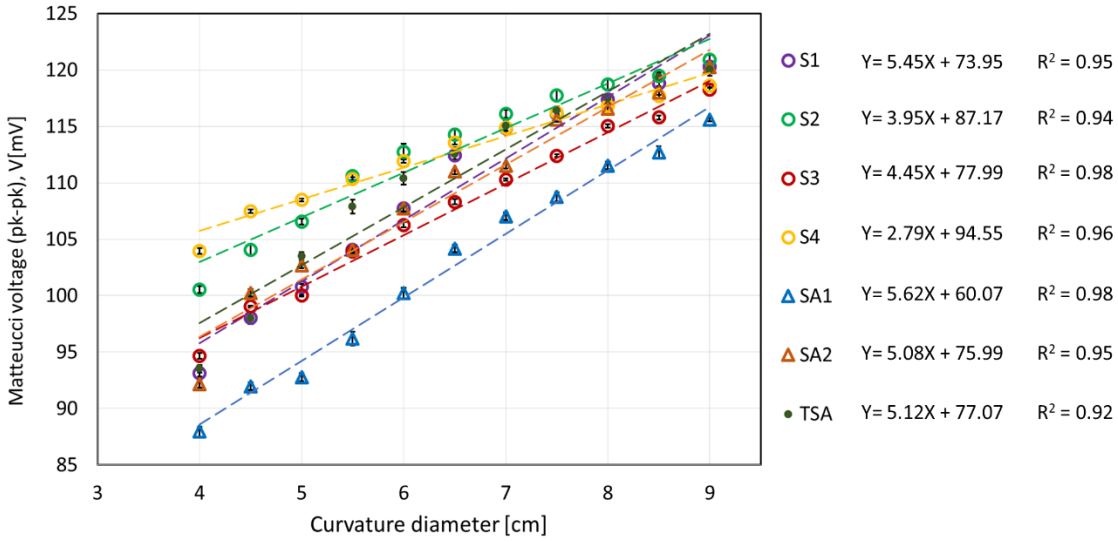

Figure 5-28: Comparison between sensors with as-cast, annealed and twisted annealed AF10 amorphous wire, twisted 0.70 rad/cm (271 MPa torsion stress), magnetised in 0.9 kA/m magnetic field and 500 Hz frequency

Table 5-4: Uncertainty budget for sensors

	Source of uncertainty	Value	Probability distribution	Divisor	Standard uncertainty
V_{RP}	SD Repeatability of Matteucci effect	0.6 mV	Normal	1	0.6 mV
V_{RS}	Resolution of oscilloscope	0.25 mV	Rectangular	√3	0.14 mV
R	Resolution of micro meter	0.0005 cm	Rectangular	√3	0.00028 cm

Table 5-5: Comparison between sensors sensitivity, linearity and uncertainty made with AF10 amorphous wires which are magnetised in 0.6 kA/m and 500 Hz frequency, twisted 0.70 rad/cm (271 MPa torsion stress)

Sensors	Sensitivity (mV/cm)	Linearity (R^2)	Max SD (mV)	Min SD (mV)	Average SD (mV)	Uncertainty of sensitivity (mV/cm)
S1	5.45	0.95	0.36	0.18	0.27	0.01
S2	3.95	0.94	0.67	0.24	0.45	0.02
S3	4.45	0.98	0.27	0.11	0.19	0.01
S4	2.79	0.96	0.25	0.07	0.16	0.005
SA1	5.62	0.98	0.61	0.18	0.39	0.02
SA2	5.08	0.95	0.37	0.16	0.26	0.01
TSA	5.12	0.92	0.62	0.33	0.47	0.02

5.9 Bending angle measurements from bending curvature

The sensitivity of the proposed bending sensor in this work was expressed in terms of mV/cm where the curved surface was quantified in terms of its diameter of curvature. Other researchers have used V/rad to characterise their sensor. To be able to compare the results of this research with the findings of other researchers, a translation from V/cm to V/rad has been performed. As there is no exact solution an estimate is given here. To do this, an arc with radius R was mapped on the curvature surface as shown in Figure 5-29. The length of the sensor in the curvature surface is always fixed and equal to L. The curvature surface (sensor) can be estimated by two tangential lines Line 1 and Line 2 which are drawn from either side of the sensor. Then, the angle Θ_b on the intersection of these two lines can be used as an indication of the amount of bending of the sensor due the specific curvature surface. R will have a direct relationship with angle Θ_b.

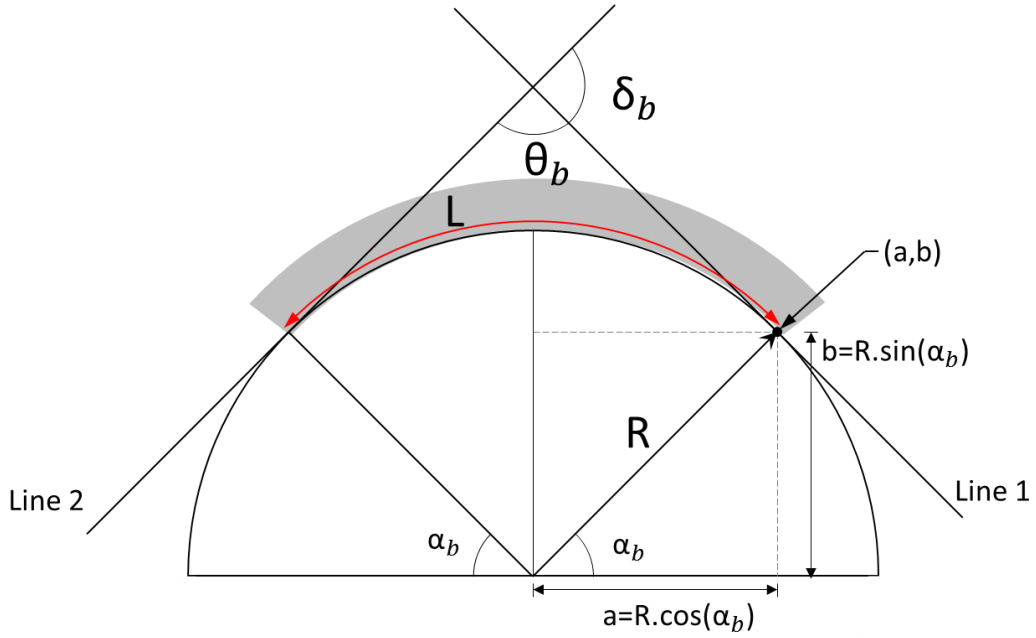

Figure 5-29: Bending sensor with the length of L (highlighted in grey) mapped on an arc (R,180) to estimate the curvature in radius R with a bending angle of δ_b.

The sensitivity of the proposed bending sensor in this work was expressed in terms of mV/cm where the curved surface was quantified in terms of its diameter of curvature. Other researchers have used V/rad to characterise their sensor. To be able to compare the results of this research with the findings of other researchers, a translation from V/cm to V/rad has been performed. As there is no exact solution an estimate is given here. To do this, an arc with radius R was mapped on the curvature surface as shown in Figure 5-29. The length of the sensor in the curvature surface is always fixed and equal to L. The curvature surface (sensor) can be estimated by two tangential lines Line 1 and Line 2 which are drawn from either side of the sensor. Then, the angle Θ_b on the intersection of these two lines can be used as an indication of the amount of bending of the sensor due the specific curvature surface. R will have a direct relationship with angle Θ_b.

To determine the equation of a tangent to a circle with centre (0,0) and radius R at point (a,b), it is required to calculate the slope of tangent which at the point of contact (a,b) is perpendicular to the radius of the circle. The slope of the radius drawn to point (a,b) is b/a. Line 1 equation can be expressed as follows:

$$y = -\frac{a}{b}x + (\frac{a^2}{b} + b) \qquad (5\text{-}5)$$

Where a and b can be expressed in terms of α_b and R, as shown in Figure 5-29.

In a similar way, the Line 2 equation can be determined using the contact point (a,b) and radius slope at the contact point equal to a/b.

The angle between Line 1 and Line 2 can be calculated from the following equation where m_1 and m_2 are their slopes respectively:

$$\theta_b = \tan^{-1}\frac{m_1 - m_2}{1 + m_1 m_2} \tag{5-6}$$

An approximate relationship between curvature and bend angle had to be developed. To extrapolate the bend angle from the arc, induced through curvature, the following equation applies.

$$\alpha_b = \frac{\pi}{2} - \frac{L}{2R} \tag{5-7}$$

Therefore

$$\theta_b = \tan^{-1}\frac{2\cot\alpha_b}{1-(\cot\alpha_b)^2} \tag{5-8}$$

Substitute Eq.(5-8) into Eq.(5-7), results in Eq. (5-9).

$$\theta_b = \tan^{-1}\frac{2\cot(\frac{\pi}{2} - \frac{L}{2R})}{1 - (\cot(\frac{\pi}{2} - \frac{L}{2R}))^2} \tag{5-9}$$

As $\tan(\theta_b) = \cot(\frac{\pi}{2} - \theta_b)$, Eq.(5-9) can be rewritten as Eq.(5-10).

$$\theta_b = \tan^{-1}\frac{2\tan(\frac{L}{2R})}{1 - (\tan(\frac{L}{2R}))^2} \tag{5-10}$$

And finally as

$$\tan(2\theta_b) = \frac{2\tan(\theta_b)}{1 - (\tan(\theta_b))^2} \tag{5-11}$$

By substituting Eq.(5-11) into Eq.(5-10),

$$\theta_b = \tan^{-1}(\tan(2\frac{L}{2R})) \qquad -\frac{\pi}{2} < \theta_b < \frac{\pi}{2} \tag{5-12}$$

And finally

$$\theta_b = \frac{L}{R} \tag{5-13}$$

The bending angle δ_b is related to θ_b, by Eq.(5-14).

$$\delta_b = 180 - \theta_b \tag{5-14}$$

Substituting the diameter values (40 mm – 90 mm) in Eq. 5-13 for the curved surfaces shown in figure 5-14-b, produces a bending range from 1.11 rad to 2.49 rad which was used to characterise the bending sensor in this work. As an example, the uncertainty of the Matteucci voltage measurement was 0.02 mV/cm for SA1, therefore because of the linear relationship of the Matteucci voltage to bending angle (Figure 5-30), the uncertainty of the bending angle equalled 0.003 rad. As shown in Figure 5-30-a linear trend line was fitted to each of the sensor outputs against bending angle. Extrapolating the data in Figure 5-29 to zero bending angle enables a prediction of the sensor output for a flat surface. A comparison of the predicted values with actual zero bending measurements are shown in Table 5-6 for all sensors. The maximum difference between the sensor measurement and the extrapolated values is less than 4 % suggesting a close linear fit over the whole bending range from 0 to 2.49 rad.

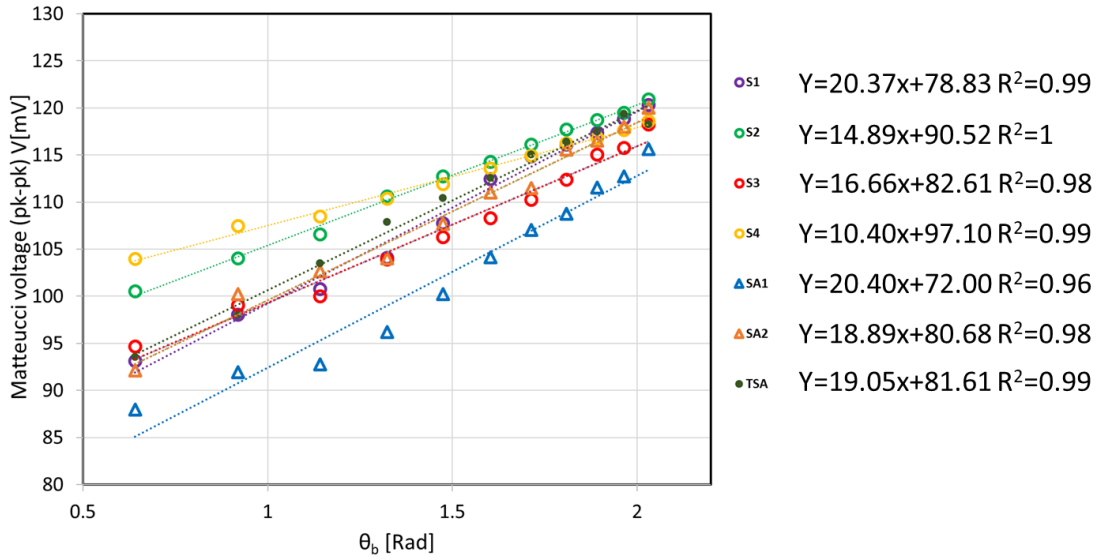

Figure 5-30: Comparison between sensors with as-cast, annealed and twisted annealed AF10 amorphous wire, twisted 0.70 rad/cm (271 MPa torsion stress), magnetised in 0.9 kA/m magnetic field and 500 Hz frequency due to bending angle

Table 5-6: Comparison between sensor in flat condition and trendline extrapolation to Π rad

Sensor type	Flat condition output (mV)	Trend line extrapolation to Π (mV)	% error
S1	130	134.81	3.7
S2	134	129.50	3.3
S3	137	141.83	3.5
S4	130	135.52	3.8
SA1	130	135.00	3.8
SA2	134	138.28	3.1
TSA	136	141.01	3.6

An important point to note in this work is that the bending angle has been defined in terms of the sensor's length and the curvature of the surface (i.e. the diameter). This is a somewhat arbitrary definition and needs consideration when calibrating the sensor. To illustrate this point further, Figure 5-31 shows two examples of how the sensor's output voltage depends on both sensor length and surface curvature. Figure 5-30-a shows that for the same curvature, sensors of different length will have the same internal stress distribution but different output voltages because this

is also proportional to length. The bending angles will also be considered different due to the definition used in Figure 5-29 despite the curvature being identical. Figure 5-31-b illustrates how two sensors with different lengths each on different curvatures will give identical bend angles according to the bending angle definition used here, however, the output for L_4 will be much smaller than that for L_3. To summarise, the sensor's output voltage is inversely proportional to the bending angle (Figure 5-30) and directly proportional to its length (Figure 4-10). Therefore, the best signal-to-noise ratio will be obtained for large output voltages when the curvature is small and the sensor is long. This high signal and linearity over small bending angles is a distinct advantage when compared to commercial flex sensors which are non-linear between 0 to 0.35 rad. Another advantage is its large measurement range of 0 to 2.49 rad. This may be extended even further with the use of shorter sensors although this will reduce the level of the output signal. When using this type of sensor, it is therefore important to calibrate the sensor based on its length and the type of curved surface to be measured. For example, to measure finger flexure the sensor dimensions will need to closely match the size of the individual's joint.

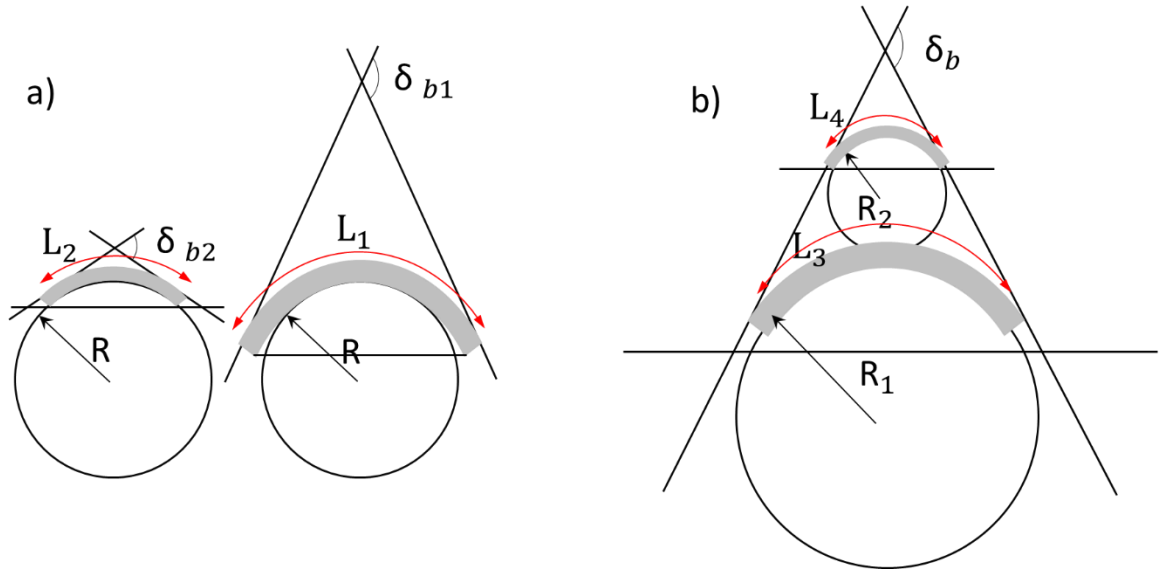

Figure 5-31: a) The same curvature but different sensor length (highlighted in grey) gives different bend angles, b) different sensor lengths and different curvatures give the same bend angle

Flex sensors are prevalent in modern wearable devices, particularly in the area of instrumented gloves used for measuring hand and finger posture. The technologies currently used in such gloves tend to be expensive fiber optic solutions, less reliable resistance or capacitance-based sensors or complex accelerometer systems. Table 5-7 summarises the specifications of some commercially available bend sensors.

The table shows that most commercial sensors perform with a bend resolution somewhere between 0.002 rad and 0.03 rad and a measurement range from 0 and Π/2 rad. However, not all of these exhibit a linear response, the relatively cheap resistive flex sensors for example perform poorly over small bend angles. The sensors developed as part of this work compare very favourably with the commercial ones and have demonstrated a measurement resolution of 0.003 rad, good linearity ($0.92 < R^2 < 0.98$) and a confirmed measurement range between 0 and 2.49 rad.

Table 5-7: Comparison of bending sensors

Sensors	Linearity	Sensitivity	Resolution	Measuring range
Commercial bends sensor from Bebop sensors, 9-degree IMU and smart fabric bend sensor [165]	-		±0.03 rad	
Commercial bend sensors from Spectra Symbol (Resistive flex sensor) [144]	Nonlinear between 0-∏/6	Variable	Resolution <0.02 rad	∏/2
Optical-based sensor [166]	Non-linear under ∏/6	Low sensitivity in small angles	-	∏/2
Bending sensor based on Hall effect [151]	-	For smaller radii, only a minor decay in sensitivity is observed	-	6 to 32 mm*
Single-mode optical fibre sensor [167]	Nonlinear	-	0.002 rad	∏/2
Embedded hetero-core fibre optic sensor [168]	Linear	-	0.01 rad	1.70 rad
Potentiometer[169]	Linear	-	-	-
Commercial bend sensor, Resistance base sensor(Shadow monitor)[170]	Nonlinear	Variable	0.02 rad	-
Commercial bend sensor, Resistance base sensor (WU Glove)[148]	Linear after modification	-	0.03 rad	-

Note: '-'means the literature did not report the corresponding performance index. * In this paper curvature is recorded instead of angle

To conclude three kinds of sensors have been developed, the first one is a strain sensor with a gauge factor of 601 $\pm$ 30 for AC20 amorphous wire at 2 kHz frequency and 0.43 rad/cm twist angle. This is an excellent result compared to the much smaller gauge factors achieved in resistive foil gauges. Secondly, a simple flex sensor has been developed to measure strain by using an AF10 amorphous wire excited with a planar coil. This sensor is light (0.9 g) and has high strain sensitivity equivalent to a gauge factor of 767, but it overheats when the excitation current is more than 0.1 A and the output Matteucci voltage is low. Finally, a flexible bend sensor has been developed capable of measuring curvature diameters ranging from 40 mm to 90 mm. It is small and light (2.5 g) and can sit on the finger easily, and therefore a good candidate for wearable glove sensors. A high sensitivity and linearity of (5.62 ± 0.02) mV/cm and 0.98 respectively was calculated for this sensor. Using a definition of bending angle based on surface curvature a measurement resolution of ± 0.003 rad was achieved with a measurement range of 0 to 2.49 rad.

6 Conclusion and future work

6.1 Conclusion

This work culminated in the development of a flexible bend sensor by utilising the Matteucci effect in amorphous wires. The aim was to develop a sensor with high linearity and sensitivity and superior performance compared to existing technologies. This was achieved by adopting a novel approach, using a flexible solenoid to excite the amorphous wire and detecting voltage pulses caused by the Matteucci effect.

In this work, a better understanding of the Matteucci effect for sensor applications was achieved through the magnetic characterisation of amorphous wires. Matteucci voltages across the ends of the wire were measured for various tensile and torsion stresses and a range of applied magnetic field amplitudes and frequencies. Further characterisation also included studies of the B-H curve, domain imaging by Kerr microscopy and the Bitter technique, and an investigation into the effects of annealing on amorphous wires.

Results show that:

1. Amorphous wires are very sensitive to both axial and torsional applied stresses. The magnitude of the Matteucci effect decreased in as-cast and annealed AF10 amorphous wire when applying tensile stresses. In this case, the stress is inhibiting the formation of a helical magnetisation anisotropy present in the wire.
2. However, the opposite is true in AC20 amorphous wire indicating an increase in the helical anisotropy.
3. Increases in excitation frequency and twisting angle both led to increases in the Matteucci voltage in both AF10 and AC20 amorphous wires. The higher the degree of twisting, the higher the induced voltage in the wire because of the increased helical anisotropy.
4. The near-zero amorphous wire (AC20) surprisingly produced a Matteucci output comparable to that found in highly magnetostrictive wires and with much better linearity when measured as a function of axial stress.

5. Increasing the length of the wire increases the Matteucci voltage confirming the hypothesis that the Matteucci voltage is due to the change in circular magnetisation integrated over the length of the wire.
6. Annealing improved the Matteucci voltage at small tensile stress but values were very similar at larger stress levels.
7. Domain imaging by the Bitter technique showed a zigzag domain structure in AF10 amorphous wires. And by twisting the wire from 0 to 2∏ rad a transition from a circumferential zigzag pattern to an arrangement of regularly spaced parallel domain walls occurred.
8. Domain imaging by Kerr microscopy showed movement of domain boundaries when twisting from 0 to ∏/2 rad (corresponding to 0 to ∏/4 rad/cm) in AF10 amorphous wire. In AC20, domain images were hard to detect possibly because the expected bamboo structure was too small for optical observations. However, structures similar to a vortex domain structure were observed.

This body of work has presented new insights into the Matteucci voltage characteristics in short amorphous wires, an area neglected in previous studies.

In the second stage of this work, the findings from the characterisation work were used as guide for sensor development. A number of sensors were developed, beginning with:

1. A strain sensor with a gauge factor of 601 $\pm$ 30 for AC20 amorphous wire at 2 kHz frequency and 0.43 rad/cm twist angle. This gauge factor is much higher than that seen for resistive foil gauges and other similar sensors.
2. Secondly, a simple flex sensor has been developed to measure strain using AF10 amorphous wire excited by a flexible planar coil. 3D modelling was performed in this work to demonstrate the feasibility of employing FEM in the process for designing planar coil sensors. Different geometries were investigated and among them, the square shape was chosen to uniformly magnetise the amorphous wire element. The designed sensor was small and lightweight and had an equivalent gauge factor of 767. The limitations of this particular sensor was overheating with currents greater than 0.1 A and the output Matteucci voltage was low.
3. Finally, a flexible bend sensor was developed, to measure various curvature diameters ranging from 40 mm to 90 mm. A simple model was proposed in this thesis to translate these curvature measurements into equivalent

bending angles. The equivalent measurement range in this case was 1.11 to 2.49 rad but additional measurements at 0 were consistent with a linear output spanning the whole range from 0 to 2.49 rad. Seven sensors were made to investigate the variability and repeatability of sensor performance due to the manufacturing methods. Three of them were subjected to annealing during manufacture which improved the linearity of the sensor. The annealed sensors had generally higher sensitivity compared to the non-annealed sensors but all sensors exhibited consistent linear behaviour. When compared to commercially available ones, the bend sensors developed in this work achieved a better measurement range (0 and 2.49 rad) whilst delivering good linearity ($0.92 < R^2 < 0.98$). A measurement resolution of 0.003 rad also compares very well with the 0.002 – 0.03 rad seen in commercial sensors,

6.2 Future work

The feasibility of measuring bend angle using a novel Matteucci effect sensor has been clearly demonstrated in this work. However, a number of limitations have been identified which require further development in order to produce a practical sensing device.

The manufacturing methodology requires further investigation to eliminate variability in output sensitivity as seen in the non-annealed bend sensors. Annealing reduced this variability but further study is needed to optimise the procedure.

Future designs should be concerned with reducing sensor size and integrating suitable circuit conditioning and amplification electronics that can be interfaced with standard wireless communication technologies.

Another potential area for improvement is the optimisation of output sensitivity. During the bending process, the sensor experiences both a compressive and tensile stress distribution along the wire sensing element. By implementing a sensor with a composite layered structure, it is possible to shift the neutral bend axis away from the centre of the amorphous sensing wire leaving a uniform tensile (or compressive) stress in the wire. This should significantly improve output sensitivity.

The square planar coil strain sensor produced an encouraging, near linear output as a function of applied stress despite its non-optimal configuration. By utilising four

separate wire elements positioned in cross formation over each of the planar coil's quadrants, the sensor will function similar to a pair of two-element 90-degree planar Rosette Strain Gauges and thus improve strain sensitivity. The mechanical coupling between the wire and planar coil also needs further study.

References

[1] O. D. Lara and M. A. Labrador, "A survey on human activity recognition using wearable sensors," *IEEE Communications Surveys & Tutorials,* vol. 15, no. 3, pp. 1192-1209, 2012.

[2] L. Wang, T. Meydan, and P. Williams, "Design and evaluation of a 3-D printed optical sensor for monitoring finger flexion," *IEEE Sensors Journal,* vol. 17, no. 6, pp. 1937-1944, 2017.

[3] R. Ch. Webb , A. P. Bonifas, A. Behnaz, Y. Zhang , KJ. Yu, H. Cheng, M. Shi, Z.Bian, Zh. Liu, Y. Kim, W. Yeo, J. S. Park, J. Song, Y. Li, Y. Huang, A. M. Gorbach and J. Rogers "Ultrathin conformal devices for precise and continuous thermal characterization of human skin," *Nature Materials,* vol. 12, no. 10, pp. 938-944, 2013.

[4] M. G. Hart and G. Hooper, "Clinical associations of Dupuytren's disease," (in eng), *Postgrad Med J,* vol. 81, no. 957, pp. 425-428, 2005, doi: 10.1136/pgmj.2004.027425.

[5] M. Borghetti, E. Sardini, and M. Serpelloni, "Sensorized glove for measuring hand finger flexion for rehabilitation purposes," *IEEE Transactions on Instrumentation and Measurement,* vol. 62, no. 12, pp. 3308-3314, 2013.

[6] J. Nabias, A. Asfour, and J.P. Yonnet, "The impact of bending stress on the performance of giant magneto-impedance (GMI) magnetic sensors," *Sensors,* vol. 17, no. 3, pp. 640, 2017.

[7] E. Pulido, R.P. del Real , F. Conde , G. Rivero , M. Vazquez , E. Ascasibar , A. Hernando, "Amorphous wire magnetic field and DC current sensor based on the inverse Wiedemann effect," *IEEE Transactions on Magnetics,* vol. 27, no. 6, pp. 5241-5243, 1991.

[8] C. Morón, C. Cabrera, A. Morón, A. García, and M. González, "Magnetic sensors based on amorphous ferromagnetic materials: A review," *Sensors,* vol. 15, no. 11, pp. 28340-28366, 2015.

[9] K. Mohri, *F. B. Humphrey, L. V. Panina, Y. Honkura, J. Yamasaki, T. Uchiyama, M.Hirami*, "Advances of amorphous wire magnetics over 27 years," *Physica Status Solidi (a),* vol. 206, no. 4, pp. 601-607, 2009, doi: doi:10.1002/pssa.200881252.

[10] K. Mohri, F. Humphrey, J. Yamasaki, and K. Okamura, "Jitter-less pulse generator elements using amorphous bistable wires," *IEEE Transactions on Magnetics,* vol. 20, no. 5, pp. 1409-1411, 1984, doi: 10.1109/TMAG.1984.1063201.

[11] N. DeCristofaro, "Amorphous metals in electric-power distribution applications," *MRS Bulletin,* vol. 23, no. 5, pp. 50-56, 1998.

[12] C. Mattmann, F. Clemens, and G. Tröster, "Sensor for measuring strain in textile," *Sensors,* vol. 8, no. 6, pp. 3719-3732, 2008.

[13] U. Tata, H. Cao, V. Landge, C. M. Nguyen, Y.-S. Seo, and J.-C. Chiao, "Wireless strain sensor based on amorphous carbon for human-motion detection," in *2013 IEEE Topical Conference on Biomedical Wireless Technologies, Networks, and Sensing Systems,* pp. 31-33, 2013.

[14] J. Kosel, H. Hauser, Y. Didosyan, and G. Pertl, "Stress dependence of the differential susceptibility of soft magnetic ribbons," *Journal of Applied Physics,* vol. 97, no. 10, pp. 10F902, 2005.

[15] D. Jiles, *Introduction to magnetism and magnetic materials*. CRC Press, 2015.

[16] K. J. Overshott, "Amorphous ribbon materials and their possibilities," *Electronics and Power,* vol. 25, no. 5, pp. 347-350, 1979, doi: 10.1049/ep.1979.0210.
[17] F. Luborsky, J. Becker, and R. McCary, "Magnetic annealing of amorphous alloys," *IEEE Transactions on Magnetics,* vol. 11, no. 6, pp. 1644-1649, 1975, doi: 10.1109/TMAG.1975.1058974.
[18] S. Chikazumi and C. D. Graham, *Physics of Ferromagnetism 2e*. OUP Oxford, 2009.
[19] K. Overshott and T. Meydan, "Unmagnetized amorphous ribbon transducers," *IEEE Transactions on Magnetics,* vol. 20, no. 5, pp. 948-950, 1984, doi: 10.1109/TMAG.1984.1063501.
[20] R. Bozorth, *FERROMAGNETISM, Wiley*, 1951.
[21] F. Bloch, vol. 74, no. 295, 1932.
[22] C. Kittel, "Physical Theory of Ferromagnetic Domains," *Reviews of Modern Physics,* vol. 21, no. 4, pp. 541-583, 10/01/ 1949, doi: 10.1103/RevModPhys.21.541.
[23] S. Zapperi, P. Cizeau, G. Durin, and H. E. Stanley, "Dynamics of a ferromagnetic domain wall: Avalanches, depinning transition, and the Barkhausen effect," *Physical Review B,* vol. 58, no. 10, pp. 6353-6366, 09/01/ 1998, doi: 10.1103/PhysRevB.58.6353.
[24] J. Joule, "Sturgeon's Annal of *Electricity",* vol. 8, pp. 219, 1842.
[25] J. P. Joule, "XVII. On the effects of magnetism upon the dimensions of iron and steel bars," *The London, Edinburgh, and Dublin Philosophical Magazine and Journal of Science,* vol. 30, no. 199, pp. 76-87, 1847/02/01 1847, doi: 10.1080/14786444708645656.
[26] S. Chikazumi and S. H. Charap, *Physics of Magnetism: Engl. ed. prepared with the assistance of*. Wiley, 1964.
[27] T.Meydan, "Transducers using amorphous ribbon materials," PhD thesis, Wolfson center, Cardiff university, 1984.
[28] Unitika. Ltd. *Amorphous metal fibers*, Japan.
[29] Y. Sakurai, Y. Hamakawa, K. Shirae, T. Masumoto, and K. Suzuki, *Current Topics in Amorphous Materials: Physics & Technology*. Elsevier Science, 2013.
[30] F. B. Humphrey and E. M. Gyorgy, "Flux Reversal in Soft Ferromagnetics," *Journal of Applied Physics,* vol. 30, no. 6, pp. 935-939, 1959, doi: 10.1063/1.1735265.
[31] W. Göpel, J. Hesse, J. N. Zemel, R. Boll, and K. J. Overshott, *Sensors, Magnetic Sensors*. Wiley, 1989.
[32] R. Lassow, "Novel shock and vibration transducers using amorphous materials," PhD thesis, Cardiff University, 1995.
[33] L. Holmes, "Metallic glasses in sensors and transducers," *Electronics and Power,* vol. 28, no. 2, pp. 180-182, 1982, doi: 10.1049/ep.1982.0074.
[34] V. Madurga, J. L. Costa, A. Inoue, and K. V. Rao, "Magnetostrictive influence on the bistability of amorphous wires," *Journal of Applied Physics,* vol. 68, no. 3, pp. 1164-1168, 1990, doi: 10.1063/1.346712.
[35] A. Zhukov, *High Performance Soft Magnetic Materials*. Springer International Publishing, 2017.
[36] Y. Konno and K. Mohri, "Magnetostriction measurements for amorphous wires," *IEEE Transactions on Magnetics,* vol. 25, no. 5, pp. 3623-3625, 1989.
[37] D. Atkinson and P. Squire, "The magnetic properties of amorphous wires and their applications," in *IEE Colloquium on Magnetic Materials for Sensors and Actuators (Digest No. 1994/183)*: IET, pp. 1/1-1/2, 1994.

[38] C. Fosalau, M. Cretu, and O. Postolache, "Circular displacement sensor using magnetostrictive amorphous wires," *IEEE Transactions on Magnetics,* vol. 36, no. 3, pp. 557-560, 2000.
[39] K. Mohri, F.B. Humphrey, L.V. Panina, Y. Honkura, J.Yamasaki, T.Uchiyama, M.Hirami, "Advances of amorphous wire magnetics over 27 years," *Physica Status Solidi (A) Applications and Materials Science,* Article vol. 206, no. 4, pp. 601-607, 2009, doi: 10.1002/pssa.200881252.
[40] M. Vazquez and A. Hernando, "A soft magnetic wire for sensor applications," *Journal of Physics D: Applied Physics,* vol. 29, no. 4, pp. 939, 1996.
[41] D. Atkinson, M. Gibbs, P. Squire, and Q. Pankhurst, "The magnetic and magnetoelastic properties of surface crystallized iron-based amorphous wire," *Journal of Magnetism and Magnetic Materials,* vol. 131, no. 1-2, pp. 19-28, 1994.
[42] C. Kim, S. Yoon, and M. Vazquez, "Evaluation of helical magnetoelastic anisotropy in Fe-based amorphous wire from the decomposed susceptibility spectra," *Journal of Magnetism and Magnetic Materials,* vol. 223, no. 3, pp. 199-202, 2001.
[43] F. Kinoshita, R. Malmhall, K. Mohri, F. Humphrey, and J. Yamasaki, "Influence of applied tensile and compressive stress on large Barkhausen and Matteucci effects in amorphous wires," *IEEE Ttransactions on Magnetics,* vol. 22, no. 5, pp. 445-447, 1986.
[44] G. Bordin, G. Buttino, A. Cecchetti, and M. Poppi, "Peculiar behavior of the magneto-impedance in Fe-based amorphous wires under torsion," *Journal of Magnetism and Magnetic Materials,* vol. 222, no. 3, pp. 257-262, 2000.
[45] D. Atkinson, M. R. J. Gibbs, P. T. Squire, and Q. Pankhurst, "The magnetic and magnetoelastic properties of surface crystallized iron-based amorphous wire," *Journal of Magnetism and Magnetic Materials,* vol. 131, no. 1, pp. 19-28, 1994/03/01/ 1994, doi: https://doi.org/10.1016/0304-8853(94)90005-1.
[46] K. Mohri, F. B. Humphrey, K. Kawashima, K. Kimura, and M. Mizutani, "Large Barkhausen and Matteucci effects in FeCoSiB, FeCrSiB, and FeNiSiB amorphous wires," *IEEE Transactions on Magnetics,* vol. 26, no. 5, pp. 1789-1791, 1990, doi: 10.1109/20.104526.
[47] A. Hernando and J. Barandiaran, "The initial Matteucci effect," *Journal of Physics D: Applied Physics,* vol. 8, no. 7, pp. 833-840, 1975/05/11 1975, doi: 10.1088/0022-3727/8/7/016.
[48] K. Mohri, F. Humphrey, J. Yamasaki, and F. Kinoshita, "Large Barkhausen effect and Matteucci effect in amorphous magnetostrictive wires for pulse generator elements," *IEEE Transactions on Magnetics,* vol. 21, no. 5, pp. 2017-2019, 1985.
[49] R. Skórski, "Matteucci effect: its interpretation and its use for the study of ferromagnetic matter," *Journal of Applied Physics,* vol. 35, no. 4, pp. 1213-1216, 1964.
[50] K. Kawashima, T. Kohzawa, M. Takagi, K. Mohri, M. Kanoh, and L. Panina, "Mechanism of Matteucci effect using amorphous magnetic wires," *IEEE Translation Journal on Magnetics in Japan,* vol. 8, no. 5, pp. 318-325, 1993.
[51] K. Mohri and S. Takeuchi, "Sensitive bistable magnetic sensors using twisted amorphous magnetostrictive ribbons due to Matteucci effect," *Journal of Applied Physics,* vol. 53, no. 11, pp. 8386-8388, 1982.
[52] H. Takamure, J. Yamasaki, K. Mohri, and I. Ogasawara, "Matteucci Effect in Amorphous Wires with Negative Magnetostriction," *IEEE Translation Journal on Magnetics in Japan,* vol. 5, no. 7, pp. 540-546, 1990.
[53] J. Yamasaki, K. Mohri, H. Kawamura, H. Takamure, F. Humphrey, and R. Malmhall, "Magnetic properties of Co-Si-B amorphous wires prepared by

quenching in-rotating water technique," *IEEE Translation Journal on Magnetics in Japan,* vol. 4, no. 6, pp. 360-367, 1989.
[54] C. Favieres, C. Aroca, M. Sanchez, and V. Madurga, "Matteucci effect as exhibited by cylindrical CoP amorphous multilayers," *Journal of Applied Physics,* vol. 87, no. 4, pp. 1889-1898, 2000.
[55] E. Hristoforou and R. Reilly, "Displacement sensors using soft magnetostrictive alloys," *IEEE Transactions on Magnetics,* vol. 30, no. 5, pp. 2728-2733, 1994.
[56] R. Lassow and T. Meydan, "An angular accelerometer using amorphous wire," *IEEE Transactions on Magnetics,* vol. 31, no. 6, pp. 3179-3181, 1995, doi: 10.1109/20.490320.
[57] J. Gonzalez, J. Blanco, A. Hernando, J. Barandiaran, M. Vázquez, and G. Rivero, "Stress dependence of magnetostriction in amorphous ferromagnets: its variation with temperature and induced anisotropy," *Journal of Magnetism and Magnetic Materials,* vol. 114, no. 1-2, pp. 75-81, 1992.
[58] K. Mohri, K. Yoshino, H. Okuda, and R. Malmhall, "Highly accurate rotation-angle sensors using amorphous star-shaped cores," *IEEE Transactions on Magnetics,* vol. 22, no. 5, pp. 409-411, 1986.
[59] K. Mohri, "Review on recent advances in the field of amorphous-metal sensors and transducers," *IEEE Transactions on Magnetics,* vol. 20, no. 5, pp. 942-947, 1984, doi: 10.1109/TMAG.1984.1063522.
[60] J. R. Wiegand, "Bistable magnetic device," US, patent 3,820,090, 1974.
[61] P. Dimitropoulos and J. Avaritsiotis, "A micro-fluxgate sensor based on the Matteucci effect of amorphous magnetic fibers," *Sensors and Actuators A: Physical,* vol. 94, no. 3, pp. 165-176, 2001.
[62] C. Fosalau, C. Zet, M. Temneanu, and M. Antoniu, "A Novel Current Sensor Using Magnetostrictive Amorphous Wires," in *IMEKO-TC4 13th International Symposium on Measurements for Research and Industry Applications*, 2004, pp. 21-25.
[63] J. Velázquez, M. Vázquez, D.X. Chen, and A. Hernando, "Giant magnetoimpedance in nonmagnetostrictive amorphous wires," *Physical Review B,* vol. 50, no. 22, pp. 16737, 1994.
[64] K. Mandal and S. Ghatak, "Large magnetoresistance in an amorphous Co 68.1 Fe 4.4 Si 12.5 B 15 ferromagnetic wire," *Physical Review B,* vol. 47, no. 21, pp. 14233, 1993.
[65] M. Vázquez, J. Velázquez, and D.X. Chen, "Comment on ‘‘Large magnetoresistance in an amorphous Co 68.1 Fe 4.4 Si 12.5 B 15 ferromagnetic wire’’," *Physical Review B,* vol. 51, no. 1, pp. 652, 1995.
[66] R. Beach and A. Berkowitz, "Giant magnetic field dependent impedance of amorphous FeCoSiB wire," *Applied Physics Letters,* vol. 64, no. 26, pp. 3652-3654, 1994.
[67] K. Rao, F. Humphrey, and J. Costa-Krämer, "Very large magneto-impedance in amorphous soft ferromagnetic wires," *Journal of Applied Physics,* vol. 76, no. 10, pp. 6204-6208, 1994.
[68] M. Knobel, M. Sánchez, P. Marin, C. Gómez-Polo, M. Vázquez, and A. Hernando, "Influence of nanocrystallization on the magneto-impedance effect in FeCuNbSiB amorphous wires," *IEEE Transactions on Magnetics,* vol. 31, no. 6, pp. 4009-4011, 1995.
[69] T. Meydan, "Influence of stress on Matteucci and search coil voltages in amorphous wires," *Journal of Magnetism and Magnetic Materials,* vol. 249, no. 1, pp. 382-386, 2002/08/01/ 2002, doi: https://doi.org/10.1016/S0304-8853(02)00562-0.
[70] S. N. Kane, M. Vázquez, A. Hernando, and A. Gupta, "Influence of current annealing, stress, torsion and dc magnetic field on Matteucci effect in

amorphous wires," *Materials Science and Engineering: A,* vol. 304-306, pp. 1055-1057, 2001/05/31/ 2001, doi: https://doi.org/10.1016/S0921-5093(00)01754-8.
[71] M. Vázquez, J. González, J. M. Blanco, J. M. Barandiarán, G. Rivero, and A. Hernando, "Torsion dependence of the magnetization process in magnetostrictive amorphous wire," *Journal of Magnetism and Magnetic Materials,* vol. 96, no. 1, pp. 321-328, 1991/06/01/ 1991, doi: https://doi.org/10.1016/0304-8853(91)90646-R.
[72] M. Vázquez, C. Gómez-Polo, D.X. Chen, and A. Hernando, "Magnetic bistability of amorphous wires and sensor applications," *IEEE Transactions on Magnetics,* vol. 30, no. 2, pp. 907-912, 1994.
[73] A. Hernando, M. Vazquez, and J. Barandiaran, "Metallic glasses and sensing applications," *Journal of Physics E: Scientific Instruments,* vol. 21, no. 12, pp. 1129, 1988.
[74] M. Vazquez, A. Hernando, and O. Nielsen, "Magnetostriction and other magnetic properties of Co-Ni based amorphous alloys," *Journal of Magnetism and Magnetic Materials,* vol. 61, no. 3, pp. 390-394, 1986.
[75] A. Hernando, M. Vazquez, V. Madurga, and H. Kronmüller, "Modification of the saturation magnetostriction constant after thermal treatments for the Co58Fe5Ni10B16Si11 amorphous ribbon," *Journal of Magnetism and Magnetic Materials,* vol. 37, no. 2, pp. 161-166, 1983.
[76] G. Herzer, "Effect of external stresses on the saturation magnetostriction of amorphous Co-based alloys," in *Proc. Int. Conf. Soft Magnetic Materials*, pp. 355-357, 1986.
[77] V. Madurga, J. Barandiarán, M. Vázquez, O. V. Nielsen, and A. Hernando, "Magnetostriction of the rapidly quenched Co80Nb8B12 alloy: Dependence on quenching rate, structural relaxation, and temperature," *Journal of Applied Physics,* vol. 61, no. 8, pp. 3228-3230, 1987.
[78] M. Vázquez, C. Gomez Polo, J. Velázquez, and A. Hernando, "Bending stresses and bistable behavior in Fe-rich amorphous wire," *Journal of Applied Physics,* vol. 75, no. 10, pp. 5791-5793, 1994.
[79] J. Yamasaki, "Sensing function in amorphous magnetic materials," *IEEE Translation Journal on Magnetics in Japan,* vol. 7, no. 9, pp. 694-704, 1992.
[80] F. Humphrey, K. Mohri, and J. Yamasaki, "Re-entrant magnetic flux reversal in amorphous wires," *Magnetic Properties of Amorphous Metals,* pp. 110-116, 1987.
[81] A. Severino, C. Gómez-Polo, P. Marin, and M. Vázquez, "Influence of the sample length on the switching process of magnetostrictive amorphous wire," *Journal of Magnetism and Magnetic Materials,* vol. 103, no. 1-2, pp. 117-125, 1992.
[82] R. Schäfer and A. Hubert, "Domains in soft magnetic materials," *Le Journal de Physique IV,* vol. 8, no. PR2, pp. Pr2-283-Pr2-290, 1998.
[83] X. Xu, A. Moses, J. Hall, P. Williams, and K. Jenkins, "A Comparison of magnetic domain images using a modified bitter pattern technique and the Kerr method on Grain-oriented electrical steel," *IEEE Transactions on Magnetics,* vol. 47, no. 10, pp. 3531-3534, 2011.
[84] A. Chizhik and J. Gonzalez, *Magnetic Microwires: A Magneto-Optical Study*. Pan Stanford Publishing, 2014.
[85] J. Yamasaki, M. Takajo, and F. B. Humphrey, "Mechanism of re-entrant flux reversal in Fe-Si-B amorphous wires," *IEEE Transactions on Magnetics,* vol. 29, no. 6, pp. 2545-2547, 1993, doi: 10.1109/20.280959.
[86] A. Chizhik, J. Gonzalez, J. Yamasaki, A. Zhukov, and J. Blanco, "Vortex-type domain structure in Co-rich amorphous wires," *Journal of Applied Physics,* vol. 95, no. 5, pp. 2933-2935, 2004.

[87] Y. Kabanov, A. Zhukov, V. Zhukova, and J. Gonzalez, "Magnetic domain structure of wires studied by using the magneto-optical indicator film method," *Applied Physics Letters,* vol. 87, no. 14, pp. 142507, 2005.
[88] J. Yamasaki, F. Humphrey, K. Mohri, H. Kawamura, H. Takamure, and R. Mälmhäll, "Large Barkhausen discontinuities in Co-based amorphous wires with negative magnetostriction," *Journal of Applied Physics,* vol. 63, no. 8, pp. 3949-3951, 1988.
[89] B. H*ernando*, M. L. Sánchez, V. M. Prida, J. D. Santos, J. Olivera, F. J. Belzunce, G. Badini, and M. Vázquez, "Magnetic domain structure of amorphous Fe 73.5 Si 13.5 B 9 Nb 3 Cu 1 wires under torsional stress," *Journal of Applied Physics,* vol. 103, no. 7, pp. 07E716, 2008.
[90] M. Knobel, P. Allia, C. Gomez-Polo, H. Chiriac, and M. Vázquez, "Joule heating in amorphous metallic wires," *Journal of Physics D: Applied Physics,* vol. 28, no. 12, pp. 2398, 1995.
[91] H. Chiriac and I. Astefanoaei, "A model of the DC Joule heating in amorphous wires," *Physica Status Solidi (a),* vol. 153, no. 1, pp. 183-189, 1996.
[92] J. González, J. Blanco, M. Vázquez, J. Barandiarán, G. Rivero, and A. Hernando, "Influence of the applied tensile stress on the magnetic properties of current annealed amorphous wires," *Journal of Applied Physics,* vol. 70, no. 10, pp. 6522-6524, 1991.
[93] P. Gawronski, A. Chizhik, J. M. Blanco, and J. Gonzalez, "Remagnetization Process of Fe-Rich Amorphous Wire Under Time Dependent Tensile Stress," *Sensor Letters,* vol. 11, no. 1, pp. 32-35, 2013.
[94] A. Zhukov, V. Zhukova, J. Blanco, A. Cobeño, M. Vazquez, and J. Gonzalez, "Magnetostriction in glass-coated magnetic microwires," *Journal of Magnetism and Magnetic Materials,* vol. 258, pp. 151-157, 2003.
[95] F. Gattiker, F. Umbrecht, J. Neuenschwander, U. Sennhauser, and C. Hierold, "Novel ultrasound read-out for a wireless implantable passive strain sensor (WIPSS)," *Sensors and Actuators A: Physical,* vol. 145, pp. 291-298, 2008.
[96] G. Ausanio, A. Barone, C. Hison, V. Iannotti, G. Mannara, and L. Lanotte, "Magnetoelastic sensor application in civil buildings monitoring," *Sensors and Actuators A: Physical,* vol. 123, pp. 290-295, 2005.
[97] T. Klinger, H. Pfutzner, P. Schonhuber, K. Hoffmann, and N. Bachl, "Magnetostrictive amorphous sensor for biomedical monitoring," *IEEE Transactions on Magnetics,* vol. 28, no. 5, pp. 2400-2402, 1992.
[98] F. Lorussi, E. P. Scilingo, M. Tesconi, A. Tognetti, and D. De Rossi, "Strain sensing fabric for hand posture and gesture monitoring," *IEEE Transactions on Information Technology in Biomedicine,* vol. 9, no. 3, pp. 372-381, 2005.
[99] A. G. Mignani and F. Baldini, "Fibre-optic sensors in health care," *Physics in Medicine & Biology,* vol. 42, no. 5, pp. 967, 1997.
[100] E. L. Tan, B. D. Pereles, R. Shao, J. Ong, and K. G. Ong, "A wireless, passive strain sensor based on the harmonic response of magnetically soft materials," *Smart Materials and Structures,* vol. 17, no. 2, pp. 025015, 2008.
[101] C. Grimes, S. Mungle ,Z. Kefeng , K. Jain , R. Dreschel , M. Paulose and G. Ong , "Wireless magnetoelastic resonance sensors: A critical review," *Sensors,* vol. 2, no. 7, pp. 294-313, 2002.
[102] C. A. Grimes, P. G. Stoyanov, D. Kouzoudis, and K. G. Ong, "Remote query pressure measurement using magnetoelastic sensors," *Review of Scientific Instruments,* vol. 70, no. 12, pp. 4711-4714, 1999, doi: 10.1063/1.1150135.
[103] D. Kusumoto, L. P. Shen, N. Naruse, E. Mohri, and T. Uchiyama, "Detection of finger-tip blood vessel pulsation using CoSiB thin amorphous wire CMOS-IC SI sensor," *IEEE Transactions on Magnetics,* vol. 35, no. 5, pp. 4115-4117, 1999, doi: 10.1109/20.800773.

[104] K. Mohri, T. Uchiyama, L. Shen, C. Cai, Y. Honkura, and H. Aoyama, "Amorphous wire and CMOS IC based sensitive micro-magnetic sensors utilizing magneto-impedance (MI) and stress-impedance (SI) effects and applications," in *MHS2001. Proceedings of 2001 International Symposium on Micromechatronics and Human Science (Cat. No. 01TH8583)*: IEEE, pp. 25-34, 2001.

[105] H. O. Michaud, J. Teixidor, and S. P. Lacour, "Soft flexion sensors integrating strechable metal conductors on a silicone substrate for smart glove applications," in *2015 28th IEEE International Conference on Micro Electro Mechanical Systems (MEMS)*: IEEE, pp. 760-763, 2015.

[106] H. O. Michaud, L. Dejace, S. De Mulatier, and S. P. Lacour, "Design and functional evaluation of an epidermal strain sensing system for hand tracking," in *2016 IEEE/RSJ International Conference on Intelligent Robots and Systems (IROS)*: IEEE, pp. 3186-3191, 2016.

[107] H. O. Michaud, J. Teixidor, and S. P. Lacour, "Soft metal constructs for large strain sensor membrane," *Smart Materials and Structures,* vol. 24, no. 3, pp. 035020, 2015.

[108] N. Lu, C. Lu, S. Yang, and J. Rogers, "Highly sensitive skin-mountable strain gauges based entirely on elastomers," *Advanced Functional Materials,* vol. 22, no. 19, pp. 4044-4050, 2012.

[109] J.H. Kong, N.S. Jang, S.H. Kim, and J.M. Kim, "Simple and rapid micropatterning of conductive carbon composites and its application to elastic strain sensors," *Carbon,* vol. 77, pp. 199-207, 2014.

[110] T. Yamada,Y. Hayamizu,Y. Yamamoto,Y. Yomogida, A. Izadi-Najafabadi, D. N. Futaba and K. Hata, "A stretchable carbon nanotube strain sensor for human-motion detection," *Nature Nanotechnology,* vol. 6, no. 5, pp. 296, 2011.

[111] Y. Yang, Y. Luo , A. Guo , L. Yan , Y. Wu, K. Jiang, Q. Li, Sh. Fan and J. Wang, "Flexible and transparent strain sensors based on super-aligned carbon nanotube films," *Nanoscale,* vol. 9, no. 20, pp. 6716-6723, 2017.

[112] S. G. Yoon, H.J. Koo, and S. T. Chang, "Highly stretchable and transparent microfluidic strain sensors for monitoring human body motions," *ACS Applied Materials & Interfaces,* vol. 7, no. 49, pp. 27562-27570, 2015.

[113] X. Li, P. Sun, L. Fan, M. Zhu, K. Wang, M. Zhong, J. Wei, D. Wu, Y. Cheng and H. Zhu , "Multifunctional graphene woven fabrics," *Scientific Reports,* vol. 2, pp. 395, 2012.

[114] J. Li, S. Zhao, X. Zeng, W. Huang, Zh. Gong, G. Zhang, R. Sun and Ch. Wong, "Highly stretchable and sensitive strain sensor based on facilely prepared three-dimensional graphene foam composite," *ACS Applied Materials & Interfaces,* vol. 8, no. 29, pp. 18954-18961, 2016.

[115] Ch. Yan, J. Wang, W. Kang, M. Cui, X. Wang, C.Y. Foo, K. J. Chee and P. S. Lee, "Highly stretchable piezoresistive graphene–nanocellulose nanopaper for strain sensors," *Advanced Materials,* vol. 26, no. 13, pp. 2022-2027, 2014.

[116] S. Chen, Y. Wei, X. Yuan, Y. Lin, and L. Liu, "A highly stretchable strain sensor based on a graphene/silver nanoparticle synergic conductive network and a sandwich structure," *Journal of Materials Chemistry C,* vol. 4, no. 19, pp. 4304-4311, 2016.

[117] A. C. Yuen, A. A. Bakir, N. N. Z. M. Rajdi, C. L. Lam, S. M. Saleh, and D. H. Wicaksono, "Proprioceptive sensing system for therapy assessment using cotton fabric-based biomedical microelectromechanical system," *IEEE Sensors Journal,* vol. 14, no. 8, pp. 2872-2880, 2014.

[118] J. B. Chossat, Y. Tao, V. Duchaine, and Y. L. Park, "Wearable soft artificial skin for hand motion detection with embedded microfluidic strain sensing,"

in *2015 IEEE international conference on robotics and automation (ICRA)*: IEEE, pp. 2568-2573, 2015.
[119] F. L. Hammond, Y. Mengüç, and R. J. Wood, "Toward a modular soft sensor-embedded glove for human hand motion and tactile pressure measurement," in *2014 IEEE/RSJ International Conference on Intelligent Robots and Systems*: IEEE, pp. 4000-4007, 2014.
[120] A. V. Alaferdov, R. Savu, T. A. Rackauskas, M. A. Canesqui, D. S. Lara, G. O. Setti, E. Joanni, G. M. Trindade, U. B. Lima, A. S. Souza and S. A. Moshkalev "A wearable, highly stable, strain and bending sensor based on high aspect ratio graphite nanobelts," *Nanotechnology,* vol. 27, no. 37, pp. 375501, 2016.
[121] A. Tognetti, R. Bartalesi, F. Lorussi, and D. De Rossi, "Body segment position reconstruction and posture classification by smart textiles," *Transactions of the Institute of Measurement and Control,* vol. 29, no. 3-4, pp. 215-253, 2007.
[122] J. C. Y. Wang, Y. Xing, M. Shahid, H. Nishijima, and W. Pan, "Stretchable platinum network-based transparent electrodes for highly sensitive wearable electronics," vol. 13, no. 27, pp.1604291, 2017.
[123] C. T. Huang, C. L. Shen, C. F. Tang, and S. H. Chang, "A wearable yarn-based piezo-resistive sensor," *Sensors and Actuators A: Physical,* vol. 141, no. 2, pp. 396-403, 2008.
[124] R. Wijesiriwardana, T. Dias, and S. Mukhopadhyay, "Resistive fibre-meshed transducers," in *Seventh IEEE International Symposium on Wearable Computers, 2003. Proceedings.*: IEEE, pp. 200-209, 2003.
[125] M. Amjadi, A. Pichitpajongkit, S. Lee, S. Ryu, and I. Park, "Highly stretchable and sensitive strain sensor based on silver nanowire–elastomer nanocomposite," *ACS Nano,* vol. 8, no. 5, pp. 5154-5163, 2014.
[126] M. Amjadi, K. U. Kyung, I. Park, and M. Sitti, "Stretchable, skin-mountable, and wearable strain sensors and their potential applications: a review," *Advanced Functional Materials,* vol. 26, no. 11, pp. 1678-1698, 2016.
[127] A. Tognetti, F. Lorussi, G. D. Mura, N. Carbonaro, M. Pacelli, R. Paradiso, D. D. Rosii, "New generation of wearable goniometers for motion capture systems," *Journal of NeuroEngineering and Rehabilitation,* vol. 11, no. 1, pp. 56, 2014 , doi: 10.1186/1743-0003-11-56.
[128] Y. H. Takeo Yamada, Yuki Yamamoto, Yoshiki Yomogida, Ali Izadi-Najafabadi, Don N. Futaba & Kenji Hata, "A stretchable carbon nanotube strain sensor for human-motion detection," *Nature Nanotechnology,* vol. 6, pp. 296-301, 2011.
[129] a. Yang Yu, c Yufeng Luo,a,c Alexander Guo,a Lingjia Yan,a Yang Wu,a Kaili Jiang,a,b and a. Qunqing Li, b Shoushan Fana,c and Jiaping Wang, "Flexible and transparent strain sensors based on super-aligned carbon nanotube films†," *Nanoscale,* vol. 9, no. 20, pp. 6716-6723, 2017.
[130] S. J. Park, J. Kim, M. Chu, and M. Khine, "Highly Flexible Wrinkled Carbon Nanotube Thin Film Strain Sensor to Monitor Human Movement," *Advanced Materials Technologies,* vol. 1, no. 5, pp. 1600053, 2016, doi: 10.1002/admt.201600053.
[131] Y. Cheng, R. Wang, J. Sun, and L. Gao, "A Stretchable and Highly Sensitive Graphene-Based Fiber for Sensing Tensile Strain, Bending, and Torsion," *Advanced Materials,* vol. 27, no. 45, pp. 7365-7371, 2015, doi: 10.1002/adma.201503558.
[132] G. Saggio, F. Riillo, L. Sbernini, and L. R. Quitadamo, "Resistive flex sensors: a survey," *Smart Materials and Structures,* vol. 25, no. 1, pp. 013001, 2015.

[133] Blommberg. “Company overview of abrams gentile entertainment, inc.” [Online]. Available:https://www.bloomberg.com/research/stocks/private/snapshot.asp?privcapId=995949

[134] A. News. “Backwards compatible - the Power Glove.”[Online]. Available: http://www.abc.net.au/tv/goodgame/stories/s2248843.htm

[135] Images Scientific Instruments. Inc., Staten Island, NY, USA. [Online]. Available: http://www.imagesco.com/

[136] S. S. Corp., Salt Lake City, UT, USA. [Online]. Available: http://www.spectrasymbol.com/

[137] I. Flexpoint Sensor Systems. Draper, UT, USA. [Online]. Available: http://www.flexpoint.com/

[138] I. Images Scientific Instruments. Two-Directional Bi-Flex Sensors, Staten Island, NY, USA. [Online]. Available: http://www.imagesco.com/sensors/flex-sensor.html

[139] G. Orengo, G. Saggio, S. Bocchetti, and F. Giannini, "Evaluating Strain Sensor Performance for Motion Analysis," in *BIODEVICES*, 2011, pp. 244-249.

[140] N. Williams, J. Penrose, C. Caddy, E. Barnes, D. Hose, and P. Harley, "A goniometric glove for clinical hand assessment: construction, calibration and validation," *The Journal of Hand Surgery: British & European Volume,* vol. 25, no. 2, pp. 200-207, 2000.

[141] G. Costantini, M. Todisco, and G. Saggio, "A wireless glove to perform music in real time," in *8th WSEAS International Conference on APPLIED ELECTROMAGNETICS, WIRELESS and OPTICAL COMMUNICATIONS, Penang, Malaysia*, 2010.

[142] G. Saggio, M. De Sanctis, E. Cianca, G. Latessa, F. De Santis, and F. Giannini, "Long term measurement of human joint movements for health care and rehabilitation purposes," in *2009 1st International Conference on Wireless Communication, Vehicular Technology, Information Theory and Aerospace & Electronic Systems Technology*: IEEE, pp. 674-678, 2009.

[143] "SparkFun Electronics, Flex/Force Sensor, Niwot, CO, USA. [Online]. Available: https://www.sparkfun.com/categories/143 ".

[144] M. Borghetti, E. Sardini, and M. Serpelloni, "Evaluation of bend sensors for limb motion monitoring," in *2014 IEEE International Symposium on Medical Measurements and Applications (MeMeA)*: IEEE, pp. 1-5, 2014.

[145] L. K. Simone and D. G. Kamper, "Design considerations for a wearable monitor to measure finger posture," *Journal of NeuroEngineering and Rehabilitation,* vol. 2, no. 1, pp. 5, 2005.

[146] G. Saggio, "Bend sensor arrays for hand movement tracking in biomedical systems," in *2011 4th IEEE International Workshop on Advances in Sensors and Interfaces (IWASI)*: IEEE, pp. 51-54, 2011.

[147] B. Flynn, J. Sanchez, P. Angove, J. Connolly, J. Condell, and K. Curran, "Novel Smart Sensor Glove for Arthritis Rehabilitation," in *EPoSS 2013-EPoSS General Assembly & Annual Forum*, 2014.

[148] R. Gentner and J. Classen, "Development and evaluation of a low-cost sensor glove for assessment of human finger movements in neurophysiological settings," *Journal of Neuroscience Methods,* vol. 178, no. 1, pp. 138-147, 2009.

[149] G. Saggio, "A novel array of flex sensors for a goniometric glove," *Sensors and Actuators A: Physical,* vol. 205, pp. 119-125, 2014.
[150] J. Jurgens and P. Patterson, "Development and evaluation of an inexpensive sensor system for use in measuring relative finger positions," *Medical Engineering & Physics,* vol. 19, no. 1, pp. 1-6, 1997.
[151] M. Melzer, J. I. Monch, D. Makarov, Y. Zabila ,G. S. Bermúdez, D.Karnaushenko, S. Baunack , F. Bahr, Ch. Yan. M. Kaltenbrunner, O. G. Schmidt, "Wearable Magnetic Field Sensors for Flexible Electronics," *Advanced Materials,* vol. 27, no. 7, pp. 1274-1280, 2015, doi: 10.1002/adma.201405027.
[152] S. Bell, "A beginner's guide to uncertainty of measurement," *Measurement Good Practice Guide,* vol. 11, pp. 1, 1999.
[153] A. Podut, *Strength of Materials Supplement for Power Engineering*. British Columbia Institute of Technology, June 23, 2018.
[154] S. Atalay and P. T. Squire, "Comparative measurements of the field dependence of Young's modulus and shear modulus in Fe-based amorphous wire," *Journal of Applied Physics,* vol. 70, no. 10, pp. 6516-6518, 1991, doi: 10.1063/1.349892.
[155] A. Inoue, H. Chen, J. Krause, T. Masumoto, and M. Hagiwara, "Young's modulus of Fe-, Co-, Pd-and Pt-based amorphous wires produced by the in-rotating-water spinning method," *Journal of Materials Science,* vol. 18, no. 9, pp. 2743-2751, 1983.
[156] A. Guinier, *X-ray Diffraction in Crystals, Imperfect Crystals, and Amorphous Bodies*. Dover Publications, 1994.
[157] R. dos Santos, M. Patel, J. Cuadros, and Z. Martins, "Influence of mineralogy on the preservation of amino acids under simulated Mars conditions," *Icarus,* vol. 277, pp. 342-353, 2016.
[158] K. Mohri, F. Humphrey, K. Kawashima, K. Kimura, and M. Mizutani, "Large Barkhausen and Matteucci effects in FeCoSiB, FeCrSiB, and FeNiSiB amorphous wires," *IEEE Transactions on Magnetics,* vol. 26, no. 5, pp. 1789-1791, 1990.
[159] S. Kane, M. Vazquez, A. Hernando, and A. Gupta, "Influence of current annealing, stress, torsion and dc magnetic field on Matteucci effect in amorphous wires," *Materials Science and Engineering: A,* vol. 304, pp. 1055-1057, 2001.
[160] J. Gonzalez, J.M. Blanco, J.M. Barandiaran, M. Vazquez, A. Hernando, G. Rivero and D. Niarchos, "Helical magnetic anisotropy induced by current annealing under torsion in amorphous wires," *IEEE Transactions on Magnetics,* vol. 26, no. 5, pp. 1798-1800, 1990.
[161] J. T. Muth, D. M. Vogt , R. L. Truby , Y. Mengüç , D. B. Kolesky ,R. J. Wood and J. A. Lewis, "Embedded 3D printing of strain sensors within highly stretchable elastomers," *Advanced Materials,* vol. 26, no. 36, pp. 6307-6312, 2014.
[162] J. Lee, S. Kim, J. Lee, D. Yang, B. Ch. Park, S. Ryu and I. Park, "A stretchable strain sensor based on a metal nanoparticle thin film for human motion detection," *Nanoscale,* vol. 6, no. 20, pp. 11932-11939, 2014.
[163] G. Dhatt, E. Lefrançois, and G. Touzot, *Finite element method*. John Wiley & Sons, 2012.
[164] U. K. A. Service, *The expression of uncertainty and confidence in measurement*. United Kingdom Accreditation Service, 2012.
[165] Commercial bends sensor from Bebop available at: https://bebopsensors.com/

[166] L. Wang, T. Meydan, P. Williams, and T. Kutrowski, "A proposed optical-based sensor for assessment of hand movement," in *2015 IEEE SENSORS*: IEEE, pp. 1-4, 2015.
[167] M. Donno, E. Palange, F. Di Nicola, G. Bucci, and F. Ciancetta, "A new flexible optical fiber goniometer for dynamic angular measurements: Application to human joint movement monitoring," *IEEE Transactions on Instrumentation and Measurement,* vol. 57, no. 8, pp. 1614-1620, 2008.
[168] M. Nishiyama and K. Watanabe, "Wearable sensing glove with embedded hetero-core fiber-optic nerves for unconstrained hand motion capture," *IEEE Transactions on Instrumentation and Measurement,* vol. 58, no. 12, pp. 3995-4000, 2009.
[169] Y. Park, J. Lee, and J. Bae, "Development of a wearable sensing glove for measuring the motion of fingers using linear potentiometers and flexible wires," *IEEE Transactions on Industrial Informatics,* vol. 11, no. 1, pp. 198-206, 2014.
[170] L. K. Simone, N. Sundarrajan, X. Luo, Y. Jia, and D. G. Kamper, "A low cost instrumented glove for extended monitoring and functional hand assessment," *Journal of Neuroscience Methods,* vol. 160, no. 2, pp. 335-348, 2007.